Coupling single electron spins to external degrees of freedom

Von der Fakultät 8 Mathematik und Physik der Universität Stuttgart zur Erlangung der Würde eines Doktors der Naturwissenschaften (Dr. rer. nat.) genehmigte Abhandlung

Vorgelegt von

Thomas Oeckinghaus

aus Waiblingen

Hauptberichter: Prof. Dr. Jörg Wrachtrup

Mitberichter: Prof. Dr. Sebastian Loth

Tag der mündlichen Prüfung: 29.04.2020

3. Physikalisches Institut der Universität Stuttgart

2020

Contents

Summary

At the turn of the last century, the theory of quantum mechanics arose from explanations of experimental observations on blackbody radiation and the photoelectric effect by Max Planck [1] and Albert Einstein [2]. In the following decades, the theory evolved to contain fundamental ideas like the wave-particle duality and the uncertainty principle and became the most successful theory of modern physics. Over time, quantum mechanics grew from a conceptual framework, used to grasp the unintuitive behavior of microscopic systems, to the basis of key technologies, like e.g. photo-voltaic, medical imaging and semiconductor technology. Over the last decades, rapid advances in the capability of controlling individual quantum systems paved the way to new quantum technologies [3], like quantum computing [4, 5, 6], quantum enhanced sensing [7, 8] and secure quantum communication [9]. Examples of prominent systems utilized for such applications are superconducting qubits, quantum dots, photons, trapped ions, solid state spins and nanomechanical resonators. These systems exhibit different properties, resulting in specific advantages and disadvantages. For example, single electron spins are prime candidates for nanoscale quantum sensors due to their strong coupling to the environment. At the same time, this coupling inherently reduces their spin lifetime, making them less suitable for storing quantum states. By coupling different types of quantum systems, their advantages can be combined to form a new and more powerful generation of quantum devices.

The nitrogen-vacancy (NV) center in diamond is at the center of this thesis. This color center, consisting of a substitutional nitrogen atom and an adjacent vacancy in the carbon lattice, is one of the most promising solid state spin systems for various quantum applications. The electron spin associated with the negatively charged NV center exhibits long coherence times even at ambient conditions and can be optically polarized and read out. Its high sensitivity to

its environment make it a potent sensor for magnetic, electric and strain fields. Using techniques developed in nuclear magnetic resonance (MNR) and electron spin resonance (ESR) experiments, a high bandwidth from DC to several GHz can be achieved. A key feature is its small size, which enables nanoscale imaging via scanning probe microscopy (SPM).

This thesis is focused on coupling the electron spin of single NV centers to additional quantum systems. It is demonstrated that the observed interactions between the systems can not only be used to improve the performance of NV centers in quantum sensing experiments, but also widen the spectrum of possible applications. Over the course of this work, NV centers were coupled to three different types of systems - electron spins located in external spin labels, nuclear spins embedded in the diamond lattice and diamond nanomechanical resonators.

Nanoscale ESR of spin-labeled biomolecules is demonstrated in Chapter 3. Electron spin labels (SL) are an important tool commonly used for structural analysis of biomolecules via electron spin resonance (ESR) [10, 11]. SLs are designed to bind to specific chemical sites of target molecules. This process is known as site-directed spin labeling (SDSL). Using double electron-electron resonance (DEER) spectroscopy, the distances between SLs can be measured with high precision. This way, SLs can be used as nanoscale rulers to map out the structure of the spin-labeled molecule. Such conventional ESR measurements require averaging over a high number of electron spins inside a macroscopic sample volume (~μm^3). As a result, it is difficult to gain information about different structural configurations in inhomogeneous samples. In contrast, the NV-based nanoscale ESR demonstrated in this thesis allows to detect SLs in a sample volume of few ~nm^3, potentially providing structural information of single molecules.

The model system studied in this work consists of the amino acid polymer poly-L-lysine (PLL) labeled with nitroxide spin labels (NSL). The diamond surface was coated with a 5 nm layer of spin labeled PLL. The recipe of the spin labeling process was adjusted to attach NSLs to ~60% of the lysines, which corresponds to a spin density of ~1 spin/nm^3 in final PLL layer. DEER spectroscopy was performed with ten individual NV centers. In the presence of the

spin labeled PLL layer, a strong DEER signal was observed on all NV centers. 80% of the recorded spectra showed three peaks, matching the characteristic hyperfine structure of the NSLs. An average spin contrast of $\bar{S}$ = 15.9% was observed. As a reference, the experiment was repeated with a cleaned diamond surface and a layer of unlabeled PLL. Here, a signal in the DEER spectra was only detected on 5% of NV centers. The few observed signals did not exhibit side peaks and are attributed to dangling bonds on the diamond surface created during the surface preparation. The average signal strength was observed to be $\bar{S}$ = 1.3% and thus, significantly weaker than in the presence of NSLs. Due to the significant difference between the measurement results with and without NSLs and the observation of side-peaks, the observed signals can be attributed to the coupling to NSLs.

Under ambient conditions, decay of the NSLs during the experiments was observed. This is attributed to photochemical modification of the NSLs induced by the laser light used for the initialization and readout of the NV center. The instability of the NSLs prevented detection of single electron spins at lower spin concentrations. However, follow-up experiments performed by Schlipf et al. demonstrate that the NSLs become stable for several weeks at low temperature and ultra-high vacuum [12]. This allowed the detection of small numbers of spin labels (<6) and measurement of their inter-spin distances, paving the way towards new potential applications.

Scanning probe microscopy (SPM) techniques can be used to perform NV-based ESR imaging. By bringing small magnetic AFM tips close to the spin labels, strong magnetic field gradients in the sample volume can be created. By monitoring the ESR signal during scanning of the tip, imaging of the electron spin with subnanometer resolution is possible[13]. Furthermore, diamond AFM tips containing single NV centers could be used to perform ESR imaging of spin labels over wider sample areas [14, 15, 16, 17, 18, 19].

Another possible application is the use of spin labeled molecules as quantum spin networks, as proposed by Schlipf et al.. Here, the precise positioning, offered by SDSL, is used to fabricate arrays of closely spaced electron spins. The exact positions and spin-spin distances are controlled by the chemical structure of the host molecule. At distances of few nanometers, the spin labels are coupled via their dipolar magnetic interaction. In this scenario, the NV center acts

as an access point to the multi-spin network composed of the spin labels.

Nuclear quantum-assisted sensing is presented in Chapter 4. This technique is used to improve the signal-to-noise ratio of NV center based sensing experiment. Typically, the state of the electron spin is read out optically by its fluorescence response to a laser pulse after each repetition of the sensing sequence. Due to optical repolarization of the spin state during the laser pulse, the readout is limited to short laser pulses of ~300 ns. With typical photon count rates, this gives ~0.1 photon per readout. For short sensing sequences, the low number of detected photons per readout is not crucial, as the complete experiment sequence can be repeated in fast succession. With increasing duration of the sensing sequence, the direct optical readout of the electron spin becomes inefficient. In this case, a longer readout yielding a higher number of photons is preferable. Such a readout can be achieved using a technique first demonstrated by Neumann et al. [20]. Here, the nuclear spin is used as a long living memory to readout the electron spin state with high fidelity in a single shot. For this purpose, the electron spin state is first mapped onto the nuclear spin. Subsequently, the nuclear spin is repetitively read out via the electron spin using a quantum non-demolition measurement. To achieve a high readout fidelity, a strong bias magnetic field aligned to the NV axis is required to increase the nuclear spin lifetime. In this thesis, an implementation of this technique is demonstrated which still allows mechanical access to the diamond sample via an atomic force microscope (AFM). This required a custom redesign of the AFM tip holder, as well as a careful design of the magnet geometry used to generate a sufficient bias magnetic field under the present spatial restrictions. A fidelity of 85% at a magnetic field of 0.28 T was achieved. To benchmark the SNR gain introduced by the SSR method, the spin lifetime of the NV centers electron was measured with and without the technique. A SNR gain of 14% was observed using the quantum nuclear-assisted sensing technique. This value fits well to the theoretical prediction of 22% obtained from expression for the SNRs derived in this work. The SNR improvement depends strongly on the experimental conditions. In follow-up experiments, performed by Häberle et al., an improvement of the SNR by a factor of 8.6 was observed due to a higher bias magnetic field [21].

NV-mechanical hybrid systems composed of single NV centers coupled to mechanical resonators are presented in Chapter 5. In the last decade, technical advances allowed to bring mechanical resonators into the quantum regime [22, 23, 24, 25]. Such resonators are promising candidates for versatile nanoscale sensors and transducers in quantum networks. This prospect stems from their sensitivity to a variety of different forces, like e.g. radiation pressure, magnetic forces and electric forces. Consequently, mechanical resonators can couple to various quantum systems with prominent examples being superconducting qubits [26, 23, 27, 28], photons [29] and solid-state spins [30, 31, 32, 33, 34]. NV centers have successfully been coupled to mechanical resonators in the form of cantilevers [33, 35, 36, 37, 38], bulk resonators [39, 40], membranes [34] and surface acoustic waves [41]. However, the experimental efforts so far were limited to single mechanical resonators. In this work, the established methods of NV-mechanical coupling are extended to a system of two coupled mechanical resonators. Two possible applications of this system were studied. First, the system is a potential architecture for multi-qubit networks, where spin-spin interactions are mediated by phonons. Similar hybrid systems were already theoretically studied [42] but not realized experimentally. The second application is high sensitivity mass sensing, where a partial localization of the common modes can be used as a measure for mass imbalances between the cantilever. Under the right experimental conditions, this results in a higher sensitivity compared to single cantilever systems where the mass is measured by observation of frequency shifts. The investigated system consists of two coupled diamond cantilevers hosting a random distribution of shallow NV centers created via ion-implantation. The cantilevers are elastically coupled via a thin shared baseplate holding both of them.

In a first step, a thorough characterization of the mechanical subsystem is performed. For this purpose, mechanical oscillations are excited by a piezoelectric actuator mounted on the sample holder. The cantilever motion is tracked using a purely optical readout scheme, based on time-resolved and phase-locked detection of laser light reflected from the sample surface. This allows to simultaneously determine the frequency, phase and amplitude of the cantilever oscillations. Scanning of the probe laser also enables imaging of the respective mode shape. This is crucial to unambiguously identify the symmetric and anti-

symmetric common modes of the cantilever pair. The analyzed cantilevers are ~100x5x2.5 µm in size, possess resonance frequencies of ~1 MHz and quality factors of $Q \approx 10^3$ under ambient conditions. At low temperature and ultra-high vacuum quality factors of up to $Q_{\mathrm{LT,UHV}} \approx 10^6$ are observed.

Two different techniques are used to establish a spin-phonon coupling. The coupling is either mediated by the intrinsic strain generated by a deflection of the cantilever or a high magnetic field gradient which translates positional changes of the NV center into an effective magnetic field. The highest strain in a bent cantilever occurs at the clamping point and close to the diamond surface. For a shallow NV center positioned at the clamping point, a strain-mediated spin-phonon coupling of $g_{\mathrm{str}} = 2\pi\times(2.14\pm0.08)$ mHz was determined. A ~1000-fold higher spin-phonon coupling of $g_{\mathrm{mag}} = 2\pi \times (0.87 \pm 0.03)$ Hz was achieved using a high magnetic field gradient. The magnetic field gradient was generated by a home-fabricated magnetized tip positioned ~50 nm above a NV center located close to the open end of the cantilever via an atomic force microscope. The magnetic field gradient translates deflections of the cantilever into an effective magnetic field at the NV centers position. Using this technique, a magnetic field gradient of $\delta B_z = (1.8 \pm 0.1) \times 10^5$ T/m was achieved. In contrast to strain-mediated coupling, this method suffers from drifts of the magnetized tip as well as deterioration of the NV centers coherence time due to magnetic noise emanating from the magnetized tip.

An important figure of merit of hybrid systems is the cooperativity C, which is the ratio of the inter-system coupling and the dissipation of the system. In case of a spin-mechanical hybrid system, the cooperativity is defined as $C = g^2/\Gamma_s\Gamma_m$, where Γ_s is the decoherence of the spin and Γ_m is the phonon decay rate. An important regime is $C > 1$, where the spin-phonon interaction becomes coherent and entanglement between spins and phonons is feasible. Under ambient conditions the cooperativity of the investigated system is below $C < 10^{-6}$. However, it is shown that with improvements of the experimental conditions a cooperativity above one can be achieved. Here, the main challenge to decrease the size of the mechanical structure while also improving the spin properties of the embedded NV center.

A coupled cantilever pair can only be used as a quantum bus if the spins in both cantilevers are coupled to the same mechanical mode. To experimen-

tally demonstrate that this requirement is met in the studied system, the characteristic cantilever motion associated with the symmetric and antisymmetric common mode was successfully imprinted into the electron spin state of NV centers in both cantilevers. This was achieved by using a dynamical decoupling sequence (XY8) phase-locked to the mechanical excitation signal.

In a further step, the piezo-actuator-based excitation of the whole sample was replaced by photo-thermal excitation of a single cantilever. For this purpose, the cantilever is illuminated by a pulsed infrared laser which periodically heats the cantilever at its resonance frequency. The resulting oscillation can be observed by NV centers in both cantilevers. This demonstrates phonon-mediated transduction of a local force to a distant spin located in a different mechanical resonator. Using the susceptibility of the distant spin to the photo-thermally induced force allows to calculate a classical upper bound for the effective spin-spin coupling between spins in separate cantilevers. Under ambient conditions, a maximum coupling of $g_{\text{s-s}} = 60.1$ mHz is expected. This coupling is too weak to be observed experimentally under the prevalent experimental conditions. Nevertheless, the conducted experiments show that arrays of elastically coupled cantilevers can be used as a quantum bus in multi-spin networks.

An important criteria of quantum networks is their scalability. The maximum number of cantilevers N_{max} in the studied system is limited by two effects. First, the total mass of the system increases with the number of cantilevers. Finite-element method (FEM) simulations show that the effective mass of the cantilever array increases approximately linearly with the number of cantilevers. This results in a decrease of the spin-phonon couplings with a scaling of $g \propto \frac{1}{\sqrt{N}}$. Second, an increasing number of cantilever leads to an according increase of mechanical modes, and thereby the mode density. At a too high mode density, single mechanical modes can not be addressed individually anymore. Using FEM simulations it was shown that $N_{\text{max}} > 100$ assuming a quality factor of $Q = 10^6$. These limitation can be circumvented by encapsulating a large cantilever array into smaller subregister. By coupling the subregister via a switchable capacitive interaction, the individual register can be isolated when needed, while still being able to transfer information on demand. This approach is discussed in more detail in a work of Rabl et al. [42].

Zusammenfassung

Zu Beginn des letzten Jahrhunderts entstand die Theorie der Quantenmechanik aus Erklärungen experimenteller Beobachtungen von Schwarzkörper-Strahlung und des photoelektrischen Effekts durch Max Planck [1] und Albert Einstein [2]. In den darauffolgenden Jahrzehnten wurde die Theorie weiterentwickelt um fundamentale Ideen wie die Welle-Teilchen-Dualität und das Prinzip der Unschärferelation mit einzuschließen und wurde so zur erfolgreichsten Theorie der modernen Physik. Mit der Zeit wuchs die Quantenmechanik von einem konzeptionellen Gerüst, verwendet um das unintuitive Verhalten von mikroskopischen Systems zu verstehen, zur Grundlage von Schlüsseltechnologien wie z.B. Photovoltaik, bildgebenden medizinischen Verfahren und der Halbleitertechnologie. In den letzten Jahrzehnten ebneten rasante Fortschritte in der Kontrolle von einzelnen Quantensystemen den Weg zu neuen Quantentechnologien [3] wie Quantencomputation [4, 5, 6], Quantensensorik [7, 8] und sicherer Quantenkommunikation [9]. Beispiele prominenter Systeme, die für diese Anwendungen verwendet werden, sind supraleitende Quantenbits, Quantenpunkte, Photonen, gefangene Ionen, Festkörperspins und nanomechanische Resonatoren. Diese System haben unterschiedliche Eigenschaften, welche zu spezifischen Vor- und Nachteilen führen. Zum Beispiel sind einzelne Elektronenspins geeignete Kandidaten für die Verwendung als Quantensensor aufgrund der starken Kopplung zu ihrer Umgebung. Andererseits führt diese Kopplung zur Verringerung der Spinlebenszeit und macht sie dadurch ungeeignet für das Speichern von Quantenzuständen. Durch das Koppeln verschiedener Quantensysteme können ihre individuellen Vorteile kombiniert werden, um eine neue und leistungsfähige Generation von Quantengeräten zu formen.

Das Stickstoff-Fehlstellen Zentrum in Diamant (im Folgenden als NV Zentrum bezeichnet) steht im Zentrum dieser Arbeit. Dieses Farbzentrum, bestehend aus einem Stickstoffatom und einer benachbarten Fehlstelle im Kohlen-

stoffgitter, ist einer der prominentesten Festkörpersysteme für eine Vielzahl an Quantenanwendungen. Der Elektronenspin des negativ geladenen NV Zentrums zeigt sogar unter Normalbedingungen lange Kohärenzzeiten und kann optisch polarisiert und aufgelesen werden. Seine hohe Sensitivität gegenüber seiner Umgebung machen es zu einem leistungsfähigen Sensor für Magnetfelder, elektrische Felder und mechanischer Verspannungen. Durch die Verwendungen von Techniken, welche ursprünglich für Kernspinresonanz und Elektronenspinresonanz (ESR) entwickelt wurden, kann eine hohe Bandbreite von Gleichstrom zu Frequenzen von mehreren GHz erreicht werden. Eine Schlüsseleigenschaft des NV Zentrums ist seine kleine Größe, welche bildgebende Verfahren durch die Verwendung von Rasterprobenmikroskopie erlaubt.

Diese Arbeit ist auf das Koppeln von einzelnen NV Zentren an zusätzliche Quantensysteme fokussiert. Es wird gezeigt, dass die beobachteten Interaktionen zwischen den Systemen nicht nur die Leistungsfähigkeit von NV Zentren im Bereich der Quantensensorik verbessern, sondern auch das Spektrum an möglichen Anwendungen erweitern. Im Laufe der Arbeit wurden NV Zentren an drei verschiedene Arten von Systemen gekoppelt - Elektronenspins in externen Spinmarkern, Kernspins im Diamantgitter und nanomechanische Resonatoren aus Diamant.

ESR von spinmarkierten Biomolekülen auf der Nanoskala wird in Kapitel 3 diskutiert. Elektronenspinmarker sind wichtige Werkzeuge für die Strukturanalyse von Biomolekülen mittels ESR [10, 11]. Spinmarker sind designt, um an spezifische chemische Gruppen von Zielmolekülen zu binden. Dieser Prozess ist als ortsspezifische Spinmarkierung bekannt. Durch die Verwendung von Doppel-Elektron-Elektron-Resonanz (DEER) Spektroskopie können die Abstände zwischen Spinmarkern mit hoher Präzision bestimmt werden. Auf diese Weise können die Spinmarker als Lineale auf der Nanoskala verwendet werden um die Struktur des spinmarkierten Moleküls auszumessen. Solche gewöhnlichen ESR Messungen müssen über eine hohe Zahl an Elektronenspin in einem makroskopischen Sensorbereich mitteln. Das führt dazu, dass Informationen über verschiedene strukturelle Konfigurationen in inhomogenen Proben nur schwer zu erhalten sind. Im Gegensatz dazu, ermöglicht die NV-basierte ESR Spektroskopie auf der Nanoskala die Detektion von Spinmarkern

in einem Volumen von wenigen Nanoqubikmetern. Dies kann verwendet werden, um Strukturanalyse an einzelnen Molekülen durchzuführen.

Das Modellsystem, welches in dieser Arbeit verwendet wurde besteht aus dem Aminosäurenoolymer Poly-L-lysine (PLL) an welchen Nitroxid-Spinmarker gebunden sind. Eine 5 nm dicke Schicht von spinmarkierten PLL wurde auf die Diamantoberfläche aufgebracht. Das Rezept für das Anbinden der Nitroxid-Spinmarker wurde angepasst, um ca. 60% der Lysine Spinmarker zu binden. Dies entspricht einer ungefähren Spindichte von 1 Spin/nm^3 in der aufgebrachten PLL Schicht. DEER Spektroskopie wurde mit zehn individuellen NV Zentren durchgeführt. In der Gegenwart der Schicht aus spinmarkierten PLL, wurde mit allen NV Zentren ein starkes DEER Signal beobachtet. Dabei zeigten 80% der aufgenommenen Spektren drei Peaks, welche zur charakteristischen Hyperfeinsturktur von Nitroxid-Spinmarkern passen. Es wurde ein durchschnittlicher Spinkontrast von $\hat{S}_{\max} = 15.9\%$ beobachtet. Als Referenz wurde das Experiment mit einer gereinigten Diamantoberfläche und einer Schicht aus nicht spinmarkiertem PLLs wiederholt. Dabei wurde nur bei 5% der NV Zentren ein DEER Signal detektiert. Die aufgetretenen Signale zeigten keine Seitenpeaks und werden nicht gesättigten Bindungen an der Diamantoberfläche, welche bei der Oberflächenbehandlung entstehen, zugeordnet. Die durchschnittliche Signalstärke lag bei nur $\hat{S}_{\max} = 1.3\%$ und ist damit signifikant schwächer als in der Anwesenheit von Nitroxid-Spinmarker. Aufgrund der deutlichen Unterschiede der Messergebnisse, mit und ohne Spinmarkern, können die beobachteten Signale der dipolaren Interaktion mit den Spinmarkern zugeschrieben werden.

Unter Normalbedingungen wurde ein Zerfall der Spinmarker im Laufe der Experimente festgestellt. Dies wird photochemischen Modifikationen der Nitroxid-Spinmarker, verursacht durch das Laserlicht, welches für die Initialisierung und das Auslesen der NV Zentren verwendet wird, zugeschrieben. Die Instabilität der Spinmarker verhinderte das Detektieren von einzelnen Elektronenspins bei geringeren Spindichten. Allerdings wurde in Folgeexperimenten, durchgeführt von Schlipf et al. gezeigt, dass die Nitroxid-Spinmarker bei tiefen Temperaturen und unter Ultrahochvakuum über mehrere Wochen stabil bleiben [12]. Dies ermöglichte die Detektion einer kleinen Anzahl an Spinmarkern (<6) und die Messung der Abstände zwischen den Spins. Dieses Experiment ebnet den Weg zu neuen potentiellen Anwendungen.

Techniken der Rastersondenmikroskopie können verwendet werden um NV-basierte bildgebende ESR durchzuführen. Indem man eine kleine magnetische Rasterkraftmikroskop-Spitze in die Nähe der Spinmarker bringt, können starke Magnetfeldgradienten im Probenvolumen erzeugt werden. Durch das Messen von ESR-Signalen während des Rasterns der Spitze, wir das Abbilden der Elektronenspins mit einer Auflösung im Subnanometer-Bereich möglich [13]. Außerdem können Rasterkraftmikroskop-Spitzen aus Diamant, welche einzelne NV Zentren enthalten, verwendet werden um ESR Abbildungen von größere Probenflächen zu erstellen [14, 15, 16, 17, 18, 19].

Eine weitere mögliche Anwendung ist das Verwenden von spinmarkierten Molekülen als Quantennetzwerke, wie es von Schlipf et al. vorgeschlagen wurde. Hierbei wird die präzise Positionierung, die durch ortspezifische Spinmarkierung ermöglicht wird, ausgenutzt, um Register aus eng beieinander liegenden Elektronenspins zu erzeugen. Die genauen Positionen und Abstände zwischen den Spins können dabei durch die chemische Struktur des spinmarkierten Moleküls bestimmt werden. Bei Abständen von wenigen Nanometern sind die Spinmarker über ihre magnetische Dipolwechselwirkung gekoppelt. In diesem Aufbau erfüllt das NV Zentrum die Rolle eines Zugangspunktes zum, aus den Spinmarkern bestehenden, Spinnetzwerk.

Kernspin-unterstütze Quantensensorik wird in Kapitel 4 vorgestellt. Diese Technik wird verwendet um das Signal-zu-Rausch-Verhältnis (SNR, aus dem Englischen: signal-to-noise ratio) von NV-basierten Messverfahren zu verbessern. Typischerweise wird der Elektronenspinzustand eines NV Zentrums über seine Fluoreszenzantwort auf einen Laserpuls nach jeder Wiederholung der Messsequenz ausgelesen. Durch die optische Repolarisation des Spinzustands während des Laserpulses, ist das Auslesen auf kurze Laserpulse mit einer Dauer von ca. 300 ns begrenzt. Mit typischen Photonendetektionsraten erhält man damit ca. 0.1 Photonen pro Ausleseprozess. Bei kurzen Messsequenzen ist die geringe Anzahl an Photon pro Auslese nicht entscheidend, da das komplette Experiment in schneller Aufeinanderfolge wiederholt werden kann. Mit steigender Dauer der Messsequenz wird das direkte optische Auslesen allerdings ineffizient. In diesem Fall sind längere Auslesemethoden, die eine höhere Anzahl an Photonen erzeugen, vorzuziehen. Eine solche Auslesemethode kann durch

eine Technik, die zuerst von Neumann et al. demonstriert wurde, erreicht werden [20]. Hierzu wird ein Kernspin als ein langlebiger Speicher verwendet, um den Elektronenspinzustand in einem einzelnen Ausleseprozess mit hoher Wahrscheinlichkeit zu bestimmen. Zu diesem Zweck wird zunächst der Elektronenspinzustand auf den Kernspin abgebildet. Anschließend wird der Kernspin wiederholt, über den Elektronenspin, mit einer Spinzustand-erhaltenden Messung ausgelesen. Um eine hohe Messgenauigkeit zu erreichen wird ein starkes Magnetfeld entlang der NV-Achse, welches die Kernspinlebensdauer erhöht, benötigt. In dieser Arbeit wird eine Umsetzung dieser Technik präsentiert, welche mechanischen Zugang zur Diamantprobe mit einem Rasterkraftmikroskop (RKM) erlaubt. Dies benötigte ein neues maßgeschneidertes Design des RKM-Spitzenhalters, sowie ein spezielles Design der magnetischen Geometrie, welche zur Generierung eines ausreichend starken Magnetfelds unter den vorhanden räumlichen Einschränkungen benötigt wird. Bei einem Magnetfeld von 0.28 T wurde eine Auslesewahrscheinlichkeit von 85% erreicht. Um die Steigerung des SNR durch die Kernspin-unterstütze Auslesemethode zu bestimmen, wurde die Spinlebensdauer des Elektronenspins eines NV Zentrums mit und ohne die Technik gemessen. Dabei wurde eine SNR Verbesserung von 14% beobachtet wenn die Kernspin-unterstützte Auslesemethode verwendet wurde. Dieser Wert passt gut zu der theoretischen Vorhersage von 22%, die aus Gleichungen für das SNR, welche in dieser Arbeit hergeleitet wurden, bestimmt wurde. Die Steigerung des SNR hängt stark von den experimentellen Bedingungen ab. In darauffolgenden Messungen, durchgeführt von Häberle et al., wurde eine Steigerung des SNR um einen Faktor von 8.6 [21] festgestellt. Dies wurde durch ein höheres äußeres Magnetfeld erreicht.

NV-mechanische Hybridsysteme die aus einzelnen NV Zentren, gekoppelt an mechanische Resonatoren, bestehen werden in Kapitel 5 präsentiert. Im letzten Jahrzehnt erlaubten technische Fortschritte es, mechanische Resonatoren in das Quantenregime zu bringen [22, 23, 24, 25]. Solche Resonatoren sind vielversprechende Kandidaten für die Anwendung als vielseitige Quantensensoren und Verbindungen in Quantennetzwerken. Diese Aussicht kommt durch ihre Sensitivität zu unterschiedlichen Kräften, wie z.B. Strahlungsdruck, magnetischen Kräften und kapazitiven Kräften. Hierdurch können mechanische Res-

onatoren an eine Vielzahl von verschiedenen Quantensystemen gekoppelt werden. Prominente Beispiele solcher Systeme sind supraleitende Quantenbits [26, 23, 27, 28], Photonen [29] und Festkörperspins [30, 31, 32, 33, 34]. NV Zentren wurden erfolgreich an mechanische Resonatoren, in Form von Cantilevern [33, 35, 36, 37, 38], Volumenwellen Resonatoren [39, 40], Membranen [34] und akustischen Oberflächenwellen [41] gekoppelt. Allerdings beschränkten sich bisherige experimentelle Anstrengungen ausschließlich auf einzelne mechanische Resonatoren. In dieser Arbeit werden etablierte Methoden zur NV-mechanischen Kopplung auf ein System aus zwei gekoppelten mechanischen Resonatoren erweitert. Zwei mögliche Anwendungen dieses Systems wurden untersucht. Das System ist eine mögliche Architektur für Netzwerke aus mehreren Quantenbits, bei dem die Spin-Spin Wechselwirkung durch Phononen übertragen wird. Ähnliche Hybridsysteme wurden bereits theoretisch untersucht [42], aber nicht experimentell realisiert. Die zweite Anwendung ist hoch-sensitive Massenbestimmung, wo durch eine teilweise Lokalisierung der gemeinsamen mechanischen Moden auf die Massendifferenz zwischen den Cantilevern geschlossen werden kann. Unter den richtigen experimentellen Bedingungen führt dies zu einer höheren Sensitivität verglichen mit Einzelcantilever-Systemen, bei denen die Masse durch eine Änderung der Resonanzfrequenz gemessen wird. Das untersuchte System besteht aus zwei gekoppelten Diamantcantilevern, welche eine zufällige Verteilung von oberflächennahen NV Zentren enthalten. Die Cantilever sind über eine dünne Basisplatte, welche beide von ihnen hält, elastisch gekoppelt.

In einem ersten Schritt wurde eine genaue Charakterisierung des mechanischen Teilsystems durchgeführt. Zu diesem Zweck wurden mechanische Schwingungen mit einem piezoelektrischen Element, welches auf dem Probenhalter angebracht ist, angeregt. Die Bewegung der Cantilever wurde durch ein rein optisches Verfahren gemessen, welches auf der zeitaufgelösten und phasengeregelten Detektion von Laserlicht, reflektiert von der Probenoberfläche, beruht. Dies ermöglicht simultan die Frequenz, Phase und Amplitude der Cantileverschwingungen zu bestimmen. Zusätzlich erlaubt das Rastern des Lasers das Abbilden der dazugehörigen Modenform. Dies ist nötig, um die symmetrische und antisymmetrischen Mode des Cantileverpaares eindeutig zu identifizieren. Die analysierten Cantilever haben eine Größe von ca. 100x5x2.5 µm, besitzen Reso-

nanzfrequenzen von ca. 1 MHz und zeigen einen Gütefaktor von $Q \approx 10^3$ unter normalen Raumbedingungen. Bei tiefen Temperaturen und unter ultra-hoch Vakuum werden Gütefaktoren von bis zu $Q_{\mathrm{LT,UHV}} \approx 10^6$ beobachtet.

Zwei verschiedene Methoden zur Erzeugung einer Spin-Phononen-Kopplung wurden verwendet. Die Kopplung wurde entweder durch die intrinsische Verspannung durch eine Biegung der Cantilever erzeugt, oder durch einen hohen Magnetfeldgradienten, der positionelle Änderungen des NV Zentrums in ein effektives Magnetfeld transformiert. Die höchste Verspannung in einem gebogenen Cantilever entsteht am Klemmpunkt und in der Nähe der Oberfläche des Cantilevers. Für oberflächennahe NV Zentren, die sich am Klemmpunkt befinden, wurde eine spannungsübertragene Spin-Phonon-Kopplung von $g_{\mathrm{str}} = 2\pi \times (2.14 \pm 0.08)$ mHz bestimmt. Eine ca. 1000-fach höhere Spin-Phonon-Kopplung von $g_{\mathrm{mag}} = 2\pi \times (0.87 \pm 0.03)$ Hz wurde mit einem hohen Magnetfeldgradienten erreicht. Der Magnetfeldgradient wurde mit einer selbstgemachten magnetischen Spitze, welche ca. 50 nm über dem NV Zentrum positioniert wurde, erzeugt. Die Spitze wurde dabei mit einem Rasterkraftmikroskop positioniert. Der Magnetfeldgradient übersetzt Biegungen des Cantilevers in ein effektives Magnetfeld an der Position des NV Zentrums. Mit dieser Methode wurde ein Magnetfeldgradient von $\delta B_z = (1.8 \pm 0.1) \times 10^5$ T/m erreicht. Im Vergleich zur spannungsübertragenen Kopplung, leidet diese Methode unter Drift der magnetischen Spitze und einer Verkürzung der Kohärenzzeit des NV Zentrum durch, von der magnetischen Spitze ausgehendem, magnetischem Rauschen.

Ein wichtiger Leistungsindikator eines Hybridsystems ist die Kooperativität C, welche dem Verhältnis zwischen der internen Kopplungsstärke und den Verlusten des Systems entspricht. Im Falle eines Spin-mechanischen Hybridsystems ist die Kooperativität definiert als $C = g^2/\Gamma_s\Gamma_m$, wobei Γ_s die Dekohärenz des Spins und Γ_m die Phononzerfallsrate ist. Ein wichtiger Bereich ist $C > 1$, in dem die Spin-Phonon Wechselwirkung kohärent wird und Verschränkung zwischen Spins und Phononen erzeugbar sind. Unter normalen Raumbedingungen ist die Kooperativität des untersuchten System unter $C < 10^{-6}$. Allerdings wird gezeigt, das Verbesserungen der experimentellen Umgebung eine Kooperativität von größer als Eins ermöglichen. Dabei ist die schwerste Aufgabe die Verkleinerung der mechanischen Struktur bei gleichzeitiger Verbesserung der Spineigenschaften des NV Zentrums.

Ein gekoppeltes Cantileverpaar kann nur als Quantenbus verwendet werden, wenn die Spins an dieselbe mechanische Mode gekoppelt sind. Um experimentell zu zeigen, dass diese Voraussetzung im untersuchten System erfüllt ist, wurde die charakteristische Cantileverschwingung, der symmetrischen und antisymmetrischen gemeinsamen Mode, erfolgreich in den Elektronenspinzustand des NV Zentrums übertragen. Dies wurde unter der Verwendung einer dynamischen Entkopplungssequenz (XY8) erreicht, welche an das Anregungssignal der mechanischen Schwingung phasengekoppelt wurde.

In einem weiteren Schritt wurde die piezoelektrische Schwingungsanregung der kompletten Probe durch eine photothermische Anregung eines einzelnen Cantilevers ersetzt. Hierfür wurde der Cantilever periodisch mit einem Infrarotlaser erhitzt. Die Rate der Laserpulse wurde dazu an die Resonanzfrequenz des Cantilevers angepasst. Die angeregte Schwingung kann mit NV Zentren in beiden Cantilevern beobachtet werden. Dies beweist eine Phononenbasierte Transmission einer lokalen Kraft zu einem entfernten Spin der sich in einem anderen mechanischen Resonator befindet. Die Suszeptibilität des Spins auf die photothermische Kraft ermöglicht die Berechnung einer klassischen Obergrenze für die effektive Kopplung zwischen Spins in unterschiedlichen Cantilevern. Unter normalen Raumbedingungen wird eine maximale Kopplung von $g_{\text{s-s}} = 60.1$ mHz erwartet. Diese Kopplung ist zu schwach, um unter den vorliegenden experimentellen Bedingungen, beobachtet zu werden. Trotzdem zeigen die durchgeführten Experimente, dass Register aus gekoppelten Cantilevern als Quantenbus in Quantennetzwerken fungieren können.

Ein wichtiges Kriterium für Quantennetzwerke ist ihre Skalierbarkeit. Die maximale Anzahl an Cantilevern N_{max} im untersuchten System ist durch zwei Effekte limitiert. Zum Ersten nimmt die Gesamtmasse des Systems mit steigender Anzahl an Cantilevern zu. Simulationen mit der Finite-Elemente-Methode (FEM) zeigen, dass die effektive Masse des Cantileverregisters näherungsweise linear mit der Anzahl der Cantilever zunimmt. Dies führt zu einer Abnahme der Spin-Phonon-Kopplung mit einer Skalierung von $g \propto \frac{1}{\sqrt{N}}$.

Zum Zweiten führt eine Erhöhung der Anzahl an Cantilevern zu einer entsprechendem Zunahme der mechanischen Moden, und damit Modendichte. Bei zu hohen Modendichten können einzelne mechanische Moden nicht mehr individual adressiert werden. Mit FEM Simulationen wurde gezeigt, dass bei einem Güte-

faktor von $Q = 10^6$ eine maximale Anzahl an Cantilevern $N_{max} > 100$ verwendet werden kann.

Diese Limitierungen können umgangen werden, indem man ein großes Register in kleinere Unterregister unterteilt. Indem man die Unterregister über eine schaltbare kapazitive Wechselwirkung koppelt, können die individuellen Register bei Bedarf isoliert werden und für einen Datentransfer wieder gekoppelt werden. Diese Methode wurde detailliert in der Arbeit von Rabl et al. diskutiert [42].

List of Figures

List of Tables

List of Abbrevations

AC	alternating current
AFM	atomic force microscope
APD	avalanche photo diode
AWG	arbitrary-waveform Generator
CPMG	Carr-Purcell-Meiboom-Gill
CVD	chemical vapor deposition
CW	continuous wave
DC	direct current
DEER	double electron-electron resonance
DPSS	diode-pumped solid state
ES	excited state (of the NV)
ESR	electron-spin resonance
FEM	finite element method
FFT	fast Fourier transformation
FID	free induction decay
FPGA	field-programmable gate array
FWHM	full width at half maximum
GS	ground state (of the NV)
HPHT	high-pressure high-temperature
HWHM	half width at half maximum
IR	infrared
LT	low temperature
MRI	magnetic-resonance imaging
MW	microwave
NA	numerical aperture
NSL	nitroxide spin label
NMR	nuclear-magnetic resonance

NV center	nitrogen-vacancy center in diamond
ODMR	optically detected magnetic resonance
PLL	poly-L-lysine
PSB	phonon side band
QND	quantum non-demolition
RF	radio frequency
RMS	root mean square
RT	room temperature
SDSL	site directed spin labeling
SEM	scanning electron microscope
SL	spin label
SMF	single mode fiber
SNR	signal-to-noise ratio
SPM	scanning-probe microscopy
SSR	single-shot readout
T_1	longitudinal relaxation time
T_2	transverse relaxation time
TF	tuning fork
TTL	transistor-transistor logic
UHV	ultra-high vacuum
ZFS	zero field splitting
ZPL	zero phonon line

Chapter 1

1 The Nitrogen Vacancy Center In Diamond

Contents

The NV center is one of over 500 known color defects in diamond [43, 44]. However, its outstanding properties make it the most promising one for quantum applications to date. In this chapter, the structure, properties and sensing capabilities of the NV center are discussed.

1.1 Diamond

Diamond is a metastable phase of carbon. It has a tetrahedral lattice structure, where the carbon atoms are covalently bond by sp^3 orbital hybrids. The compact structure and strong covalent bonds make diamond the hardest naturally occurring material. Its very high Young's modulus of $E \approx 1200$ GPa [45, 46] makes it an excellent material for high frequency mechanical resonators. At the same time, such diamond mechanical resonators exhibit high quality factors of over 10^6 at low temperatures due to low mechanical losses in diamond [47, 48, 49]. This stems from low thermoelastic dissipation that is linked to the extraordinarily high thermal conductivity of ≈ 2000 W m^{-1} K^{-1} [50, 51]. Besides its mechanical stability, diamond is also chemically inert, making it an interesting material for biological applications.

Diamond has a wide band gap of 5.5 eV at room temperature, making it transparent over a wide spectral range from infrared to far ultraviolet [52]. Importantly, this allows to observe single color centers - like the NV center - embedded in diamond. These crystal defects, in particular, make diamond an interesting platform for quantum devices [53].

Due to its outstanding properties, there is a high demand for diamond in industry and science. Here, mostly synthetic diamonds are used. The two most common methods for diamond fabrication are chemical vapor deposition (CVD) and high pressure, high temperature synthesis (HPHT). These methods allow to control the exact composition of the produced diamonds. For example, the concentration of different types of impurities or the ratio between ^{13}C and ^{12}C can be controlled.

1.2 Structure of the nitrogen vacancy center

The NV center is a defect center consisting of a substitutional nitrogen atom (N) and an adjacent vacancy (V) in the carbon lattice. An illustration of the NV center structure is shown in Fig 1.1. The NV center has a symmetry axis along the line connecting both lattice sites occupied by the NV center. In the following, this axis is simply referred to as the NV axis. In accordance with the tetrahedral lattice, the NV center can be oriented along four different direction of covalent bonds.

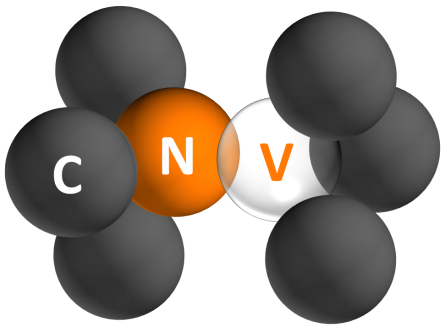

Figure 1.1: Illustration of the NV center in diamond. The NV center is composed of a substitutional nitrogen atom (N) and an adjacent vacancy (V) in the carbon lattice (C).

NV center occur naturally in diamond but can also be artificially created. The formation of NV centers first requires nitrogen impurities in the diamond lattice. These impurities can either be incorporated during the diamond synthesis or implanted afterwards by ion-irradiation. Former leads to NV centers equally distributed throughout the diamond, while latter will create NV centers close to the surface, so-called shallow NV centers. By subsequent annealing, vacancies in the diamond lattice get mobile and start to diffuse through the crystal, eventually forming stable NV centers.

Shallow NV centers are well-suited for quantum sensing application as they can be positioned close to potential samples outside of the diamond crystal. However, there spin properties are typically deteriorated by magnetic and electric noise emanating from the diamond surface [54, 55, 56, 57, 58]. This influence can be mitigated by advanced fabrication techniques [59, 60, 61]. The NV

centers used in this work are exclusively created via ^{15}N ion-implantation at energies of 5-10 keV. The average depth of such NV centers is 5-20 nm.

NV centers can have different charge states, the most prominent ones being NV^- and NV^0. In this thesis, only NV centers in the NV^- state are used. Hence, the following sections will solely focus on this charge state. From here on, the NV center in its negatively charged state will be simply referred to as "NV center".

1.3 Optical properties of the NV center

The NV^- charge state has two unpaired electron, forming an electron spin triplet ($S = 1$). Fig 1.2 shows a depiction of the electronic energy levels and dominant transitions of the NV center.

The ground state ($^3A_2$) and excited state (^3E) are separated by an energy of 1.945 eV and both lie within the diamond band gap [62]. Accordingly, the NV center has a zero-phonon line (ZPL) at a wavelength of $\lambda = 637$ nm. The ZPL is accompanied by a temperature-dependent phonon side band (PSB). At room temperature, the emissions ranges from ~600-800 nm. A photoluminescence emission (PLE) spectrum is shown in Fig 1.3. The NV center can be excited off-resonantly with green laser light ($\lambda = 515 - 532$ nm) [63]. The direct radiative transitions between the ^3E and $^3A_2$ states are spin conserving and feature decay rates of around $\gamma \approx 1/10$ ns^{-1} for both spin states.

An alternative decay channel is provided by the singlet states $^1A_1$ and ^1E [64, 65, 66]. The non-radiative inter-system crossing (ISC) transition from the ^3E triplet to the $^1A_1$ singlet state is spin state selective. The transitions predominantly occurs from the exited $m_s = \pm 1$ sublevels to the singlet state. From the $^1A_1$ state, the system relaxes into the ^1E singlet state by emitting a photon at a wavelength of $\lambda \approx 1042$ nm at a decay rate of $\gamma \approx 1/250$ ns^{-1} [64], and subsequently into the $^3A_2$ manifold. The ISC via the singlet states is responsible for two key features of the NV center - optical spin polarization and readout.

Overall, the ISC decay channel preferably transfers the system from excited $m_s = \pm 1$ spin state to the $m_s = 0$ sublevel of the ground state. As all other transitions are spin conserving, optically pumping of the NV center leads to a partial polarization of the spin into the $m_s = 0$ state. Spin polarizations of ~80%

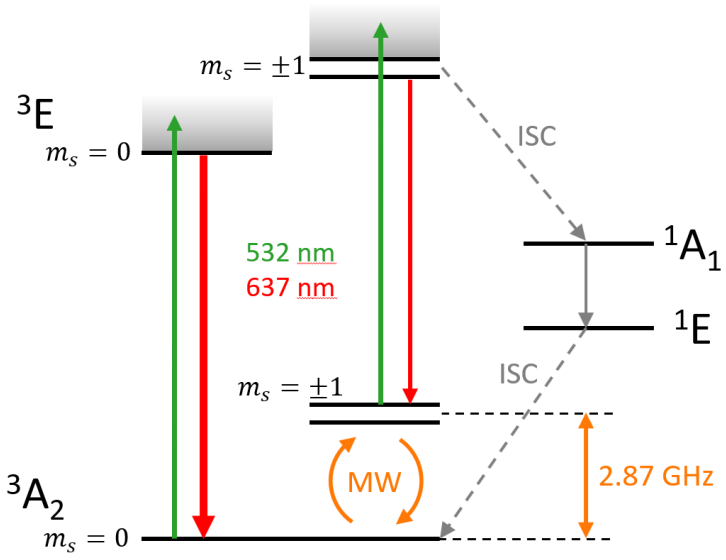

Figure 1.2: Illustration of the electron energy level structure and corresponding dominant transitions of the negatively charged NV center. The ground state (^{3}A$_2$) and excited state (^{3}E) are spin triplet states. The ground $m_s = \pm 1$ spin states are separated from the $m_s = 0$ spin state by the zero-field splitting (ZFS) $D = 2.87$ GHz. The additional singlet states ^{1}A$_1$ and ^{1}E offer an inter-system crossing (ISC). This decay channel is spin-selective and predominantly transfers the system from the excited $m_s = \pm 1$ spin states to the $m_s = 0$ sublevel of the ground state manifold. The ISC enables optical polarization and readout of the NV centers spin state.

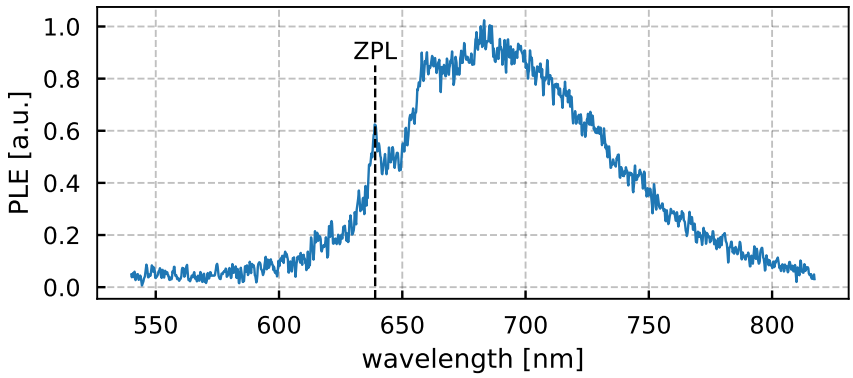

Figure 1.3: Photoluminescence emission (PLE) spectrum of a negatively charged NV center (NV^-) at room temperature. The dashed line indicates the zero-phonon line (ZPL) at 637 nm. The phonon side band (PSB) ranges from ~600-800 nm.

are achieved at room temperature [65].

The photon emission rate of the $m_s = \pm 1$ spin states is reduced by the alternative decay channel offered by the ISC. Due to the slow decay rate between the singlet states compared to the triplet states, the system is shelved in the single state for a relatively long time. Furthermore, the photons associated with the singlet state transition have an wavelength far away from the NV centers PSB and can thus be filtered out easily. Hence, the $m_s = \pm 1$ spin states are also known as the dark states and $m_s = 0$ as the bright state. Typically, a fluorescence contrast of ~30% between the spin states is observed.

The $m_s = 0$ and $m_s \pm 1$ sublevels of the ground state triplet are separated by the zero-field splitting (ZFS) $D = 2.87$ GHz [62, 67]. The transition between the spin states can be driven with resonant microwave (MW) radiation. This manipulation of the spin state, known as magnetic resonance, is discussed in detail in Section 1.4.2. Fig 1.4 shows the fluorescence of a NV center under continuous optical excitation ($\lambda = 532$ nm) and exposed to MW radiation of varying frequency. Due to the optical excitation, the NV center is pumped into the $m_s = 0$ spin state and thus shows a high fluorescence (indicated by the dashed blue line in Fig 1.4). When the MW is resonant with the spin transition ($f \approx 2.87$ GHz), the spin state is partially transfered into $m_s = \pm 1$, which results in a decreased fluorescence (indicated by the dashed red line in Fig 1.4). This optical measure-

ment of the spin state transition is also known as optically detected magnetic resonance (ODMR).

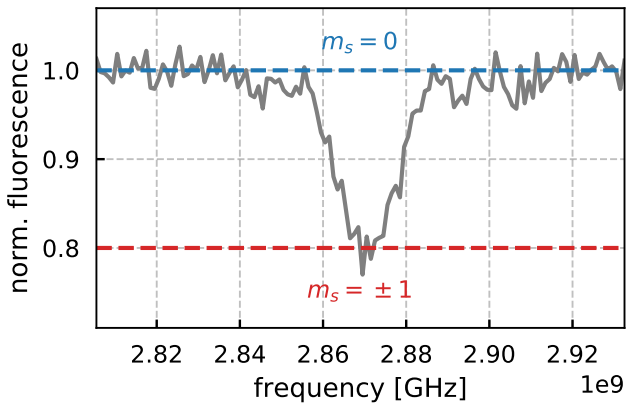

Figure 1.4: Optically detected magnetic resonance (ODMR) of a NV center. The fluorescence of a NV center under continuous optical excitation is recorded. The NV center is exposed to microwave (MW) radiation of varying frequency. The NV center is polarized into the $m_s = 0$ by the optical excitation. The fluorescence level associated with this spin polarization is indicated by the blue dashed line. When the MW frequency is resonant to the spin state transition ($f = 2.87$ GHz), the NV center is driven into the $m_s = \pm 1$ spin states. This is observed as a reduced fluorescence (red dashed line).

1.4 Spin dynamics

This section highlights the spin dynamics of the ground state manifold of the NV center. The influence of magnetic fields and the intrinsic coupling to the nitrogen atom is discussed. The coupling of the NV center to strain is discussed in Section 5.5.1.

1.4.1 Spin Hamiltonian

The ground state manifold of the NV center in a magnetic field $\underline{B}$ is described by the Hamiltonian

$$\hat{H} = \underbrace{D\hat{S}_z^2}_{\text{ZFS}} + \underbrace{\gamma_{\text{NV}}\underline{B}\cdot\underline{\hat{S}}}_{\text{Zeeman}} + \underbrace{\underline{\hat{S}}\cdot\underline{\underline{A}}\cdot\underline{\hat{I}}}_{\text{hyperfine}}. \tag{1.1}$$

Here, $D = 2.87$ GHz is the zero-field splitting (ZFS), $\gamma_{\text{NV}} = 28$ GHz T^{-1} is the gyromagnetic ratio of the NV electron spin, $\underline{\hat{S}}$ are the spin operators of the electron spin, $\underline{\hat{I}}$ are the spin operators of the nitrogen nuclear spin[1] and $\underline{\underline{A}}$ is the hyperfine tensor.

The first term of the Hamiltonian describes the ZFS caused by the spin-spin interaction between the two unpaired electrons of the NV center. The second term governs the influence of magnetic fields described by the Zeeman effect. In the experiments presented in this work, all static magnetic fields are aligned along the NV axis (z-axis). Thus, only this case is discussed in the following. The absence of transverse magnetic fields reduces the Zeeman term to $\hat{H}_{\text{Zeeman}} = \gamma_{\text{NV}} B_z \hat{S}_z$, with the eigenstates $|m_s = 0\rangle$, $|m_s = -1\rangle$ and $|m_s = +1\rangle$ and the corresponding magnetic field dependent eigenvalues $\lambda_{|0\rangle} = 0$, $\lambda_{|-1\rangle} = -\gamma_{\text{NV}} B_z$ and $\lambda_{|+1\rangle} = +\gamma_{\text{NV}} B_z$. Hence, a static magnetic field leads to a splitting of $2\gamma_{\text{NV}} B_z$ between the $m_s = \pm 1$ sublevels (see Fig 1.5a), allowing to distinguish the two transitions in an ODMR experiment as shown in Fig 1.5b.

The last term of the Hamiltonian describes the hyperfine structure caused by the intrinsic nitrogen nuclear spin of the NV center. In the NV centers coordinate system, $\underline{\underline{A}}$ is a diagonal tensor with the elements $A_{xx} = A_{yy} = A_\perp$ and $A_{zz} = A_\parallel$. Using the spin ladder operators $S_\pm$ and $I_\pm$, the hyperfine Hamiltonian can be written as [20, 65]

$$\begin{aligned} \hat{H}_{\text{HF}} &= \underline{\hat{S}}\cdot\underline{\underline{A}}\cdot\underline{\hat{I}} \\ &= \frac{A_\perp}{2}(S_+ I_- + S_- I_+) + A_\parallel \hat{S}_z \hat{I}_z. \end{aligned} \tag{1.2}$$

The first two terms induce flip-flop processes between the electron and nuclear spin, while the last term leads to a hyperfine splitting of the $m_s = \pm 1$ spin states.

[1] Coupling of the NV center's electron spin to other nuclear spins, like e.g. ^{13}C spins in the diamond lattice, is ignored at this point, as they only indirectly influence the experiment presented in this work by a reduction of coherence times.

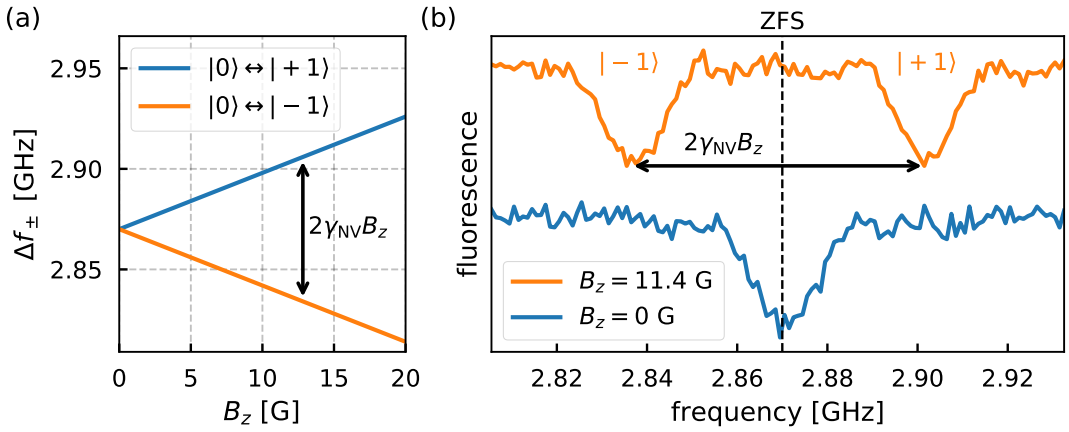

Figure 1.5: **(a)** Magnetic field dependence of the transitions frequencies $\Delta f_\pm$ between the $|m_s = 0\rangle$ and $|m_s = \pm 1\rangle$ spin states. Without a magnetic field, the $|m_s = \pm 1\rangle$ states are degenerate. A magnetic field introduces a splitting of $2\gamma_{NV}B_z$ between the two transitions. **(b)** ODMR measurement of the NV centers spin transitions with and without a magnetic field. The bias magnetic field removes the degeneracy of the spin states and allows to address the $|0\rangle \leftrightarrow |-1\rangle$ and $|0\rangle \leftrightarrow |+1\rangle$ transitions individually (orange).

The hyperfine splitting depends on the nitrogen isotope incorporated into the NV center. ^{15}N has a spin of $I = \frac{1}{2}$ an splits the spin states into two sublevels with a separation of $A_{\parallel}(^{14}\mathrm{N}) = 3.02$ MHz [68, 69]. ^{14}N results in three sublevels with an equidistant spacing of $A_{\parallel}(^{15}\mathrm{N}) = 2.16$ MHz due to the $I = 1$ nuclear spin [70, 71].

1.4.2 Magnetic resonance and Rabi oscillations

As already mentioned in Section 1.3, spin state transitions in the ground state can be driven by resonant MW radiation. Without loss of generality, the MW field can be viewed as a magnetic field $\mathbf{B_1}(t) = B_1(\mathbf{e}_x \cos\omega t + \mathbf{e}_y \sin\omega t)$ rotating in the xy-plane with frequency ω and amplitude B_1. To analyze the effect of this magnetic field, it is convenient to switch to a reference frame ($\mathbf{e}'_x$, $\mathbf{e}'_y$, $\mathbf{e}_z$) that rotates around the z-axis with the frequency of the applied MW. In this new reference frame, the MW field is static. The effective magnetic field in the rotating frame is [72, 73]

$$B_{\mathrm{eff}} = (B_0 - \frac{\omega}{\gamma_{\mathrm{NV}}})\mathbf{e}_z + B_1\mathbf{e}'_x. \tag{1.3}$$

Ignoring the hyperfine interaction, the Hamiltonian in the rotating frame can be written as

$$\hat{H}' = \underbrace{(D \pm \gamma_{\mathrm{NV}}B_0 - \omega)}_{\Delta_\pm}\hat{S}_z + \gamma_{\mathrm{NV}}B_1\hat{S}_x, \tag{1.4}$$

with $\pm$ corresponding to the spin states $|-1\rangle$ and $|+1\rangle$. $\Delta_\pm$ is the detuning of the MW frequency to energy splitting between the $|0\rangle$ and $|\pm 1\rangle$ spin states. When a detuning is present, the spin will precess around the effective magnetic field B_{eff} that is pointing roughly along the z-axis. At the resonance condition $\Delta_\pm \approx 0$, the effective magnetic field will point along the x-axis of the rotating frame. The resulting spin precession around the x-axis with frequency $\Omega = \gamma_{\mathrm{NV}}B_1$ is also known as a Rabi oscillation, and a fundamental building block of the manipulation of the NV spin.

The rotation of the spin can be visualized using Bloch spheres. For this purpose, the $|1\rangle$ spin state is neglected and the remaining spin state subset

$[|0\rangle,|-1\rangle]$ is regarded as a two-level system.[2] The Bloch sphere allows to represent all possible superpositions states of the two-level system as vectors. The north and south pole represent the eigenstates $|0\rangle$ and $|-1\rangle$. States on the equator correspond to coherent superposition states of the form

$$|\psi\rangle = \frac{1}{\sqrt{2}}\left(|0\rangle + e^{i\phi}|-1\rangle\right), \tag{1.5}$$

where ϕ is a relative complex phase between the two eigenstate components.

A MW pulse transferring the spin state from $|0\rangle$ to $|-1\rangle$ is commonly called π-pulse. The π-pulse length

$$\tau_\pi = \frac{\pi}{\gamma_{\mathrm{NV}} B_1} \tag{1.6}$$

depends on the amplitude B_1 of the MW field. The corresponding rotation on the Bloch sphere is illustrated in Fig 1.9a. Other important MW pulses are the so called $\frac{\pi}{2}$- and $\frac{3\pi}{2}$-pulse shown in Fig 1.9b and Fig 1.9c, respectively. Both pulses transfer the $|0\rangle$-state into a coherent superposition state on the equator. However, the two resulting spin states have a relative phase shift of π. Hence, the states point into opposite directions on the Bloch sphere.

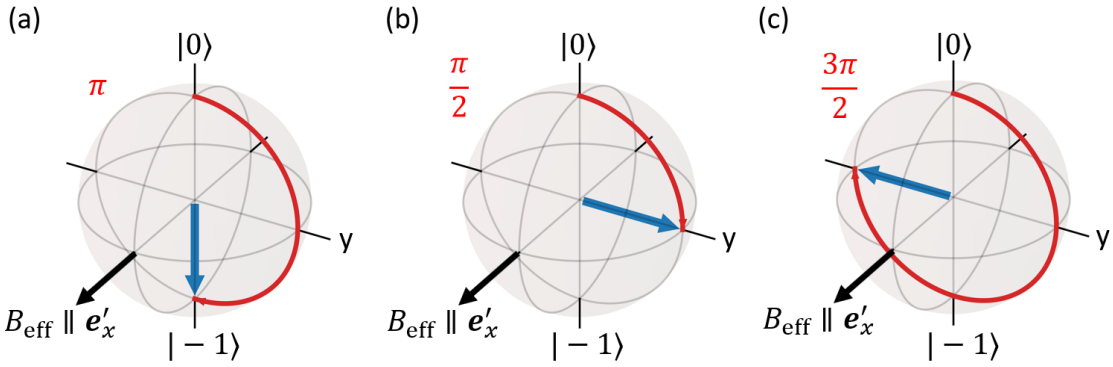

Figure 1.6: Illustration of the rotation caused by resonant MW pulses of different lengths. The rotation angle depends on the amplitude and duration of the MW pulse. Depicted is a **(a)** π-, **(b)** $\frac{\pi}{2}$- and **(c)** $\frac{3\pi}{2}$-pulse.

If the MW frequency is detuned from the spin state transitions frequency ($\Delta_- \neq 0$), the axis of the spin precession is tilted by an angle $\theta = \arctan(\Delta_-/\Omega)$.

[2] This approximation is valid in the presence of a bias magnetic field along the NV axis, lifting the degeneracy of the $|m_s = \pm 1\rangle$ spin states.

In this case, the spin undergoes a Rabi oscillation with the effective Rabi frequency [74]

$$\Omega_{\text{eff}} = \sqrt{\Omega^2 + \Delta_-^2} \tag{1.7}$$

and the reduced amplitude

$$A = A_0\left(\frac{\Omega}{\Omega_{\text{eff}}}\right)^2, \tag{1.8}$$

where A_0 is the amplitude of a resonant Rabi oscillation ($\Delta_- = 0$). As the optical readout is essentially a measurement of the spin state projected onto the z-axis, the detected spin signal of a single rectangular MW pulse of duration τ is

$$S(\Delta_-, \tau) = A_0\left(\frac{\Omega}{\Omega_{\text{eff}}}\right)^2 \cos(\Omega_{\text{eff}}\tau). \tag{1.9}$$

1.5 Pulsed experiments

1.5.1 Pulsed optical readout experiments

The optical polarization and readout capabilities allow to control and observe the spin dynamics of the NV centers electron spin. Experiments utilizing the NV spin mainly follow the same basic recipe, which is illustrated Fig 1.7a. First, a green laser pulse polarizes the spin into the $|m_s = 0\rangle$ state. Afterwards, the spin is manipulated by a sequence of MW pulses to perform a specific experiment. Examples of such MW sequences are discussed in the following sections. Finally, a second green laser pulse is used to readout and repolarize the spin. The final laser pulse is typically used as the first pulse of the next experimental cycle. The fluorescence response of the NV center to the readout laser pulse is shown in Fig 1.7b. At the beginning of the laser pulse, the fluorescence depends on the spin state, with the $|m_s \pm 1\rangle$ states showing a smaller photon emission rate. After ~300 ns the spin is repolarized by the optical pumping.[3] To extract the spin signal, the number of photons ν collected during the first 300 ns of the laser pulse ("signal" in Fig 1.7b) are compared to the number of photons ν_r collected in a reference window after repolarization of the spin ("reference" in

[3] The time needed to repolarize the spin depends on the laser intensity. The time values mentioned in the main text are typical values for NV centers excited with their saturation power.

Fig 1.7b). The spin signal referred to in this work is defined as

$$\mathcal{S}_{\text{spin}} = \frac{\nu}{\nu_{\text{r}}}. \tag{1.10}$$

Using a reference photon count rate makes the experiment robust against slow fluctuations of the fluorescence.

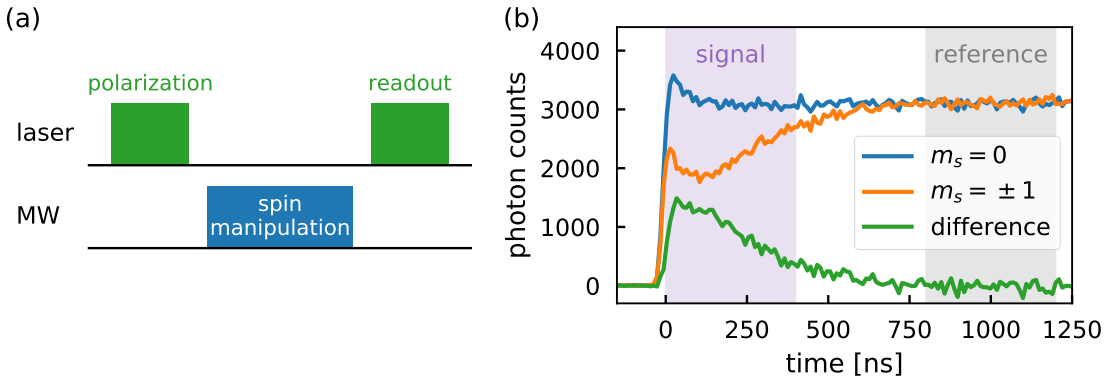

Figure 1.7: **(a)** Illustration of the basic recipe of a pulsed NV center experiment. The NV spin is polarized by a first green laser pulse. Afterwards, the spin is manipulated by a sequence of MW pulses to perform a certain experiment. Finally, a second green laser pulse is used to readout the spin state and repolarize the spin. **(b)** Fluorescence response of a NV center in the $|m_s = 0\rangle$ (blue) and $|m_s = \pm 1\rangle$ (orange) spin states. During the beginning of the laser pulse the fluorescence depends on the spin state. After ≈ 300 ns the spin is repolarized by the optical excitation. The spin signal is extracted as the ratio between the photons collected during the time windows labeled "signal" and "reference".

1.5.2 Spin relaxation

The easiest example of a pulsed experiment is the measurement of the longitudinal spin decay. The pulse sequence is depicted in Fig 1.8a. During the waiting time τ between the laser pulses, the spin state is decaying according to its longitudinal relaxation time T_1. The T_1 time describes the relaxation of NV

center's electron spin from a polarized state, back into thermal equilibrium. The measurement is alternating between two different spin manipulation sequences MW_0 and MW_π. While the first sequence does not contain any active spin manipulation, the spin is flipped by a π-pulse just before the optical readout in the second sequence (see Fig 1.8c (ii)). The corresponding spin signals $\mathcal{S}_0$ and $\mathcal{S}_\pi$ are collected separately. Fig 1.8b shows the spin signals recorded for a NV center with a spin lifetime of $T_1 \approx 108$ µs. The final measurement result is the spin contrast $\Delta\mathcal{S} = \mathcal{S}_0 - \mathcal{S}_\pi$, plotted in Fig 1.8d. In total, the spin contrast is calculated by using four different photon counts (see Eq. (1.10))

$$\Delta\mathcal{S} = \frac{\nu_0}{\nu_{0,\mathrm{r}}} - \frac{\nu_\pi}{\nu_{\pi,\mathrm{r}}}. \tag{1.11}$$

1.5.3 Rabi oscillation

Fig 1.9a shows a Rabi oscillation of a NV center exposed to a resonant MW ($\Delta_\pm = 0$). The spin signal was recorded with the pulsed detection technique discussed in Section 1.5.1. The used pulse sequence is depicted in the inset in Fig 1.9a. Between the polarization and readout laser pulse, a Rabi oscillation of the NV spin is driven by a resonant MW pulse of varying length τ. Without a MW pulse ($\tau = 0$ ns), the spin is in the $|m_s = 0\rangle$ state, which corresponds to a normalized fluorescence of 1. With increasing length of the MW pulse, the spin rotates around the x-axis and eventually ends up in the $|m_s = -1\rangle$ spin state ($\tau \approx 60$ ns).

Fig 1.9b shows the representation of the spin state (blue arrow) in the Bloch sphere at different times during the Rabi oscillation. Additionally, the previous rotation of the spin is indicated by the red arrows.

1.5.4 Pulsed ODMR

A pulsed ODMR sequence is typically used to detect the spin state transitions of the NV center. As the transition frequency depends on the magnetic field along the NV axis, the pulsed ODMR can be used as a measurement of static magnetic fields. The pulse sequence follows the basic principle of a pulsed experiment discussed in Section 1.5.1 and is shown in Fig 1.10a. The spin manipulation

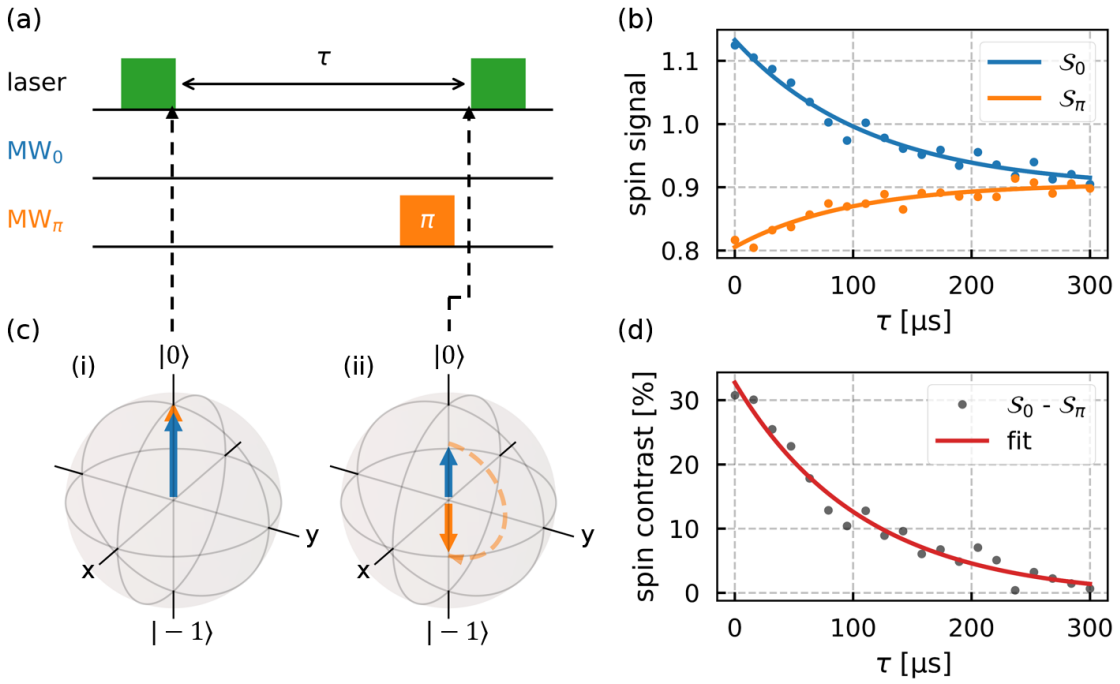

Figure 1.8: Measurement of the longitudinal spin relaxation time (T_1). **(a)** Sequence to measure the T_1 time. First, a laser pulse polarizes the NV electron spin. Afterwards, the spin can evolve freely during the waiting time τ. During the measurement, the MW sequence is alternating between the MW_0 and MW_π variant. Finally, the spin state is readout via a second laser pulse. **(b)** Signals recorded with the MW_0 (blue) and MW_π (orange) sequence. **(c)** Illustration of the spin evolution during the sequence. After the first laser pulse the spin is initialized into the $m_s = 0$ state. During the waiting time, the spin state decays according to its T_1 time. The π-pulse of the MW_π sequence inverts the spin. **(d)** The final result of the measurement is the so-called spin contrast $\Delta\mathcal{S} = \mathcal{S}_0 - \mathcal{S}_\pi$, which is the difference between the signals obtained with the MW_0 and MW_π sequences.

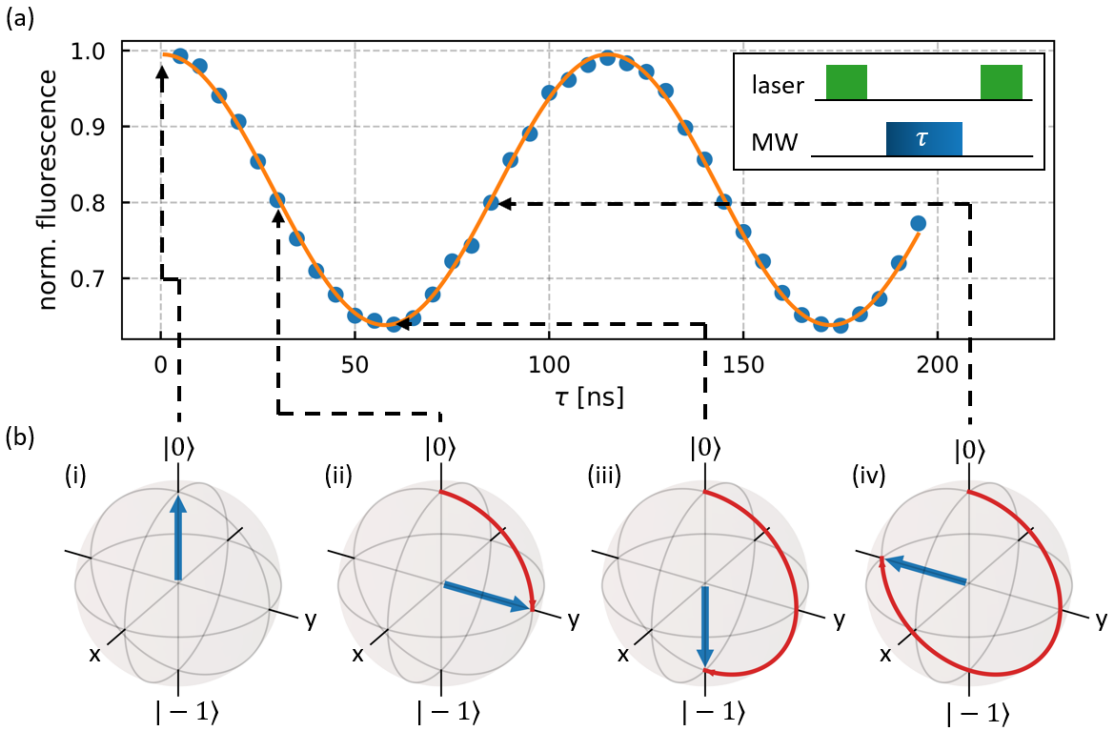

Figure 1.9: **(a)** Rabi oscillations of NV spin recorded with the pulse sequence depicted in the inset. After polarization of the spin into the $|0\rangle$ state by a first laser pulse, the spin is rotated around the x-axis by a resonant MW pulse. Afterwards, the spin state is readout using a second laser pulse. The rotation angle of the spin is defined by the length τ of the MW pulse. **(b)** Representation of the spin states (blue arrow) at different times of the Rabi oscillation using Bloch spheres. The undergone rotations of the spin are indicated by the red arrows. Sub-figures (ii), (iii) and (iv) correspond to $\frac{\pi}{2}$-, π- and $\frac{3\pi}{2}$-pulses, respectively.

consists of a single rectangular MW pulse. By varying the MW frequency, the resonance peak of spin transition is recorded. The MW pulse is supposed to transfer the spin from the $m_s = 0$ to the $m_s = -1$ spin state at the resonance condition $\Delta_- = 0$. This way, the amplitude of the resonance peak is maximized. Accordingly, the pulse duration should fulfill the π-pulse condition

$$\tau_\pi = \frac{\pi}{\Omega_{\text{eff}}(\Delta_- = 0)} = \frac{\pi}{\Omega}. \tag{1.12}$$

A spin signal recorded with a pulsed ODMR sequence is shown in Fig 1.10b. The resonance peak corresponds to the $|0\rangle \leftrightarrow |+1\rangle$ transition at a static magnetic field along the NV axis of $B_z \approx 350$ G. The measured spin signal (gray) was fitted using Eq. (1.9) (red).

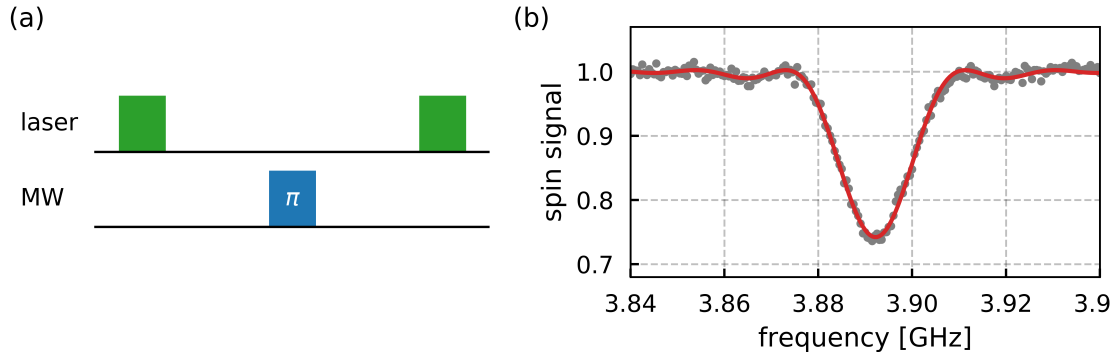

Figure 1.10: **(a)** Pulse sequence of a pulsed ODMR measurement. The NV spin is first polarized into the $|0\rangle$ spin state by a green laser pulse. Afterwards, the spin is rotated by a MW pulse of length τ. Subsequently, a second laser pulse is used to readout the spin state and repolarize the spin. **(b)** Spin signal recorded with a pulsed ODMR sequence. The MW frequency is swept to acquire a spectrum of the spin state transition. The observed resonance peak corresponds to the $|0\rangle \leftrightarrow |+1\rangle$ transition at a static magnetic field along the NV axis of $B_z \approx 350$ G.

1.5.5 Free Induction Decay

An alternative technique to measure static magnetic fields is the free induction decay (FID), also known as Ramsey interferometry [75]. The corresponding

pulse sequence is depicted in Fig 1.11a and a visualization of the spin states at different times during the sequence using Bloch spheres is shown in Fig 1.11d.

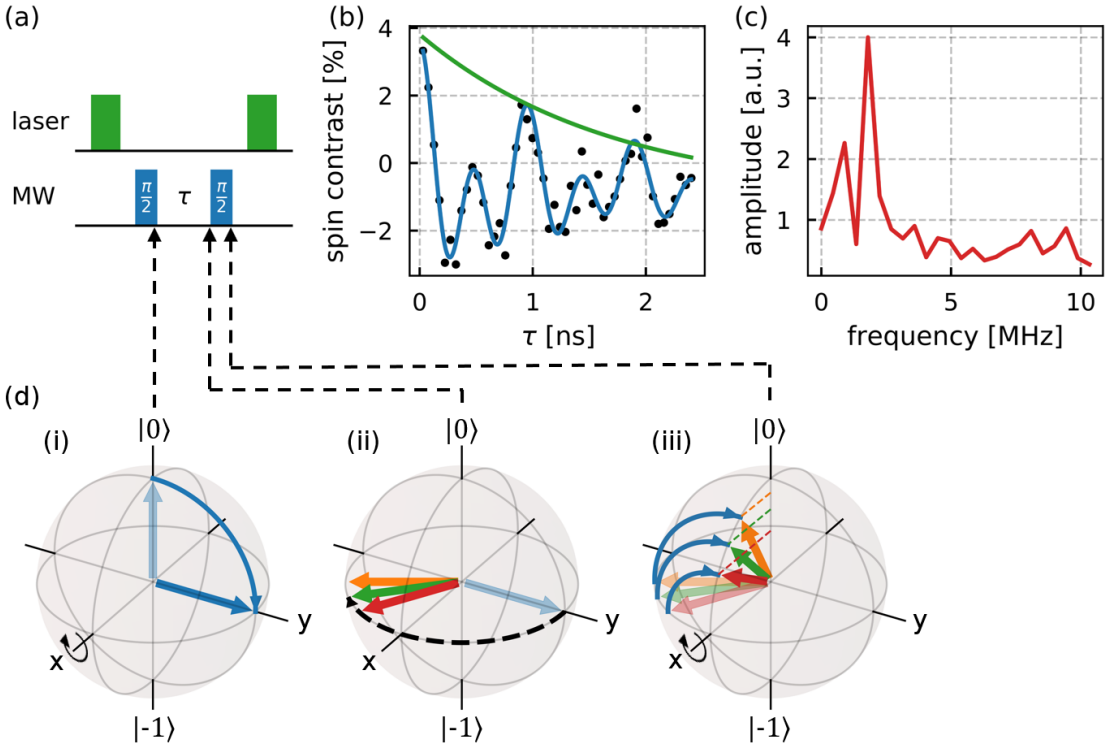

Figure 1.11: Free induction decay (FID) measurement on a NV electron spin. **(a)** FID sequence based on the pulsed measurement scheme described in Section 1.5.2. **(b)** Measured FID signal over the waiting time τ. The electron spin is driven with a MW frequency between the two hyperfine transitions of the NV center. The MW frequency was chosen to be closer two one of the transitions frequencies. As a result, the two different detunings (~1 MHz and ~2 MHz) are visible in the measurement result. **(c)** FFT of the FID signal showing the two detuning frequencies. **(d)** Illustration of the spin evolution during the FID sequence. The first $\frac{\pi}{2}$-pulse creates a superposition state. During the waiting time, the spin state accumulates a phase according to the present magnetic fields and the initial detuning of the MW frequency. The second $\frac{\pi}{2}$-pulse maps the accumulated phase into the spin polarization.

After the optical polarization into the $|0\rangle$ state, the spin is transfered into the coherent superposition state

$$|\psi\rangle = \frac{1}{\sqrt{2}}\Big(|0\rangle + |-1\rangle\Big) \tag{1.13}$$

by a $\frac{\pi}{2}$-pulse resonant with the $|0\rangle \leftrightarrow |-1\rangle$ transition (Fig 1.11d (i)). Afterwards, the spin freely evolves during the waiting time τ. During this time, the spin will precess around the z-axis with the frequency detuning Δ_- (see Eq. (1.4)), accumulating a relative phase $\phi = \Delta_- \tau$ (Fig 1.11d (ii)). The new spin state, after the waiting time τ, is

$$|\psi(\tau)\rangle = \frac{1}{\sqrt{2}}\Big(|0\rangle + e^{i\Delta_- \tau}|-1\rangle\Big). \tag{1.14}$$

Subsequently, the accumulated phase is mapped into the spin polarization (z-axis) by a second $\frac{\pi}{2}$-pulse (Fig 1.11d (iii)), resulting in a spin polarization of $\mathcal{P} \propto \cos(\Delta_- \tau)$. The spin polarization is subsequently read out optically by a second laser pulse. During the free evolution time, the electron spin will also be subject to dephasing, caused by fluctuations of the surrounding spin bath. This results in a decay of the FID signal with increasing τ, which is described by the inhomogeneous transverse relaxation time T_2^*. The signal of a FID measurement can be described by

$$S(\tau) = e^{-\frac{\tau}{T_2^*}} \sum_i A_i \cos(\Delta_i \tau + \phi_i) + c, \tag{1.15}$$

where i denotes all present detunings.

The result of a FID measurement is shown in Fig 1.11b. The MW frequency was chosen to be between the two hyperfine split resonances of the NV center's electron spin. As a result, two different oscillations stemming from two different detunings are observed in the FID signal. Fig 1.11c shows a FFT of the FID signal, revealing the two detuning frequencies (~1 MHz and ~2 MHz).

1.5.6 Hahn echo

The Hahn echo sequence can be used to suppress the influence of constant or slowly fluctuating magnetic fields [76]. For this purpose, an additional π-pulse

is added to the FID sequence, discussed in the previous section. The Hahn echo pulse sequence and the corresponding evolution of the spin state on the Bloch sphere is depicted in Fig 1.12. The first $\frac{\pi}{2}$-pulse creates a superposition state. Afterwards, the spin state accumulates a phase due to external magnetic fields. Subsequently, the spin is rotated by the π-pulse and will again accumulate a phase during the second waiting time. If the magnetic field during the both waiting times is identical, the accumulated phases will cancel each other. Hence, the effect of static magnetic fields is suppressed. At the same time, phase accumulated from AC magnetic fields with periods close to 2τ will be increased. Thus, the Hahn echo sequence can be seen as a frequency filter with a central frequency of $f_{\text{Hahn}} = \frac{1}{2\tau}$. Consequently, the Hahn echo can be used to perform NMR spectroscopy, by varying the waiting time τ.

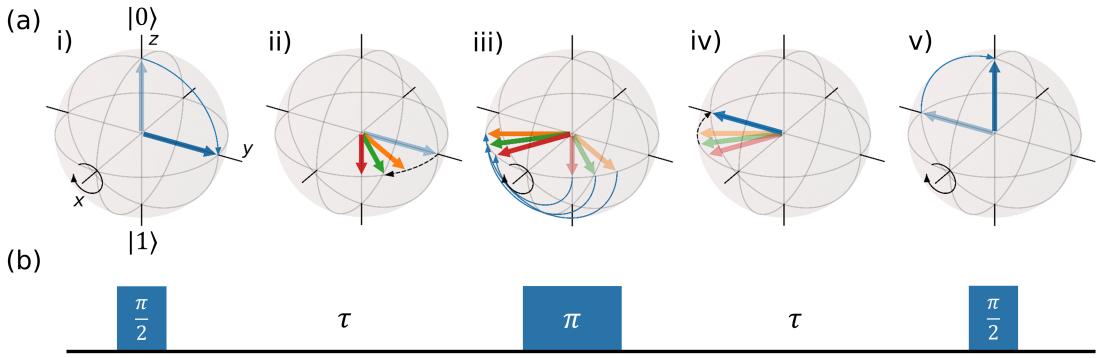

Figure 1.12: Illustration of the Hahn echo sequence **(b)** and the corresponding evolution of the spin state on the Bloch sphere **(a)**. A superposition state is created by the initial $\frac{\pi}{2}$-pulse. The spin state accumulated a phase during the first waiting time (τ) according to the magnetic field. Subsequently, a π-pulse refocuses the spin state by a 180° rotation. For a constant magnetic field, the accumulated phase in the second waiting time will cancel out the phase of the first waiting time, thus suppressing the influence of constant or slowly fluctuating fields. In contrast, the signal from AC magnetic fields with frequencies matching the period of the Hahn echo sequence will be amplified. Hence, the Hahn echo acts as a frequency filter.

A result of a Hahn echo measurement is shown in Fig 1.13b. The signal de-

cays with the transverse relaxation time T_2, which is caused by fluctuations of the magnetic field with frequencies faster than the period of the Hahn echo sequence. The T_2 time is typically much longer than the T_2^* time observed in FID, due to the effective decoupling by the Hahn echo sequence. Furthermore, the signal shows periodic collapses and revivals. These are caused by the Larmor precession of the surrounding ^{13}C spin bath. For certain τ, the precession fits the filter frequency of the Hahn echo sequence, resulting in an increased phase accumulation.

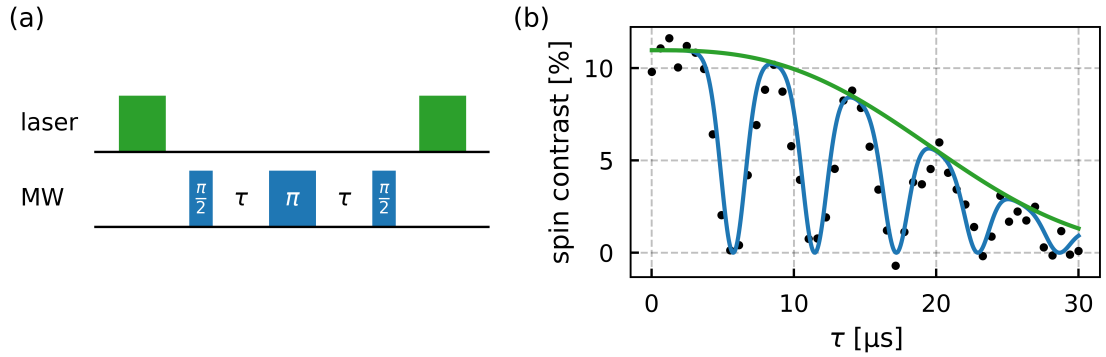

Figure 1.13: Signal **(b)** obtained using a Hahn echo sequence **(a)**. The signal shows a decay, described by the transverse relaxation time T_2. Additionally, collapses and revivals, caused by the Larmor precession of the surrounding ^{13}C spin bath, are observed.

1.5.7 Dynamical decoupling

The coherence time of the NV electron spin can be further enhanced by increasing the number of refocusing π-pulses. This improves the decoupling of the electron spin from its environment and reduces the width of the filter function. Based on this idea, several dynamical decoupling sequences were created. Prominent sequences are CPMG [77], UDD [78], KDD [79] and XY4 [80, 81]. In this thesis, the XY8-N sequence is used. The sequence is shown in Fig 1.14. The spin is periodically refocused by π-pulses. The total number of refocusing pulses is $8 \times N$, where N is the so-called order of the sequence. The relative phase of the MW switches between 0° and 90°. π-pulses with a relative phase

of 0° are denoted as π_x-pulses (blue in Fig 1.14) and results in a rotation of the spin state around the x-axis. With a relative phase of 90°, the pulse becomes a π_y-pulse (orange in Fig 1.14) and leads to a rotation around the y-axis. The use of rotations around different axis compensates dephasing for states along arbitrary direction, making the sequence more robust and efficient.

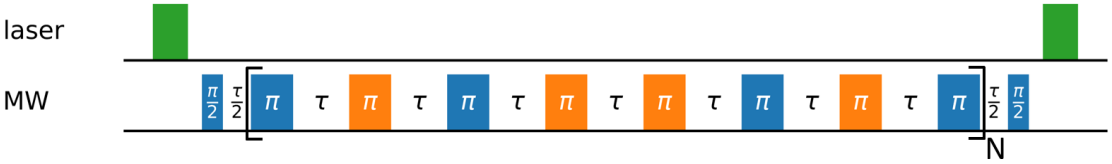

Figure 1.14: Depiction of the XY8-N dynamical decoupling sequence. The spin is periodically refocuses by π_x- (blue) and π_y-pulses (orange). The total number of π-pulses is $8 \times N$.

Chapter 2

2 Experimental setup

Contents

2.1 Introduction

A schematic of the experimental setup, used to perform the experiments in the following chapters, is depicted in Fig 2.1. A home-built confocal microscope allows to address single NV centers optically. The sample is optically accessed from below. A commercial AFM (Asylum Research, MFP-3D) is positioned above the sample. The AFM can be used for precise positioning and scanning of samples relative to the NV center, enabling imaging and scanning probe techniques using a NV center.

A permanent magnet, mounted on a motorized stage (Thorlabs MTS25/M-Z8E), is used to apply a bias magnetic fields to the NV center. A thin wire close to the NV center is used to generate MW fields for spin manipulation.

In the following sections, the main components of the setup are discussed in more detail.

2.2 Confocal microscope

The optical path of the confocal microscope is shown in Fig 2.1. Optical excitation is performed with green laser light at a wavelength of 520 nm. The laser light is generated by a home-built pulsed diode laser consisting of a commercially available drive module (PicoLAS, LDP-V 03-100 UF3) and a laser diode (Roithner, LD-520-50SG). A detailed description of the diode laser can be found in [63].

The green laser light is guided through a single mode fiber (SMF) to ensure a Gaussian beam profile. Afterwards, the beam is deflected towards the sample stage via a long-pass dichroic beam splitter (DC 1). The laser beam is focused onto the sample via an oil objective (Olympus UPlanSApo 60x, NA = 1.35). The objective is mounted on a XYZ piezo stage (Physik Instrumente) with a traveling range of 200 µm in x- and y-direction and 10 µm in z-direction. By scanning the objective, the laser focus is scanned across the sample and confocal images can be recorded.

The objective is collimating red fluorescence light, emitted by the NV center, onto the same optical path as the excitation laser beam. After passing the dichroic beam splitter (DC 1), the red light is focused onto the center of a 50

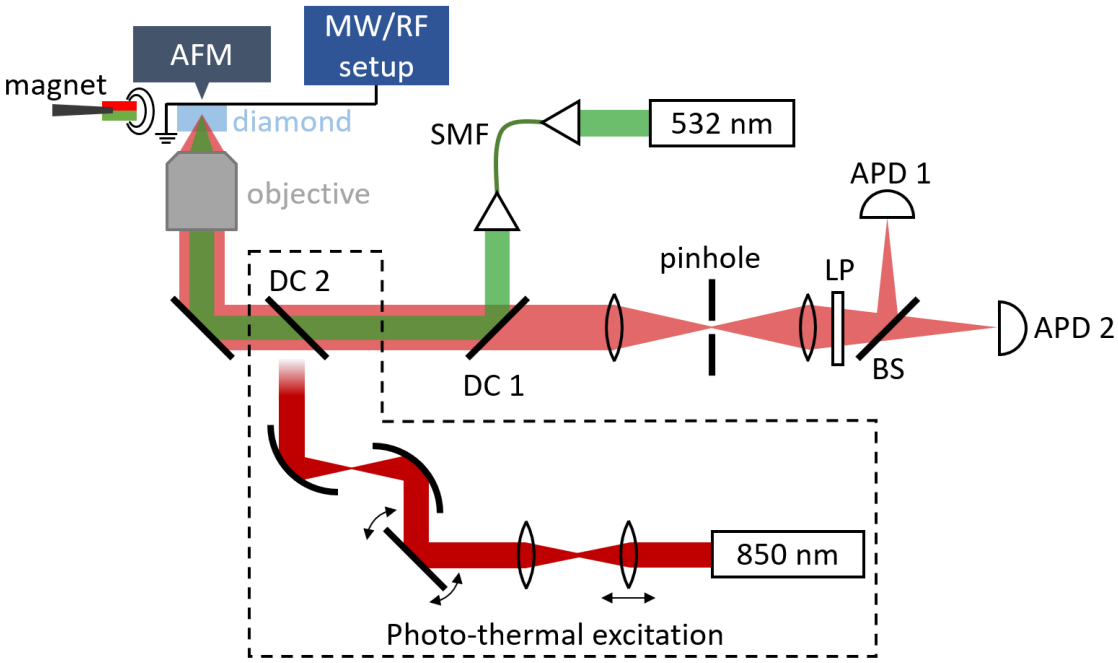

Figure 2.1: Illustration of the confocal microscope. The green laser light is focused onto the sample by an objective from the bottom side of the sample. The fluorescence is collected by the same objective and detected by two APDs in a Hanbury-Brown-Twiss setup. To record confocal images, the objective is scanned by a piezo-stage. The sample can be mechanically accessed from the top side with an AFM. The infrared laser, used for photo-thermal excitation of mechanical resonators, can be scanned via a galvo-scanner. The infrared light is coupled into the optical path of the green laser via a dichroic beam splitter (DC 2).

µm pinhole by a lens. A second lens is focusing the beam onto two APDs via a 50:50 beam splitter (BS). This is also known as a Hanbury-Brown-Twiss setup and allows to record auto-correlation functions of the detected photons. Residual laser light is filtered out by a 650 nm long-pass filter (LP).

The optical setup inside the dashed line is used for photo-thermal excitation of mechanical structures presented in Chapter 5. A near IR laser (850 nm) is deflected into the optical path of the green laser by a second dichroic beam splitter (DC 2) and focused onto the sample by the objective. The optical path is discussed in detail in Section 5.4.4.

2.3 MW and RF

The experiments presented in this thesis require sequences of pulses at different frequencies. Electron spins are manipulated by MW fields with frequencies between 1-6 GHz, while nuclear spins exhibit transition frequencies of a few MHz. The mechanical structures investigated in Chapter 5 require driving signals of ~1 MHz. The exact setup used to produce the necessary pulses depends on the specific experiment. The different setups are illustrated in Fig 2.2.

The generation of the MW signal used to manipulate the electron spin of the NV center is identical in each variation of the setup. A continuous MW signal is generated using a SMIQ06 signal generator (Rohde & Schwarz). An IQ mixer (Marki MLIQ-0218L) is used to modulate the signal via single sideband mixing. This way, the signal is pulsed and the frequency, phase and amplitude can be controlled. The I- and Q-input signals are generated by an arbitrary waveform generator (AWG) (Tektronix AWG520 or Spectrum DN2.663-04). A additional switch, also controlled by the AWG, is used to mitigate any power leakage between MW pulses. The signal is amplified by a Tecdia TD-A06M20-25-F amplifier.

The setup used for the quantum nuclear-assisted sensing introduced in Chapter 4 is depicted in Fig 2.2a. In this scenario, RF pulses with frequencies of a few MHz are required to manipulate the nitrogen nuclear spin of the NV center. The corresponding signal is produced by a SMIQ03 (Rohde & Schwarz) and pulsed using a switch (Mini-Circuits ZASWA-2-50DR+) controlled by the AWG. The signal is amplified by a Mini-Circuits LZY-22+ amplifier. The MW and RF

signal are then combined using a bias tee (Taylor Microwave BT-A1080-3). The RF signal is fed into the DC input of the bias tee which has a bandwidth of ~20 MHz.

The detection of external electron spins, presented in Chapter 3, requires active manipulation of the sensed electron spins at frequencies between 1-3 GHz. The used setup is shown in Fig 2.2b. As in the previous case, the signal is generated by a SMIQ03 and pulses are created using a switch. As the frequency is on the same order as the resonance frequency of the NV centers electron spin, both signals can be rooted through the same amplifier. For this purpose, both signals are first combined using a power combiner (Mini-Circuits ZX10R-14-S+).

The last setup variant (see Fig 2.2c) is used for experiments involving mechanical resonators as presented in Chapter 5. The used diamond cantilevers are either excited by a piezoelectric actuator, glued to the sample holder, or by periodic photo-thermal heating using an IR laser. The control signals of the actuator and the IR laser are both directly generated by the AWG. This allows to phase-lock and synchronize the drive signal of the mechanical structures to the MW pulses used for spin manipulation.

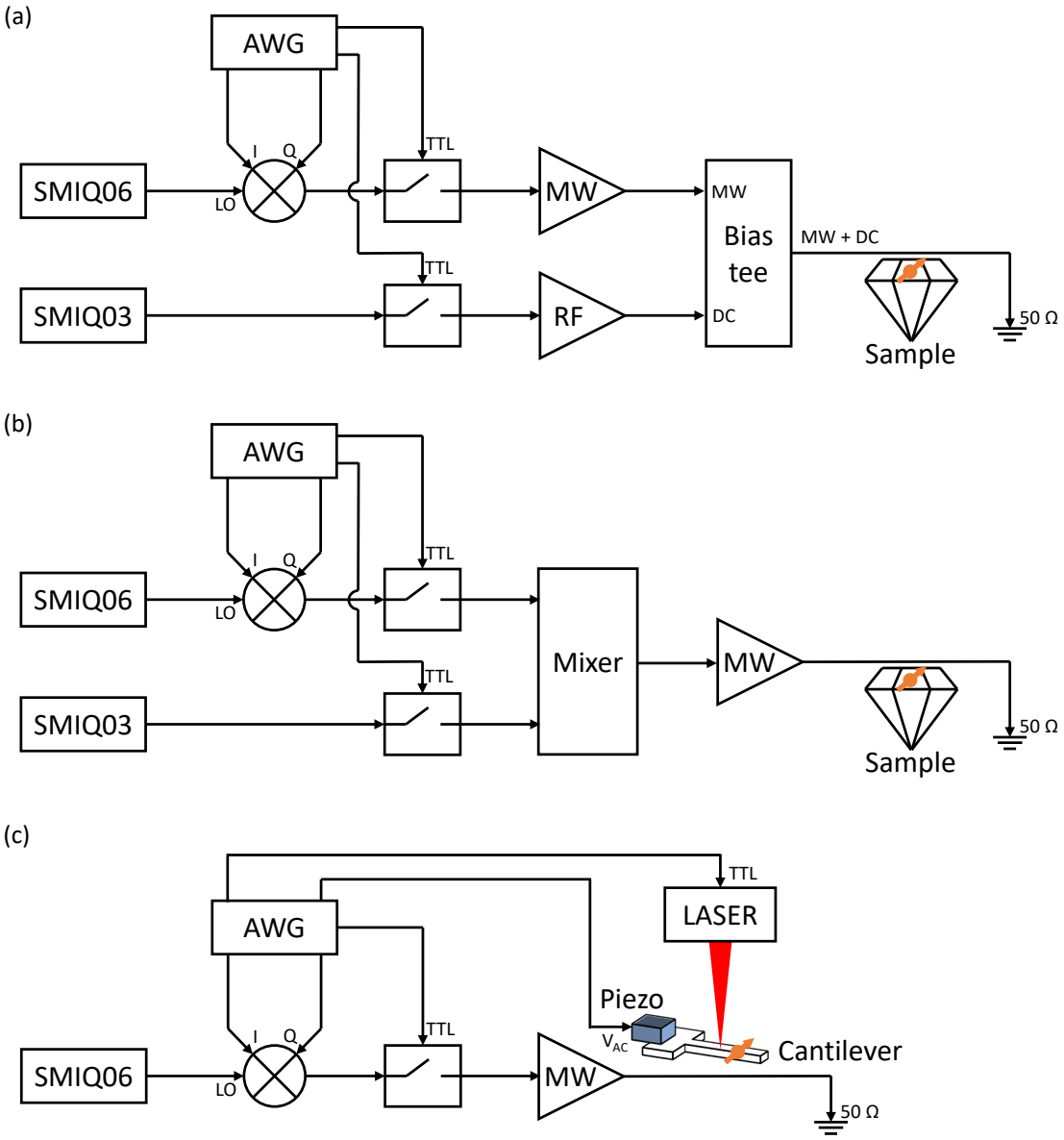

Figure 2.2: Setups to generate MW and RF pulses used for spin manipulation and drive signals used to excite mechanical resonators. The different variants are used for **(a)** quantum nuclear-assisted sensing, **(b)** sensing of external electron spin and **(c)** coupling of NV spins to mechanical resonators.

Chapter 3

3 Nanoscale ESR spectroscopy of spin labels

Contents

3.1 Introduction

Structural analysis of biomolecules is a key step in understanding their functionality. The interactions of proteins within biological systems and the associated processes are determined by their spatial conformation. Due to their complexity, it is difficult to deduce their folded shape from the chemical structure. Consequently, methods to gain information on the native three-dimensional structure of proteins are of great interest. Examples of techniques commonly used for this purpose are X-ray crystallography [82, 83], cryo electron microscopy and NMR spectroscopy [84]. If successful, these methods can yield the complete three-dimensional structure of studied proteins. However, they also suffer from high requirements in sample preparation and data analysis, rendering the analysis of certain protein species impossible.

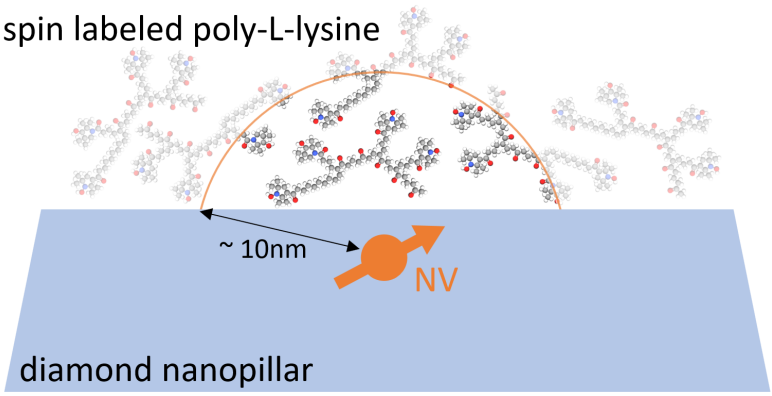

Figure 3.1: Illustration of the sample geometry to detect external spin labels. The spin-labeled poly-L-lysine is applied to the diamond surface. A shallow NV center, created via ion-implantation, is used to detect the spin labels via DEER spectroscopy.

An alternative technique is electron spin resonance (ESR) spectroscopy. Here, so-called spin labels, each hosting an electron spin, are attached to specific chemical sites in the target molecule. This process is known as site-directed spin labeling (SDSL). By exploiting the coupling between nearby spin labels, their distance from each other can be determined with nanometer-scale precision [11]. This way they can be utilized as nanoscale rulers to gain structural information about the target molecule. Additionally, analysis of their spectra can

give insights into the local environment. Conventional ESR measurements require averaging over a high number of spins (>1000) and are limited to macroscopic sample volume (~μm^3). As a result, it is difficult to gain information about different structural configurations in inhomogeneous samples. This limitation can be circumvented by using the NV center as a nanoscale ESR sensor.

In this chapter, the detection of spin labels via NV-based ESR spectroscopy is demonstrated. Due to the high sensitivity and small size of the NV center, this approach can be used to investigate single molecules. Furthermore, scanning probe microscopy (SPM) techniques can be implemented to image spin labels with nanometer precision [13].

3.2 Sample preparation

3.2.1 Spin labeling of poly-L-lysine

The amino acid polymer poly-L-lysine (PLL) is used as a model system. The used PLL (P7890, Sigma Aldrich) has a molecular weight of 15.000 - 30.000 amu. The lysines are spin-labeled using a NHS ester of the nitroxide spin label (NSL) (16148, Cayman Chemicals). The chemical structure of the PLL, the NSL and the spin-labeled PLL are depicted in Fig 3.2.

4.6 mg of PLL were dissolved in 460 µl phosphate-buffered saline (PBS). Subsequently, this PPL stock solution was diluted with PBS to a concentration of 1 mg/ml. The NSL NHS ester was dissolved in DMSO with a concentration of 10 µg/µl. A mixture of 60 µl PPL solution, 78 µl PBS and 78 µl NSL NHS ester solution was prepared. The quantities were chosen to label ~60% of the lysines. The mixture was incubated at room temperature for 1 h under rotation and subsequently for several hours at 7°C. To remove residual by-products of the labeling process, the solution was dialyzed using ZelluTrans Mini-Dialyzer membranes (MWCO 6000-8000, Carl Roth). In a last step, the solution was dialyzed against water to remove residual salts.

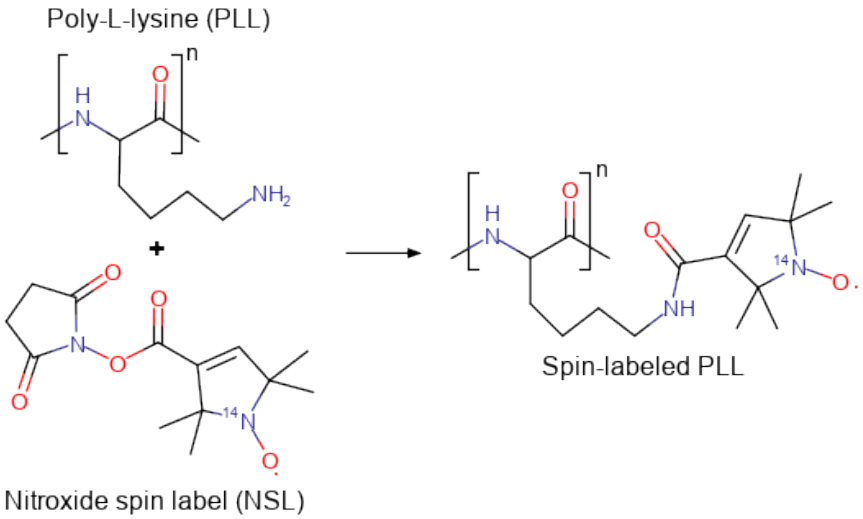

Figure 3.2: Spin-labeling of poly-L-lysine (PLL) with nitroxide spin labels (NSL). NSLs are bound to the lysines via a NHS ester group.

3.2.2 Preparation of the diamond sample

Shallow NV centers inside an electronic grade diamond with a thickness of ~30 µm were used for the experiments presented in this chapter. The NV centers were created by nitrogen implantation with an energy of 5 keV. The low implantation energy results in an average NV depth of ~8 nm [85]. After the NV center creation, nanopillars were etched out of the diamond surface. These nanostructures act as photon waveguides, enhancing the photon collection efficiency of embedded NV centers [86]. ~30% of the nanopillars were found to contain a single NV center and could thus be used in the following experiments.

In a first step, the diamond was cleaned for four hours in a mixture of equal proportions of sulforic acid (H_2SO_4), nitric acid (HNO_3) and perchloric acid ($HClO_4$) at a temperature of ~100°C. Subsequently, the spin-labeled PPL was applied to the diamond surface by drop-casting of 5 µl of the PLL solution. Fig 3.3a shows the topography of a single PLL-coated nanopillar recorded using an AFM. The PLL forms a uniform layer with a roughness of ~0.5 nm on the pillar surface (see Fig 3.3c). To determine the layer thickness, parts of the PLL layer were scratched off using an AFM. The respective areas are indicated by

black squares in Fig 3.3b. From the depth of the resulting hole in the PLL layer, a layer thickness of ~6 nm was deduced (see Fig 3.3d).

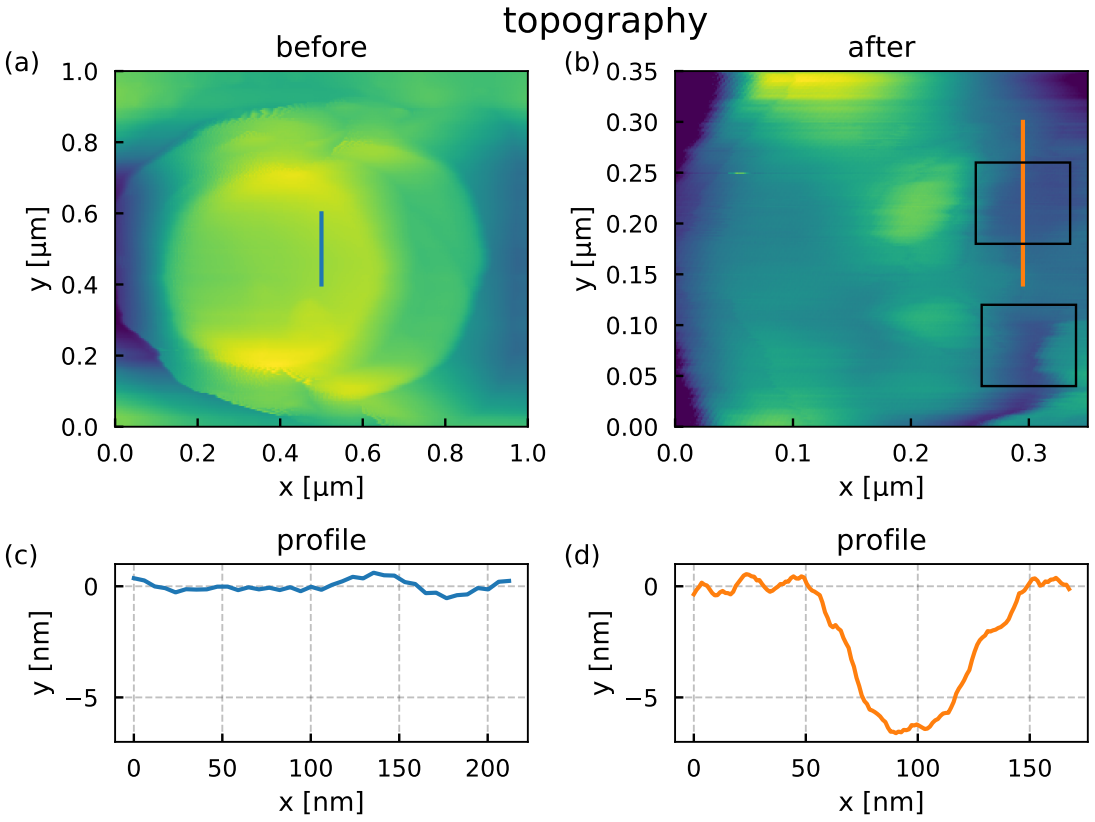

Figure 3.3: **(a)** Topography of a diamond nanopillar covered by a layer of spin-labeled PLL. A profile of the topography along the blue line is shown in (c). **(b)** Topography of the nanopillar surface after removing parts of the PLL layer (black squares) with an AFM. **(d)** Profile of a hole created in the PLL layer (along orange line in (b)). From the observed depth a layer thickness of ~6 nm is determined.

3.3 Nanoscale ESR

3.3.1 Double electron-electron resonance with NV centers

Double electron-electron resonance (DEER) was first introduced as a technique in ESR experiments. It is used to measure couplings between electron spins [10]. The observed coupling strength allows to determine inter-spin distances with high precision. This makes the technique a powerful tool for structural analysis of biological samples. DEER sequences are based on the decoupling sequences introduced in Section 1.5.6 and Section 1.5.7. Periodic π-pulses performed on a first electron spin (sensor spin) effectively decouple the spin from off-resonant magnetic fields, while increasing the phase accumulation caused by resonant magnetic fields. As the decoupling frequency of these sequences is limited to few MHz, the Larmor precession of electron spins (~GHz) can not be detected directly. To circumvent this limitation, the second electron spin (target spin) is actively manipulated by a second MW signal to invert its direction in sync with the sensor spin. This effectively modulates the magnetic field of the target spin into an AC magnetic field tuned into the filter function of the decoupling sequence. By varying the MW frequency, spectroscopy on the target spin can be performed.

The sequence used in this work to perform NV center-based DEER spectroscopy is depicted in Fig 3.4. The electron spin of the NV center is manipulated by a MW sequence at its resonance frequency denoted as ω_{NV}. The sequence is identical to the XY8 sequence introduced in Section 1.5.6. The target spins are manipulated by MW π-pulses with frequency ω_{SL}. Due to the ZFS of NV centers, the MW frequencies are well separated ($\omega_{\mathrm{SL}} \neq \omega_{\mathrm{NV}}$). This allows independent control of the two electron spin species. B_{SL} indicates the evolution of the magnetic field produced by the target spins during the sequence. Due to the periodic inversion of the target spins, an effective AC magnetic field at the position of the NV center is created. As the AC magnetic field is frequency-locked to the XY8 sequence, the NV center electron spin accumulates a phase due to the coupling to the target spins. This phase is subsequently mapped into the NV centers spin polarization and read out optically.

A prerequisite for this technique is that the timescale of random spin flips of

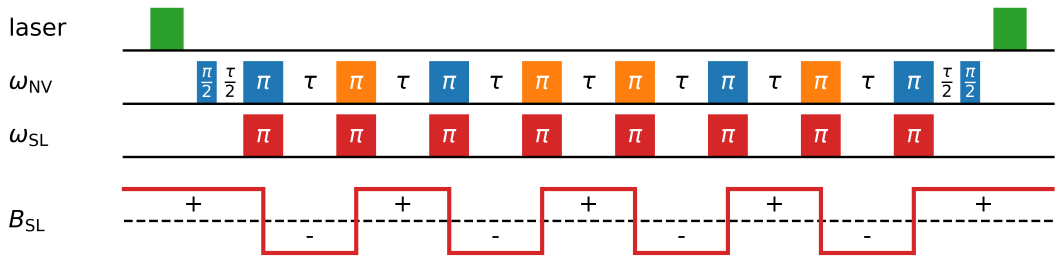

Figure 3.4: DEER sequence used to detect the coupling of a NV center to spin labels. A XY8 decoupling sequence is performed on the electron spin of the NV center with a resonant MW at frequency ω_{NV}. Blue/orange pulses represent π_x-/π_y-pulses (see Section 1.5.7). The electron spins of the spin labels are flipped in sync with the NV center spin by resonant π-pulses performed on a second MW channel at frequency ω_{SL}. B_{SL} represents the evolution of the magnetic field produced by the spin labels during the DEER sequence. Due to the periodic flipping, an effective AC magnetic field is created, which is locked into the frequency of the XY8 sequence. Consequently, the coupling to the spin labels is detected as a phase accumulation on the NV centers electron spin.

the target spins is longer than the sequence duration. Hence, the longitudinal relaxation time T_1^{SL} of the target spins should exceed the total measurement time ($2\tau < T_1^{\mathrm{SL}}$). To fulfill this condition, the target spin needs to be sufficiently well isolated from their environment. This prevents the detection of strongly coupled electron spin baths. NV center-based DEER spectroscopy was successfully used to detect nitrogen defects in the diamond lattice [87], electron spins embedded in external molecules [88], spin labeled proteins [89] and NV centers [90].

3.3.2 Numerical simulation

The used NSLs have an electron spin of $\frac{1}{2}$ and a nuclear spin of 1 from the embedded ^{14}N. The system is described by the Hamiltonian

$$H_{\mathrm{SL}} = \gamma_{\mathrm{el}} B_z \sigma_z + \underline{\sigma} \cdot \underline{\underline{A}} \cdot \underline{I}, \tag{3.1}$$

where $\underline{\underline{A}}$ is the hyperfine tensor and θ is the angle between the NSL's z-axis and the bias magnetic field $\underline{B} = (B_x, B_y, B_z)^T$ (see Fig 3.5a). In the following, it is assumed that the bias magnetic field is aligned along the NV center axis. In this case, θ matches the angle between the principle axis of the spin label and the NV center. In the coordinate system of the NSL, the hyperfine tensor has the diagonal form

$$\underline{\underline{A}} = \begin{pmatrix} A_{\mathrm{xx}} & 0 & 0 \\ 0 & A_{\mathrm{yy}} & 0 \\ 0 & 0 & A_{\mathrm{zz}} \end{pmatrix} \tag{3.2}$$

with $A_{\mathrm{xx}} = A_{\mathrm{yy}} = 14$ MHz and $A_{\mathrm{zz}} = 103.2$ MHz. The hyperfine tensor in the principle frame of the NV center is obtained by a unitary rotation as $\underline{\underline{A}}(\theta) = \underline{\underline{R}}(\theta) \cdot \underline{\underline{A}} \cdot \underline{\underline{R}}^{-1}(\theta)$, where $\underline{\underline{R}}(\theta)$ is the rotation matrix. By inserting $\underline{\underline{A}}(\theta)$ into Eq. (3.1) and subsequent numerical calculation of the energy eigenstates, the transition frequencies of the NSL can be obtained. Fig 3.5b shows the calculated values of the transition frequencies for all three nuclear spin states. In this graph, the central frequency (0 MHz) is the resonance frequency of a free electron ($g = 2.002$). The hyperfine splitting depends on the tilt angle θ and can have any value between A_{xx} and A_{zz}.

In the following, a simulation of the DEER signal of a NSL, observed via a NV center, is discussed. Using the rotating wave approximation (introduced

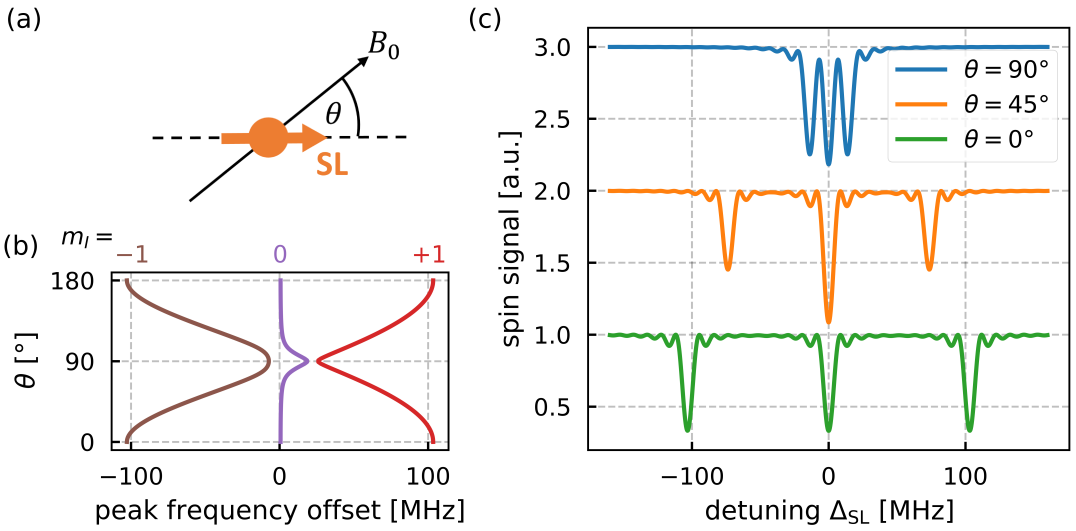

Figure 3.5: **(a)** Definition of the angle θ between the SL axis and the static magnetic field B_0 aligned along the NV axis. **(b)** Calculated transition frequencies of the hyperfine structure for different angles θ. An offset frequency of 0 MHz corresponds to the frequency of a free electron ($g = 2.002$). **(c)** Simulated results of a DEER measurement in presence of a NSL for different tilt angles θ. The hyperfine spectrum of the NSL is observed in the DEER measurement.

in Section 1.4.2) for both electron spins (NV and NSL), the Hamiltonian of the NV-NSL system becomes

$$H = \underbrace{\Delta_{\mathrm{NV}}\hat{S}_z + \Omega_{\mathrm{NV}}\hat{S}_x}_{\text{NV center}} + \underbrace{\Delta_{\mathrm{SL}}\hat{\sigma}_z + \Omega_{\mathrm{SL}}\hat{\sigma}_x}_{\text{spin label}} + \underbrace{(A_{\mathrm{xx}} - A_{\mathrm{zz}})\sin\theta\cos\theta\hat{\sigma}_z\hat{I}_y + (A_{\mathrm{xx}}\sin^2\theta + A_{\mathrm{zz}}\cos^2\theta)\hat{\sigma}_z\hat{I}_z}_{\text{dipolar coupling}} \tag{3.3}$$

Here, all $\hat{S}_x$ and $\hat{S}_y$ terms are neglected, as the Zeeman term is much larger than the hyperfine couplings. By simulating the evolution of the spin states during the DEER sequence, the resulting spectrum of the NSL can be simulated. Simulated DEER spectra for different tilt angles are shown in Fig 3.5c. The hyperfine structure of the NSL is imprinted into the electron spin polarization of the NV center.

3.3.3 Nanoscale ESR of nitroxide spin labels

NV-based DEER spectroscopy under ambient conditions was performed after three different preparations of the diamond surface. DEER signals were recorded after acid cleaning of the diamond, after applying a layer of unlabeled PLL and after applying a layer of spin labeled PLL (see Section 3.2.2 for details). For each case, DEER spectra from 10 individual NV centers were obtained. The three spectra measured on one of the NV centers are depicted in Fig 3.6. The observed spectra can be divided into three categories. When the surface was clean or coated with unlabeled PLL, 95% of measurements did not show a signal. In the rest of the measurements (5%) a single peak at a frequency of $\omega_{0,\mathrm{SL}} = \gamma_{\mathrm{el}}B_0$ and a spin contrast between 1-10% is observed. These signals could stem from dangling bonds on the diamond surface, randomly created during sample preparation [55, 91]. When the surface is coated with spin-labeled PLL, all recorded DEER spectra show a distinct peak at frequency $\omega_{0,\mathrm{SL}} = \gamma_{\mathrm{el}}B_0$. Most measurements (80%) in addition show two side peaks. The peak spacings are within the possible values of the NSL hyperfine spectrum. When the static magnetic field is changed, the central frequency of the DEER spectrum is shifted according to a g-factor of $g = 2.006 \pm 0.024$ (see Fig 3.6b). Within the error, the measured

value fits the electron spin g-factor $g_e = 2.002$. The maximum signal strengths $S_{\max}$ of the individual measurements are plotted in Fig 3.6c. The average signal strength with the spin labeled PLL coating is $\bar{S}_{\max} = 15.9\%$. Without NSLs on the diamond surface, the average signal strength is only $\bar{S}_{\max} = 1.3\%$. The overall stronger DEER signals in presence of spin labeled PLL and the observed side peaks prove that the observed signals are linked to the NSLs.

Fig 3.7 shows examples of DEER spectra recorded in the presence of spin labeled PLL. All observed spectra are symmetric and exhibit frequency splittings between 30 - 50 MHz. The lower spin contrast of the side peaks indicates that the signal stems from multiple NSLs with different orientations. This fits well to the expected spin density of ~1 spin/nm^3 resulting from the sample preparation protocol. At least >50 electron spins are assumed to contribute to the observed spectra.

By fixing the MW frequency ω_{SL} to one of the NSL resonance frequencies and varying the duration of the MW pulses t_{SL}, Rabi oscillations of the NSL spins can be observed. Rabi oscillations (introduced in Section 1.4.2) recorded with MW pulses resonant to the right peak (orange) and the central peak (blue) are shown in Fig 3.8b. Hence, coherent control of the external electron spins is possible.

During measurements, a decay of the DEER signal strength over time was observed. Signals typically vanished after few hours of experimentation under ambient conditions. The spin labels are found to be stable prior to the experiments, indicating that the conditions during the DEER spectroscopy are causing the observed decay. A likely scenario is that a photochemical modification of the spin labels is induced by the laser light used to read out and polarize the NV center. This process, known as photobleaching, is a common phenomenon observed in fluorescence microscopy [92]. An important milestone of the nanoscale ESR technique is the detection of single or few spin labels. To achieve this goal, the DEER spectroscopy was repeated with a PLL sample with a spin labeling percentage of ~1%.[1] In these experiments no DEER signals were detected, which we attribute to fast photobleaching of the few spin labels inside the detection volumes of the NV centers.

Follow-up measurements, performed by Schlipf et al., at low temperature

[1] The previous results were conducted with ~60% of lysines being spin labeled.

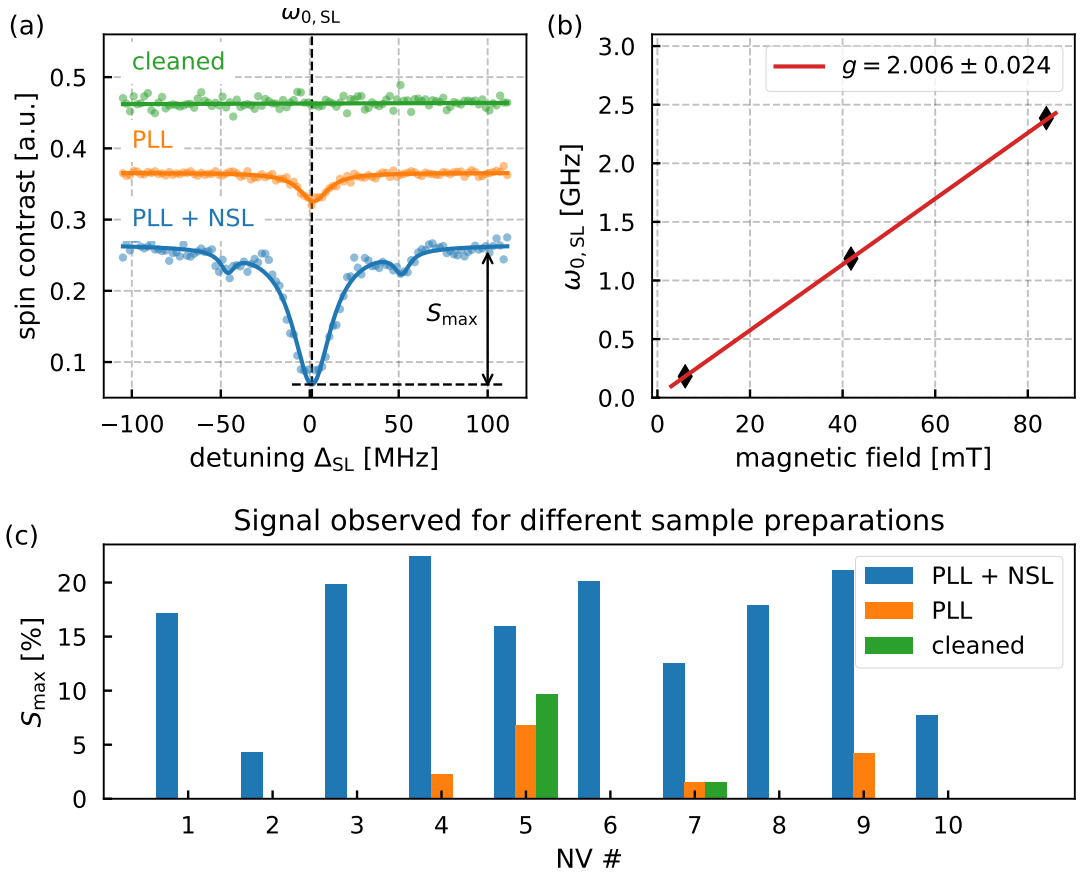

Figure 3.6: NV-based DEER spectroscopy for three different preparations of the diamond surface - acid cleaned surface, coated with unlabeled poly-L-lysine (PLL) and coated with spin labeled poly-L-lysine (PLL + NSL). **(a)** DEER spectra recorded with one NV center for the three different sample preparations. With a cleaned surface no signal is observed. When coated with unlabeled PLL a single peak, presumably associated to a surface dangling bond, is detected. After applying spin labeled PLL, three peaks are observed, resembling the hyperfine spectra of the NSL. **(b)** When the bias magnetic field strength is changed, the central frequency of the spectra is shifted in accordance with a g-factor of $g = 2.006 \pm 0.024$. This indicates that the signal stems from an electron spin. **(c)** Maximum spin contrast S_{max} of each recorded spectra (10 NV centers).

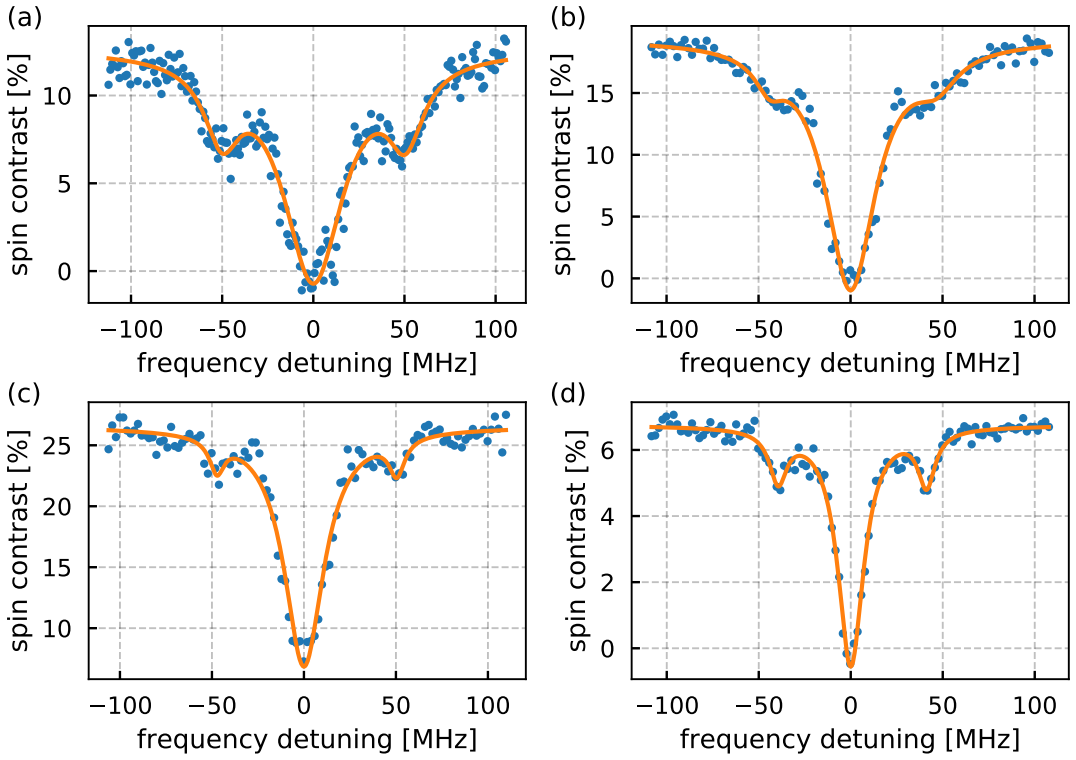

Figure 3.7: DEER spectra of nitroxide spin labels measured via four different NV centers. All spectra show three peaks with equidistant spacing, reflecting the hyperfine structure of the nitroxide spin labels. The lower spin contrast of the side-peaks indicates that the signal originates from a cluster of spin labels with varying orientations.

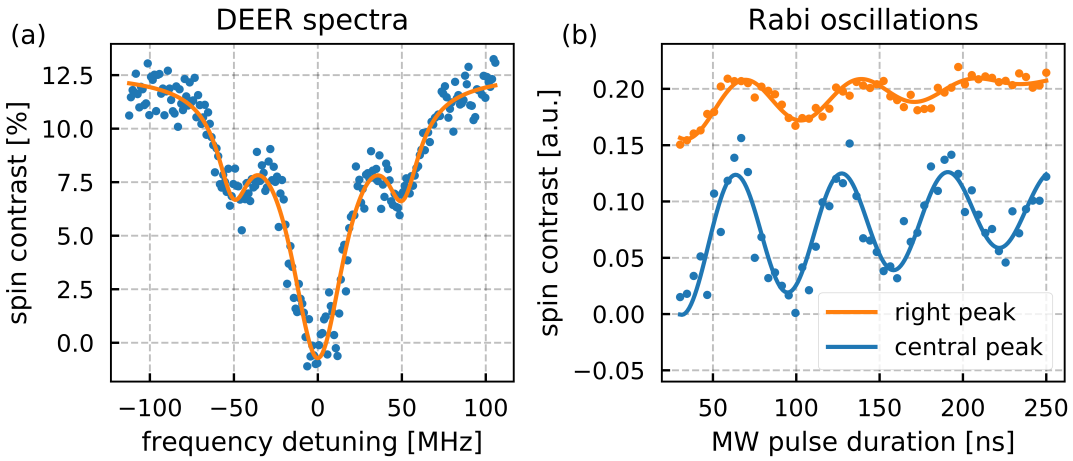

Figure 3.8: **(a)** DEER spectra of spin labels. **(b)** Rabi oscillations of spin labels driven with a MW resonant to the right peak (orange) or central peak (blue).

and under ultra-high vacuum demonstrate the observation of few NSLs (<6) attached to peptides [12]. Under these conditions, the NSLs were found to be stable over several weeks of experimentation. Furthermore, coherent coupling between spin labels was observed and allowed to measure spin-spin distances. This opens the opportunity for novel applications. As proposed by Schlipf et al., properly designed molecules can be used as a framework to host an array of electron spins with distances of few nanometers. Such a system can be used as quantum network, where the spins are directly coupled by their magnetic dipole interaction. In this scenario, the NV center acts as an access point to the spin network.

3.4 Summary and outlook

In this chapter, the detection of spin labels via NV-based nanoscale ESR was presented. For this purpose, the diamond surface was coated with spin labeled PLL and DEER spectroscopy was performed with 10 individual NV centers. In presence of the spin labeled PLL, all NV centers showed distinct DEER spectra with an average spin contrast of 15.9%. In most of the spectra (80%), two sym-

metric side-peaks were observed. These spectra fit well to the expected signal caused by NSLs. Reference measurements with a cleaned diamond surface and a coating of unlabeled PLL showed a strong decrease of the average spin contrast to 1.3%, where 95% of DEER measurements did not show a signal at all. This verifies that the previously observed signal stemmed from the NSLs.

The NSLs were found to decay during the experiments under ambient conditions. This is attributed to photochemical modifications of the spin label molecules induced by the laser pulses used to read out the NV center. As demonstrated by Schlipf et al., NSLs become stable for several weeks at low temperature and under ultra-high vacuum [12]. This stability allowed the detection of signals from a small number of spin labels (<6) and the measurement of spin-spin distances.

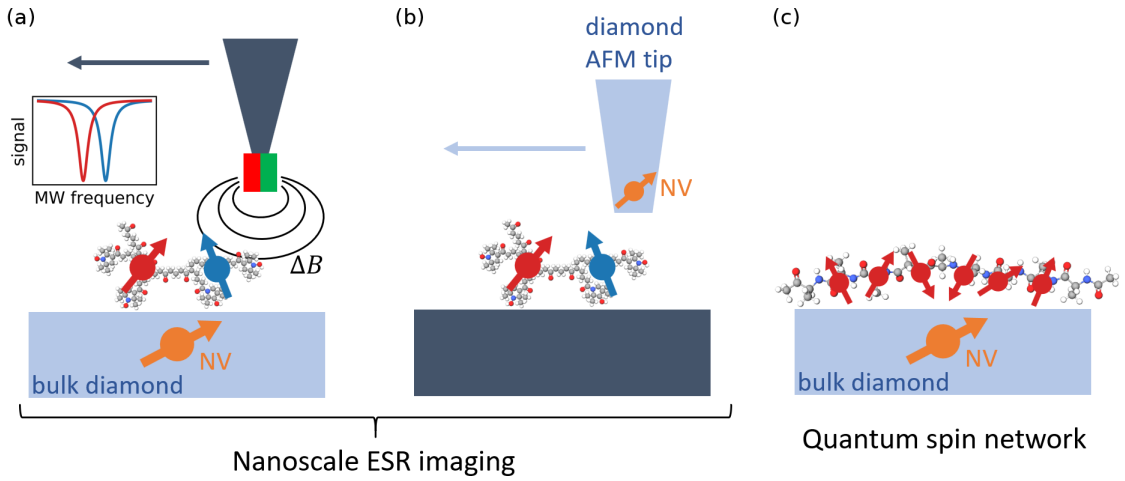

Figure 3.9: Potential applications of NV-based nanoscale ESR. **(a)** Spin label localization using a high-magnetic field gradient produced by a magnetized AFM tip. **(b)** Spin label imaging by scanning a NV center inside of a diamond AFM tip over the sample. **(c)** Spin register created by site-directed spin labeling of a polymer. In this scenario, the NV center acts as an access point to the spin network.

Utilizing SPM techniques, the NV-based nanoscale ESR could be expanded into an imaging technique. Two possible setup geometries are shown in Fig 3.9a,b. A small magnetic AFM tip can be used to apply a strong magnetic field gradient in the sample volume (see Fig 3.9a). This way individual spin labels can

be spectrally resolved and three dimensional localization of the spin labels with subnanometer precision is feasible [13]. Alternatively, a diamond AFM tip [14, 15, 16, 17, 18, 19], containing a single NV center, can be scanned over the sample to allow ESR imaging of a larger sample area with nanometer resolution (see Fig 3.9b).

Another possible application is to use the precise positioning, offered by SDSL, to create quantum networks composed of dipolarly coupled electron spins (see Fig 3.9c), as proposed by Schlipf et al. [12]. Here, the positions of individual spin labels can be controlled via the chemical structure of the host molecule. Placing the spin labels with distances of few nanometer, the electron spins are coupled directly by their magnetic dipole interaction. In this scenario, the NV center acts as an access point to the electron spin network.

Chapter 4

4 Nuclear Quantum-assisted sensing

Contents

4.1 Introduction

The performance of the NV center as a quantum sensor depends strongly on the efficiency of the optical spin readout. Especially for the NV-based imaging techniques, discussed in Section 3.4, a fast measurement time is important to achieve reasonable scanning speeds and number of pixels. The signal-to-noise ratio (SNR) of the optical readout is the ratio between the number of photons N_S contributing to the signal and the photon noise ΔN. The readout is mainly limited by the photon shot noise $\Delta N = \sqrt{N}$, where N is the total number of collected photons [93, 8]. The SNR is then

$$\mathrm{SNR} = \frac{N_S}{\sqrt{N}} = \frac{cN}{\sqrt{N}} = c\sqrt{N}, \tag{4.1}$$

where c is the fluorescence contrast between the two spin states. In a pulsed experiment (see Section 1.5.1), the number of photons, collected after a certain measurement runtime T_{run}, depends on the time T between consecutive spin readouts and the number of photons n collected per readout. The time-dependent SNR of a shot-noise limited pulsed experiment can be written as

$$\mathrm{SNR}(t) = c\sqrt{\frac{n}{T}T_{\mathrm{run}}}. \tag{4.2}$$

Hence, to optimize the performance of NV-based sensing, the average photon count rate n/T needs to be maximized. T is defined by the duration of the sensing pulse sequence T_{sens} and the duration of the optical readout T_{read} as

$$T = T_{\mathrm{sens}} + T_{\mathrm{read}}. \tag{4.3}$$

The best strategy to maximize n/T depends on the duration of the sensing sequence. For increasing T_{sens}, the number of photons per readout becomes more important as $n/T \approx n/T_{\mathrm{sens}}$ for $T_{\mathrm{sens}} \gg T_{\mathrm{read}}$, while the duration of the readout becomes neglectable. To highlight this behavior, Eq. (4.2) is plotted for two different sets of parameter values in Fig 4.1.[1] Set 1 (blue) has a longer readout time ($T^{(1)}_{\mathrm{read}} = 10$ ms) and a lower photon count rate during the readout

[1] The same measurement time t and fluorescence contrast c is used for both parameter value sets. As the shown SNR is normalized, the values of both parameters do not change the result.

$((n/T_{\text{read}})^{(1)} = 10^4\ \text{s}^{-1})$. However, in total, the number of photons per readout is higher. Set 2 (orange) has a shorter readout time ($T_{\text{read}}^{(2)} = 10^{-3}$ ms) with a higher count rate ($(n/T_{\text{read}})^{(2)} = 10^6\ \text{s}^{-1}$). For short T_{sens}, set 2 results in a higher SNR as the photon count rate is the limiting factor. However, for increasing T_{sens}, set 1 offers a higher SNR as the total time per measurement cycle T is primarily defined by T_{sens}. This shows that there is no ultimate route to optimize the performance of a NV-based sensing applications and a thorough analysis of the requirements and capabilities of the system is necessary.

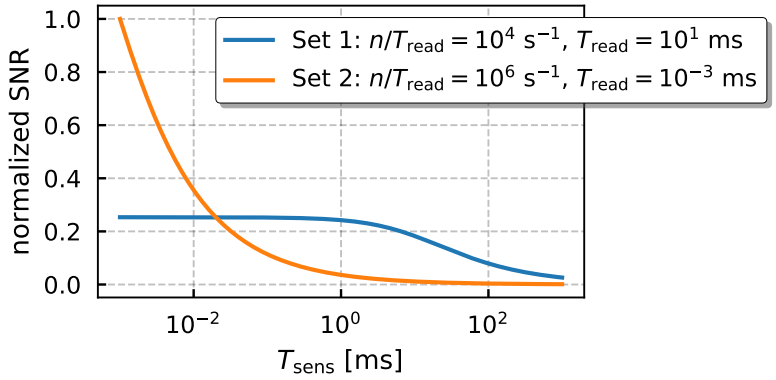

Figure 4.1: Normalized signal-to-noise ratio (SNR) of a pulsed NV-based sensing experiment over the duration of the sensing sequence. The SNR is plotted for two different parameters sets of the spin readout. The blue line represents the SNR achieved with a slow readout that yields a high number of detected photons per readout. In contrast, the orange line shows the SNR with a fast readout that results in a smaller number of detected photons per readout. For short sensing protocols, the faster readout results in a higher SNR. For long sensing sequences, the readout yielding more photons per readout leads to a higher SNR.

For long sensing protocols, a readout yielding a high number of photons per readout is preferable. Different methods to achieve such readouts were already demonstrated [94]. Prominent examples are resonant optical excitation [95], spin-to-charge conversion [96, 97, 98, 99] and the use of ancillae spins [20, 71, 100]. In this chapter, a single shot readout (SSR) sequence, based on a long living memory spin, is used. The SNR improvement achieved via a

SSR-based sensing sequence is discussed and experimentally demonstrated. A continuation of the work presented in this chapter, utilizing improved experimental conditions, was published by Häberle et al. [21].

4.2 Single Shot Readout

A long-living memory spin can be used to detect the NV center's electron spin state with fidelities close to unity [20]. This technique, called single-shot readout (SSR), consists of two steps. First, the electron spin state is mapped onto the memory spin. In the second step, the state of the memory spin is read out repetitively via a quantum non-demolition (QND) measurement. In the NV center's case, single nuclear spins in its vicinity can be used as a memory. A prime candidate is the intrinsic nitrogen nuclear spin. Alternatively, nearby ^{13}C spins can be utilized. The additional step of mapping the electron spin state into the nuclear spin state adds an overhead to the readout process, resulting in a significantly longer duration. At the same time, however, more information is extracted in a single readout process.

The main figure of merit of a SSR is the readout fidelity $\mathcal{F}$. It is commonly defined as the probability to measure the correct spin state. However, in this work, another definition is used. The fidelity is defined as the probability to detect the same spin state in two subsequent measurements.

4.2.1 Readout of the nuclear spin state

The nuclear spin state is read out by repetitively mapping it into the electron spin state, which is subsequently detected optically. This process is repeated M times during a single readout of the nuclear spin state. The pulse sequence of the readout protocol is depicted in Fig 4.2b. The mapping of the nuclear into the electron spin state is performed via a nuclear spin state selective π-pulse. Fig 4.2a shows a hyperfine-resolved ODMR measurement of the NV center's electron $m_s = -1$ spin state. The two offset frequencies $\omega_1/(2\pi) = -1.5$ MHz and $\omega_2/(2\pi) = +1.5$ MHz correspond to the resonances of the $m_I = +1/2$ and $m_I = -1/2$ spin states of the intrinsic nitrogen spin, respectively. From the central frequency $\omega_0/(2\pi) = 5.1$ GHz of the ODMR spectrum, a static magnetic field

along the NV axis of $B_{NV} = (\omega_0 + D_{ZFS})/\gamma_{NV} = 0.28$ T is deduced[2]. A π-pulse with frequency ω_1 acts as a controlled-NOT (CNOT) gate between the nuclear- and electron spin. In this case, the electron spin is flipped dependent on the nuclear spin state. Hence, we denote this gate as a C_nNOT_e-gate. To readout the electron spin state, a short laser pulse (≈ 300 ns) is used. The result of the readout is defined by the total number of photons detected during the readout sequence.

Fig 4.2c shows the number of collected photons n for subsequent readouts of the nuclear spin state (gray line). The photon trace shows distinct jumps between two levels of photon counts (red line), each corresponding to one of the two nuclear spin states. Hence, this measurement resembles a trace of the nuclear spin state. From the spin flip rate, a nuclear spin lifetime of $T_1^n \approx 10$ ms can be determined.

A histogram of the photon count signal, showing the two distinct photon count levels corresponding to the two spin states, is shown in Fig 4.2d. The overlap of the two fitted Lorentzian curves (orange and blue) can be used as a measure for the fidelity of the readout. However, in accordance with the definition of the fidelity introduced earlier in this chapter, the fidelity is determined by the probability of detecting the same spin state in two subsequent readouts in the nuclear spin trace. The result of an individual readout is determined by comparing the number of collected photons to a photon count threshold v_{th} indicated by a red line in Fig 4.2d.

The fidelity can be optimized by choosing the right number of repetitions M. Fig 4.2d shows the readout fidelity over M. The highest fidelity of $\mathcal{F} \approx 85\%$ is achieved at $M \approx 450$. For smaller M, less photons are collected, reducing the readout fidelity. For higher M on the other hand, although more photons are collected, the fidelity is decreasing because of the finite lifetime of the nuclear spin. In this case, the probability of a nuclear spin-flip during the readout is too high. To further increase the achievable readout fidelity, the photon count rate and the nuclear spin lifetime need to be maximized. In the experiments presented in this work, the photon count rate was improved by the use of pho-

[2] At the high magnetic field applied to the NV center, the Zeeman energy shift of the $m_s = -1$ spin state surpassed the zero field splitting. Hence, the total energy shift of the $m_s = -1$ state is $\Delta\omega = \omega_0 + D_{ZFS}$.

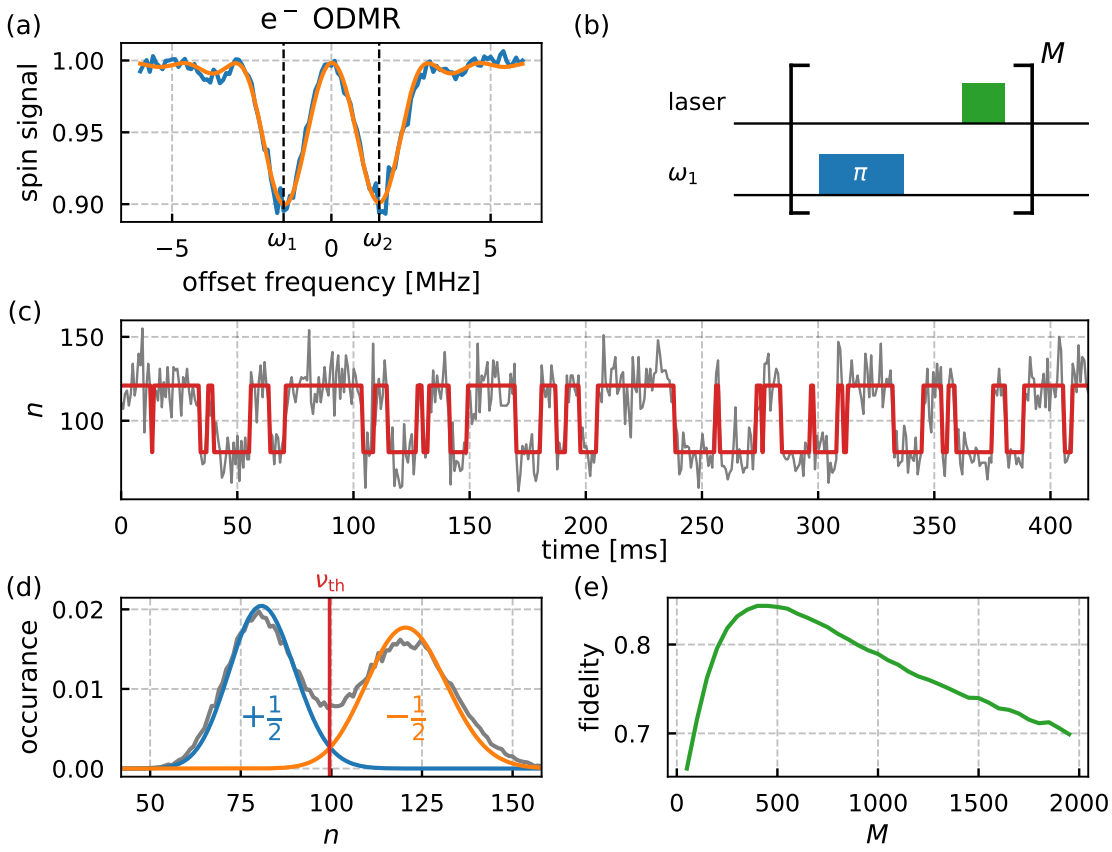

Figure 4.2: **(a)** Hyperfine-resolved ODMR of the $|m_s = 0\rangle \leftrightarrow |m_s = -1\rangle$ transition. ω_1 and ω_2 correspond to the $m_I = -1/2$ and $m_I = +1/2$ nuclear spin states, respectively. **(b)** Pulse sequence used to detect the nuclear spin state. The nuclear spin state is mapped into the electron spin state by a nuclear spin state-selective π-pulse (ω_1). Subsequently, the electron spin state is read out optically using a short (300 ns) laser pulse. This sequence is repeated M times. **(c)** Time trace of the signal generated using the sequence shown in (b). The number of collected photons per readout jumps between two distinct levels, corresponding to the two nuclear spin states. Hence, the measurement shows the time trace of the nuclear spin state. **(d)** Histogram of the time trace shown in (c). The two peaks show the two distinct photon count levels of the nuclear spin states. The result of the readout can be determined using the photon threshold n_{th}. **(e)** Fidelity of the single shot readout over the number of repetitions M. The optimal number of repetition depends on the nuclear spin lifetime.

tonic waveguides [86] and the nuclear spin lifetime was prolonged by strong magnetic bias fields aligned to the NV axis. These measures are discussed in more detail in the following subsection.

4.2.2 Experimental implementation

Bias magnetic field

As the magnetic field dependent nuclear spin lifetime is a key limiting factor of the readout fidelity, the bias magnetic field should be as strong as possible. At the same time, the experimental setup is supposed to be compatible with the atomic force microscope (Asylum Research, MFP-3D). This poses severe restriction on the design of the permanent magnets producing the magnetic bias field at the NV center's position. A sketch of the experimental setup is shown in Fig 4.3. While the sample is accessed optically via a high-NA oil objective positioned below the sample holder, the AFM enables mechanical access from the top side. As a result, only little space is available to position permanent magnets close to the sample.

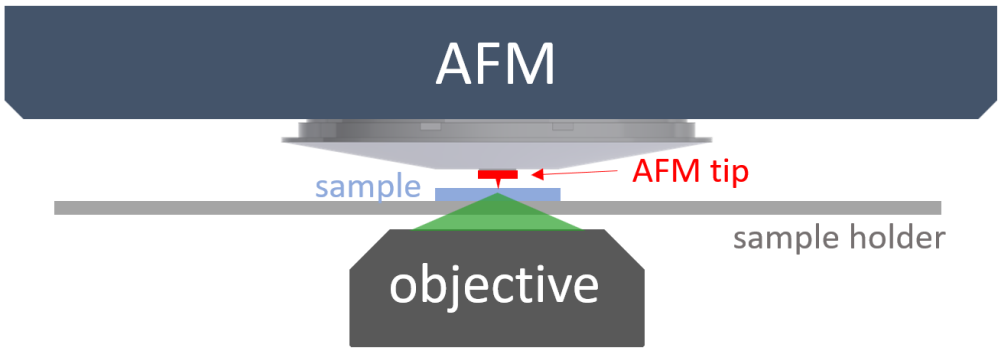

Figure 4.3: Illustration of the combined AFM-confocal microscope. The sample is accessed optically from below via a high-NA oil objective. Additionally, mechanical access is employed from the top side by an AFM. Positioning of permanent magnets close to the sample is difficult, as most space is occupied by the AFM. To solve this issue, a custom tip holder had to be fabricated.

To solve this issue, a custom tip holder was designed and 3D printed from

stainless steel. 3D models of the standard[3] and custom tip holder are depicted in Fig 4.4a and b respectively. From the side views of the models (lower), it can be seen that the custom holder creates space on both sides of the tip position and hence, allows positioning of permanent magnets much closer to the sample.

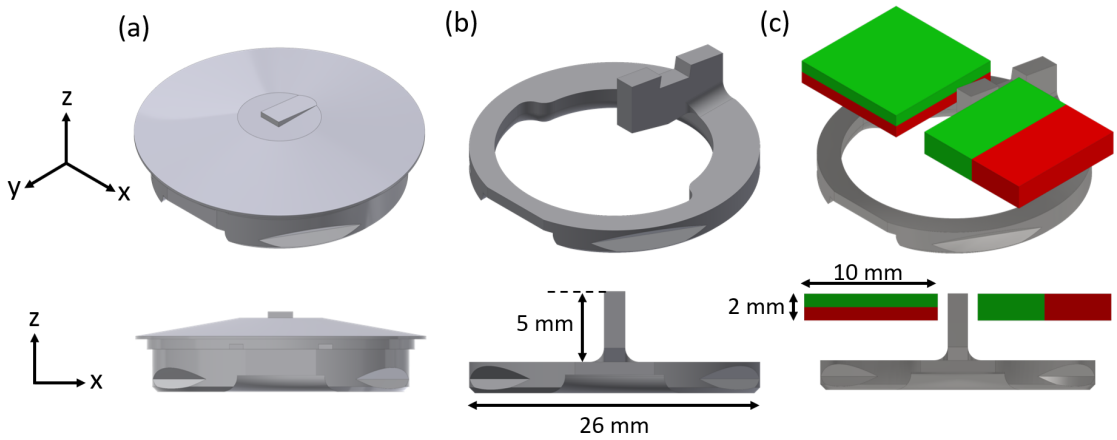

Figure 4.4: Different designs of the AFM tip holder. **(a)** Rough recreation of the standard tip holder offered by Asylum Research. The bulk of the holder is close to the sample surface, prohibiting positioning of permanent magnets close to the sample. **(b)** Custom tip holder designed to allow positioning of permanent magnets close to the sample. The holder used in the SSR experiments were 3D printed from stainless steel. **(c)** Custom tip holder and permanent magnets used in the experiments. The magnets are (10x10x2) mm in size and perpendicularly magnetized. The spacing between the magnets still allows mechanical access using the custom tip holder.

The used set of permanent magnets and their position relative to the tip holder are depicted in Fig 4.4c. The magnets are (10x10x2) mm in size and have perpendicular magnetization directions $\mathbf{e}_z$ and $-\mathbf{e}_x$. The magnets are attached to a custom made titanium holder, which can be positioned in x-, y- and z-direction by a motorized stage (Thorlabs MTS25/M-Z8E). The magnet

[3] An exact 3D model of the commercial tip holder was not available. The shown model is a rough, but sufficiently accurate, recreation of the real holder.

setup is designed to produce a strong magnetic field aligned to the NV orientation $\sphericalangle(\mathbf{e}_z, \mathbf{e}_{\mathrm{NV}}) = 0°$ in a (100)-diamond, positioned below the magnets. A FEM simulation of the magnetic field in the x-z-plane is shown in Fig 4.5a. The magnetic field is only plotted at positions where the alignment to the NV axis is above 99.7%. The trajectory of perfect alignment is roughly following the z-axis. Hence, a wide range of magnetic field strengths ($B_{\mathrm{NV}} = 50-400$ mT) can be applied to the NV center by varying the z-position of the magnets.

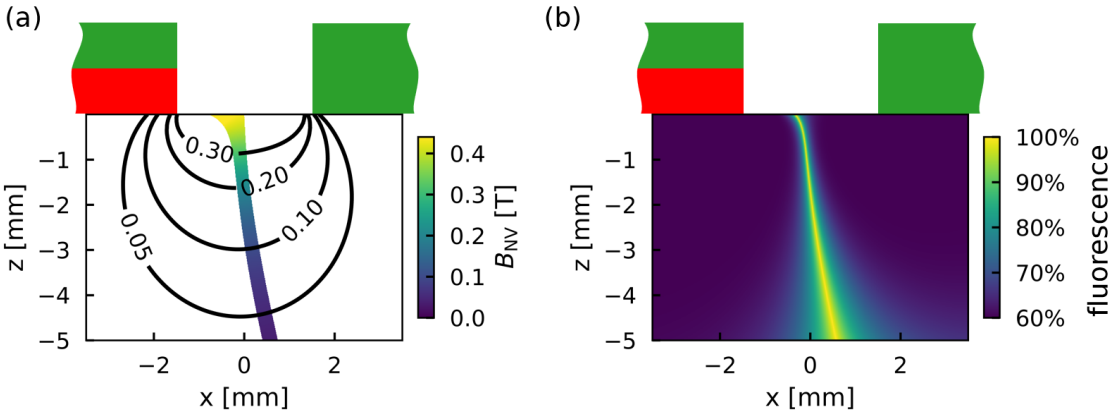

Figure 4.5: FEM simulation of the magnetic field generated by the two magnets. **(a)** The magnetic field is only shown for positions at which the alignment to the NV axis is over 99.7%. The trajectory of perfect alignment roughly follows the z-axis. This allows to control the magnetic field strength via the z-position of the magnets. Importantly, the magnetic field is alignment in the center of the gap between the magnets. Magnetic fields up to 300 mT can be applied to the NV center. **(b)** Calculated NV fluorescence based on the FEM simulation of the magnetic field. The fluorescence of the NV center is quenched by off-axis magnetic fields. Hence, the trajectory of perfect alignment is visible as a bright line. Closer to the magnets, the fluorescence distribution along the x-axis gets narrower, indicating that a more precise alignment of the magnetic field is required at a high magnetic field.

Off-axis magnetic fields quench the NV fluorescence due to mixing of the spin states. Hence, more precise alignment of the field is required, when the mag-

netic field strength is increased. The NV fluorescence, calculated from the FEM simulation results, is shown in Fig 4.5b. The line of bright fluorescence follows the trajectory of perfect alignment and gets narrower when approaching the magnets. This effect can be used as a tool for alignment of the magnetic field. Fig 4.6a shows the measured NV fluorescence while the permanent magnets are scanned in the x-y-plane. The high fluorescence indicates the area of good alignment. However, the alignment accuracy, using this technique, is found to be not sufficient. The nuclear spin lifetime is much more sensitive to off-axis fields than the fluorescence. Hence, in a second step, the SSR fidelity is measured while scanning the magnets in x-y-direction. The SSR fidelity gives a much narrower feature and enables alignment with high precision. A fidelity scan can be seen in Fig 4.6b. The scanned area is also indicated in Fig 4.6b by a red rectangle. The fidelity scan requires a refocus of the transition frequencies ω_1 and ω_2, via an ODMR measurement, at each pixel.

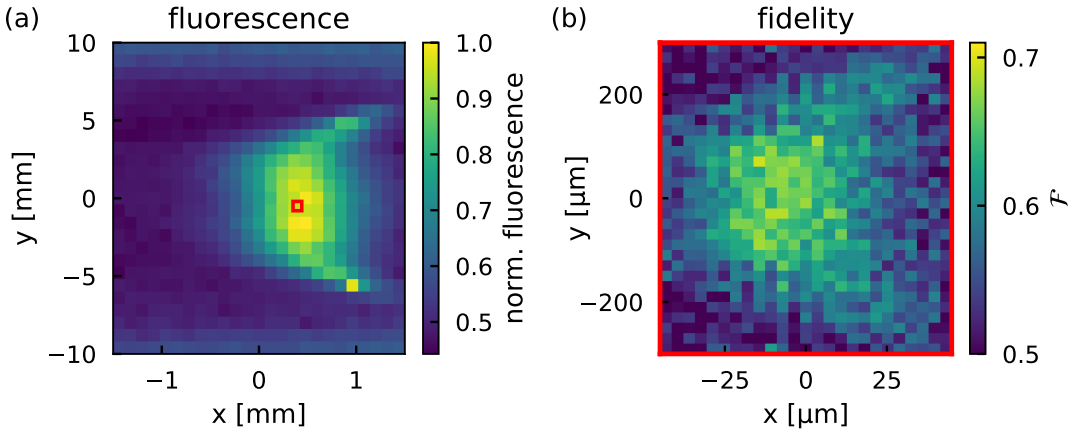

Figure 4.6: Alignment of the bias magnetic field. **(a)** NV fluorescence for different positions of the two magnets. Good alignment is visualized as a bright area, as the NV centers fluorescence is quench by off-axis fields. **(b)** SSR fidelity for different positions of the permanent magnets. The area of high fidelity indicates precise alignment of the magnetic field. The feature seen in the fidelity signal is much narrower than the one in the NV fluorescence. The scan area of the fidelity scan is indicated by a red rectangle in (a).

4.2.3 Manipulation of the nuclear spin

Like the electron spin, the nuclear spin can be manipulated by resonant electromagnetic waves that induce Rabi oscillations, which were introduced in Section 1.4 of this thesis. Due to the smaller gyromagnetic ratio of nuclear spins, the resonance frequencies are in the radio frequency (RF) range (~MHz). The pulse sequence used to observe the response of the nuclear spin to a RF pulse is depicted in Fig 4.7a. First, a RF pulse with frequency ω_n and duration τ_{RF} manipulates the nuclear spin. Afterwards, the nuclear spin state is read out by a SSR sequence. The SSR sequence differs to the sequence introduced in Section 4.2.1 (see Fig 4.2b). Here, both nuclear spin states are probed by successively applying MW pulses with frequencies ω_1 and ω_2. The photons are collected separately for both frequencies and the spin state is determined by comparing the two photon counts. This way, no photon count threshold is needed to differentiate between the two spin states, making the technique robust against slow fluctuations of the average photon count rate.

Repeating of the complete sequence results in a trace of the nuclear spin state projected into the $m_I = \pm 1/2$ basis. If the nuclear spin state is not changed by the RF pulse, e.g. because it is far off-resonant, the trace will show a spin flip rate according to the maximum readout fidelity $\mathcal{F}_{\mathrm{max}}$. If the RF pulse changes the spin state, the rate of nuclear spin flips will increase and the calculated fidelity will decrease. For a perfect π-pulse, the nuclear spin flips between every readout, leading to a fidelity of $(1 - \mathcal{F}_{\mathrm{max}})$. However, this is in general not observed in NV centers, as switching of the charge state leads to off-resonant RF-pulses. This effect is even more prevalent in the investigated shallow NV centers.

A Rabi oscillation of the intrinsic ^{15}N spin, recorded by varying the pulse duration τ_{RF}, is shown in Fig 4.7b. Because of the weak coupling of the nuclear spin to its environment, the observed nuclear Rabi frequency of $f_{\mathrm{Rabi}}^{(n)} = 23.4$ kHz is slower, compared to Rabi oscillations of the NV center's electron spin. By varying the frequency ω_n of the RF-pulse, the nuclear magnetic resonance of the nitrogen spin can be observed (see Fig 4.7c). The resonance was observed at a frequency of $\omega_n/(2\pi) = 1.225$ MHz, which corresponds to an absolute magnetic field strength of $B = \omega_n/\gamma_{^{15}\mathrm{N}} = 0.28$ T, where $\gamma_{^{15}\mathrm{N}}/(2\pi) = -0.4316$ MHz T^{-1} is

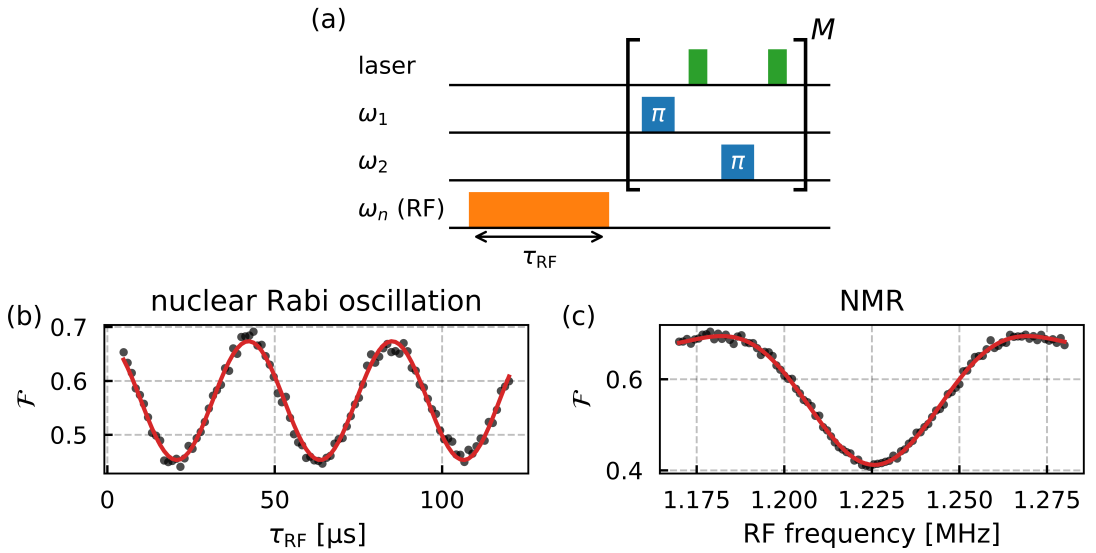

Figure 4.7: Manipulation of the intrinsic ^{15}N nuclear spin of a NV center. **(a)** Sequence used to manipulate and read out the nuclear spin. First, Rabi oscillations, introduced by a RF-pulse, alter the nuclear spin state. Afterwards, the nuclear spin state is read out by a SSR sequence. The SSR is performed continuously on both spin states to make the measurement robust against fluctuations of the photon count rate. **(b)** Rabi oscillation ($f^{(n)}_{\text{Rabi}} = 23.4$ kHz) of the nuclear spin. **(c)** Nuclear magnetic resonance (NMR) recorded by varying the frequency ω_n of the RF-pulse.

the gyromagnetic ratio of ^{15}N. This observation fits well to the magnetic field determined via the Zeeman shift of the electron spin state (see Section 4.2.1).

4.3 Nuclear Quantum-assisted sensing

In this section, the SSR of the electron spin is discussed. In the first subsection, the experimental implementation of SSR-assisted quantum sensing is presented. As a demonstration, the electron spin T_1 is measured via the nuclear spin. As a comparison, the same measurement was performed using the standard optical readout of the electron spin state. The SNR of both techniques under the same experimental conditions is compared.

In the second subsection, the SNR of both methods is calculated theoretically. By comparing the two methods, the parameter regime resulting in an improved sensing time can be identified.

4.3.1 Benchmark experiments

The sequence used for SSR-assisted sensing experiments is depicted in Fig 4.8. First, a sensing protocol is performed on the electron spin. Afterwards, the nuclear spin state is flipped conditionally on the electron spin state by a C_eNOT_n-gate, in form of a RF π-pulse resonant to the nuclear spin state transition. Finally, the nuclear spin state is detected via a SSR sequence as described in Section 4.2.3.

To demonstrate this technique, the longitudinal spin decay (T_1) of the electron spin was measured using the SSR readout. The electron spin sensing protocol is alternating between the two sequences (MW_0 and MW_π) introduced in Section 1.5.2 and the fidelity is recorded separately for each variant. The final measurement result is the difference between the two fidelity signals $\Delta\mathcal{F} = \mathcal{F}_0 - \mathcal{F}_\pi$. Fig 4.9a shows the spin decay of a NV center's electron spin detected by SSR. From the observed signal, a spin lifetime of $T_1 = 13.8 \pm 1.3$ µs was determined. The maximum fidelity contrast of ≈ 0.13 ($\tau_{sens} = 0$) is lower than the fidelity contrast of ≈ 0.28 observed in the NMR signal of the same NV center (see Fig 4.7c). This is caused by the long duration of the nuclear π-pulse $\tau_{\pi,n} = 21.4$ µs, which is on the order of the electron spin lifetime. The electron

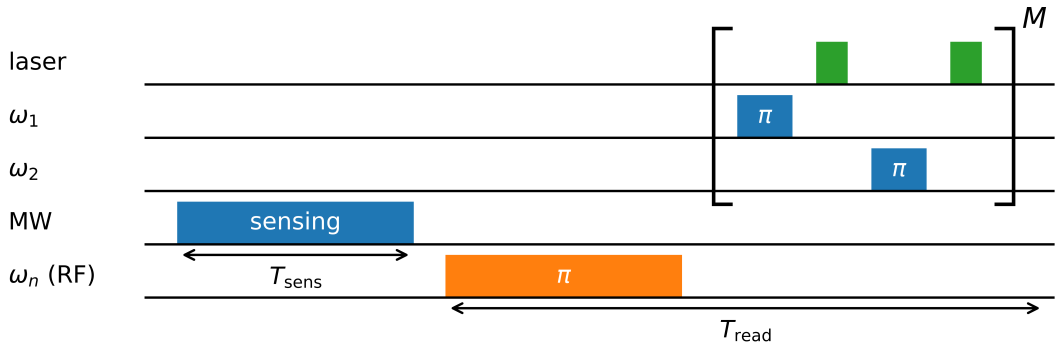

Figure 4.8: Pulse sequence of the nuclear quantum-assisted sensing technique. First, a sensing protocol is preformed on the electron spin (MW, blue). Afterwards, the nuclear spin is flipped conditional on the electron spin state by a RF π-pulse (RF, orange). Finally, a SSR of the nuclear spin is executed.

spin is decaying significantly during the RF pulse, leading to a decrease of the detected contrast.

As a comparison, a T_1 measurement using the standard optical readout, which was introduced in Section 1.5.1 is shown in Fig 4.9c. Both measurements ran for 5 minutes and show the same decay time within the measurement error.

To compare the performance of the two readout techniques, both measurements were repeated 243 times with a runtime of 5 minutes each. The resulting T_1 values are shown in Fig 4.9c,d. The average T_1 of the SSR-assisted measurements is $T_1^{SSR} = 13.8 \pm 1.5$ µs. The same average spin lifetime is detected via the standard optical readout $T_1^{Std} = 13.8 \pm 1.8$ µs. Here, the standard deviation of the extracted T_1 values has been taken as the error. The average SNR ratios of the individual measurements for each technique are $SNR^{SSR} = 9.28$ and $SNR^{Std} = 8.12$. A summary of the retrieved values is shown Table 4.3.1. The sensing performance is slightly improved by the use of SSR under the given experimental conditions. As will be discussed in the next section, this improvement gets more significant for higher fidelity contrasts and longer sensing sequences.

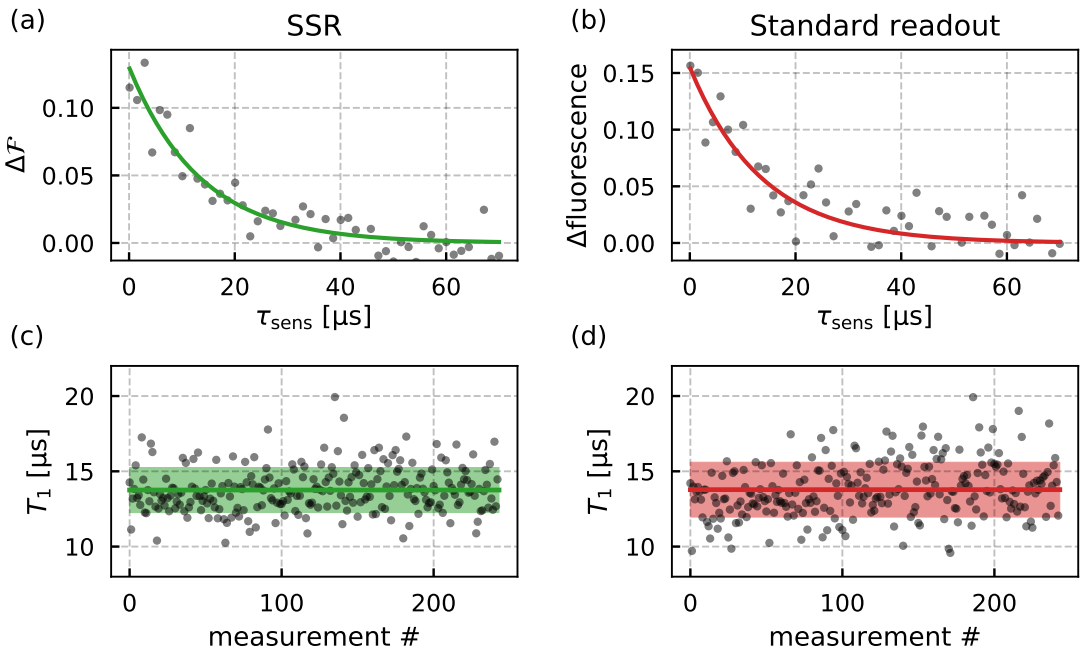

Figure 4.9: **(a)** Nuclear quantum-assisted measurement of the longitudinal spin decay of the electron spin. The sensing sequence is alternatingly performed with and without an electron π-pulse. The detected signal is the fidelity contrast $\Delta\mathcal{F}$ between the fidelities measured for each sensing protocol variant. **(b)** Comparison measurement of the longitudinal electron spin decay performed on the same NV center using the direct optical readout of the electron spin. The signal shows the same spin lifetime as the SSR-based measurement in (b). **(c)** T_1 values obtained from 243 individual SSR-assisted measurements performed on the same NV. Each measurement was running for 5 minutes. The average spin lifetime is $T_1 = 13.8 \pm 1.3$ µs (green line). The standard deviation of the T_1 values is indicated by the light green area. **(d)** T_1 values resulting from 243 measurements using the standard optical readout of the electron spin. The average spin lifetime $T_1^{\text{Std}} = 13.8 \pm 1.8$ (red line) fits to the nuclear quantum-assisted results shown in (d). However, the standard deviation σ (light red area) is slightly higher with the standard optical readout.

Table 4.3.1: Comparison of T_1 measurements using the standard optical readout of the electron spin (Std) and the nuclear quantum-assisted sensing technique (SSR). With both techniques, 243 measurements with a runtime of 5 minutes each were performed. Shown is the average spin lifetime (T_1), the standard deviation of the measured spin lifetimes ($\sigma(T_1)$), the average SNR of the measurements and the theoretically calculated SNR based on the experimental parameters and conditions.

parameter	**Std**	**SSR**	**SSR/Std**
T_1 [µs]	13.8	13.8	-
$\sigma(T_1)$ [µs]	1.8	1.5	0.83
average SNR (experiment)	8.12	9.28	1.14
SNR (theory)	11.12	13.56	1.22

4.3.2 Theory

To get an estimate of the performance improvement of a sensing experiment utilizing the SSR sequence introduced in the previous section, its theoretical SNR is calculated in this section and compared to the same measurement with the standard optical readout of the electron spin. The SNR for both methods is calculated in dependence of the duration of the sensing sequence performed on the electron spin and the maximum fidelity of the SSR. To make the theoretical values comparable to the previously shown experimental results, the calculation of the SNR is based on the used experimental parameters. First, expressions for the SNR of each technique are derived, following the work of Häberle et al. [21]. Afterwards, the results are compared to the experimental data.

SNR using a direct optical readout of the electron spin

As discussed in Section 1.5.2, the signal of a measurement, utilizing the standard optical readout of the electron spin, is generated using four different photon counts: ν_0, ν_π, $\nu_{0,\mathrm{r}}$ and $\nu_{\pi,\mathrm{r}}$ (see Eq. (1.11)). The shot noise of each photon count is the square root of the number of collected photons $\Delta\nu = \sqrt{\nu}$. Assuming

a shot noise limited measurement, the total uncertainty $\Delta\mathcal{S}$ of Eq. (1.11) is

$$\Delta\mathcal{S} = \sqrt{\left(\frac{1}{\nu_{0,\mathrm{r}}}\sqrt{\nu_0}\right)^2 + \left(\frac{1}{\nu_{\pi,\mathrm{r}}}\sqrt{\nu_\pi}\right)^2 + \left(\frac{\nu_0}{\nu_{0,\mathrm{r}}^2}\sqrt{\nu_{0,\mathrm{r}}}\right)^2 + \left(\frac{\nu_\pi}{\nu_{\pi,\mathrm{r}}^2}\sqrt{\nu_{\pi,\mathrm{r}}}\right)^2}. \tag{4.4}$$

The number of photons in the two reference signals can be approximated to be equal $\nu = \nu_{0,\mathrm{r}} = \nu_{\pi,\mathrm{r}}$. Furthermore, the number of signal photons can be expressed relative to the reference photons, using the respective enhancement constants c_0 and c_π [71], as

$$\nu_0 = c_0\nu \tag{4.5}$$

$$\nu_\pi = c_\pi\nu. \tag{4.6}$$

Eq. (4.4) then simplifies to

$$\Delta\mathcal{S} = \sqrt{\frac{2}{\nu}\left(c_0^2 + c_\pi^2\right)} \tag{4.7}$$

and the SNR using the standard optical readout of the electron spin becomes

$$\mathrm{SNR}_{\mathrm{Std}} = \frac{\mathcal{S}}{\Delta\mathcal{S}} = \sqrt{\frac{\nu}{2(c_0^2 + c_\pi^2)}}(c_0 - c_\pi). \tag{4.8}$$

The number of photons $\nu = \tilde{\nu} f_{\mathrm{read}} T_{\mathrm{run}}$ depends on the average number of photons $\tilde{\nu}$ detected during a single readout, the frequency of readouts f_{read} and the total runtime T_{run}. The readout frequency for each of the sequence variants is defined by the duration of the sensing sequence T_{sens} and the duration of the readout T_{read} (see Fig 4.8) as

$$f_{\mathrm{read}} = \frac{1}{4(T_{\mathrm{sens}} + T_{\mathrm{read}})}. \tag{4.9}$$

The number of photons detected during a single readout can be calculated using the average photon count rate of the NV center β and the duration of the readout laser pulse τ_0 as

$$\tilde{\nu} = \beta\tau_0. \tag{4.10}$$

Finally, the SNR exclusively expressed in terms of experimental parameters is

$$\mathrm{SNR}_{\mathrm{Std}} = \sqrt{\frac{\beta\tau_0 T_{\mathrm{run}}}{8(c_0^2 + c_\pi^2)(T_{\mathrm{sens}} + T_{\mathrm{read}})}}(c_0 - c_\pi). \tag{4.11}$$

SNR using SSR

The signal of the SSR-based sensing experiment is defined as the difference between the non-flip probabilities, p_0 and p_π, of the two sequence variants

$$\mathcal{S}_{\mathrm{SSR}} = p_0 - p_\pi. \tag{4.12}$$

Both signals follow a binomial distribution, leading to a standard deviation of

$$\sigma = \sqrt{\frac{p(1-p)}{N}}, \tag{4.13}$$

where N is the number of performed readouts. The uncertainty of the complete signal is then

$$\Delta\mathcal{S}_{\mathrm{SSR}} = \sqrt{\frac{p_0(1-p_0) + p_\pi(1-p_\pi)}{N}}. \tag{4.14}$$

Using $N = T_{\mathrm{run}}/(2(T_{\mathrm{sens}} + T_{\mathrm{read}}))$ the SNR can be expressed using solely experimental parameters

$$\mathrm{SNR}_{\mathrm{SSR}} = \frac{\mathcal{S}_{\mathrm{SSR}}}{\Delta\mathcal{S}_{\mathrm{SSR}}} = \sqrt{\frac{T_{\mathrm{run}}}{2(p_0(1-p_0) + p_\pi(1-p_\pi))(T_{\mathrm{sens}} + T_{\mathrm{read}})}}(p_0 - p_\pi). \tag{4.15}$$

Comparison to experiments

Fig 4.10 shows the ratio between the SNRs using the standard optical readout and SSR for different readout fidelities and durations of the sensing sequence. The values were calculated using Eq. (4.11) and Eq. (4.15). All other parameters are set according to the conditions prevalent at the experiments presented in Section 4.3.1. A list of all parameter values is given in Table 4.3.2.

The presented benchmark experiment, with $p_0 = 0.58$, $p_\pi = 0.45$ and an average waiting time $\tau = 35$ µs, is indicated by an orange marker in Fig 4.10. The calculated ratio between the SNRs for this parameter set is 1.22, which fits well to the ratio of 1.14 found in the experiment. The individual SNRs from the calculation are $\mathrm{SNR}_{\mathrm{Std}} = 11.12$ and $\mathrm{SNR}_{\mathrm{SSR}} = 13.56$. These values are slightly higher than observed in the experiment (see Table 4.3.1). This is expected as only shot noise was considered in the calculation.

[4] In the experiment, the total runtime of 5 minutes is split between 50 different waiting times τ. Hence, the runtime for each individual bin is 6 s.

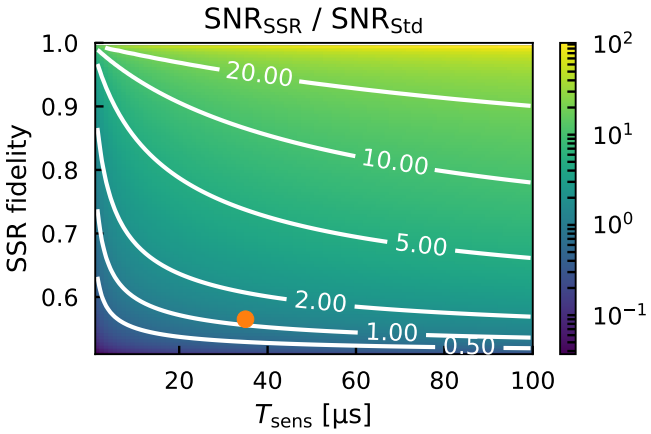

Figure 4.10: Calculated values for the ratio between the SNRs achieved with a standard optical readout and a quantum nuclear-assisted readout. All parameters of the calculation were chosen to resemble the experimental conditions of the experiments presented in Section 4.3.1. The orange marker indicates the fidelity and sensing time of the experiment.

Table 4.3.2: Values used for the calculation shown in Fig 4.10.

parameter	value
c_0	1.05
c_π	0.86
β	1.1×10^6 cps
τ_0	300 ns
$T_{\text{read,Std}}$	300 ns
$T_{\text{read,SSR}}$	470 µs
T_{run}	6 s [4]

4.4 Summary

In summary, it was shown that the SSR technique can improve the SNR of a NV-based sensing measurement. The achievable gain in SNR depends on the fidelity of the SSR and the duration of the sensing sequence. Hence, the technique only offers an advantage under certain experimental conditions. Shot

noise limited expressions for the SNR with and without the nuclear quantum assisted protocol were derived in this chapter and are given with Eq. (4.11) and Eq. (4.15). This allows to evaluate the benefits arising from a SSR-assisted measurement under specific experimental conditions.

As an experimental demonstration, the T_1 time of a NV center was subsequently measured with both techniques. Under the prevalent experimental conditions a 14% improvement of the SNR was observed. This fits well to the theoretically calculated improvement of 22%. The experiment was conducted under the spatial restrictions posed by an AFM (Asylum Research, MFP-3D) placed above the sample. This limited the bias magnetic field to 0.28 T, which was achieved using a custom-designed tip holder and suitable setup of permanent magnets. The SNR gain resulting from the SSR assisted measurement could be further increased by a stronger bias magnetic field. Häberle et al. [21] demonstrated a 8.6-fold improvement of the SNR at a bias magnetic field of ~0.4 T using the same measurement technique as presented in this chapter.

The presented nuclear quantum assisted technique is especially beneficial in the case of long sensing sequences. Thus, it is suitable for high order dynamical decoupling sequences used for nanoscale NMR [101, 17] and correlation spectroscopy [102, 103]. Furthermore, using the direct control of the nuclear memory spin, it can be used together with the NV center's electron spin as a combined quantum sensor. Utilizing entangled states of the two spins, the sensitivity of the electron spin and the long lifetime of the nuclear spin can be exploited to improve the resolution of NV-based NMR spectroscopy [104, 105, 106].

Chapter 5

5 NV-mechanical hybrid systems

Contents

5.1 Introduction

The capability of observing and controlling single quantum systems has greatly increased over the last decades. This paved the way towards new technologies like quantum computing [107, 5], quantum sensing [8] and secure quantum communication [9]. However, these application still comprise great challenges. Quantum systems, like e.g. superconducting circuits, solid state spins and quantum dots, are inherently fragile and need to be well isolated from their environment to minimize decoherence. At the same time, a coupling to the environment is required to realize multi-qubit networks or quantum sensing. A practical solution is to combine different types of quantum systems, and thereby combine their individual strengths to create more robust and powerful quantum devices [108]. Such novel quantum hybrid devices require interfaces between different kinds of physical system. Potent candidates to act as such interaction-mediating interfaces are mechanical systems. In the last decade, technological advances allowed to bring mechanical resonators into the quantum regime [23, 22, 24, 25]. Such systems can be sensitive to a variety of different forces, including e.g. capacitive forces, magnetic forces and radiation pressure. Consequently, mechanical resonators were successfully coupled to various types of quantum system, like e.g. superconducting qubits [26, 23, 27, 28], photons [29] and solid-state spins [30, 31, 32, 33, 34]. NV centers have successfully been coupled to mechanical resonators in the form of cantilevers [33, 35, 36, 37, 38], bulk resonators [39, 40], membranes [34] and surface acoustic waves [41].

In this chapter, the prospects of a NV-mechanical hybrid system, comprised of single NV centers coupled to an array of coupled mechanical resonators, are discussed. Prove of principle experiments, using a pair of coupled mechanical cantilevers hosting single NV centers, are presented. For this purpose, a thorough characterization of the studied system was preformed, which is described in Section 5.4 and Section 5.5. Afterwards, two potential applications of the studied system are investigated. First, the use of the cantilever pair as a quantum bus, mediating spin-spin interactions, is discussed in Section 5.6. Second, the capability of the hybrid system as a high-sensitivity mass sensor is studied in Section 5.7. Results of this chapter were published in [109].

5.2 Mechanical resonators

5.2.1 Cantilevers

Singly clamped beams, also known as cantilevers, are an important class of micro- and nanomechanical resonators. In the next section, strain and stress induced by a static bending of such devices is discussed. Afterwards, vibrations of single and coupled cantilevers are introduced. This is followed by a discussion of the quantum mechanical description of mechanical resonators in the last section.

In the following, we consider a thin cantilever elongated along the x-axis with length L, width W and thickness T (see Fig 5.1).

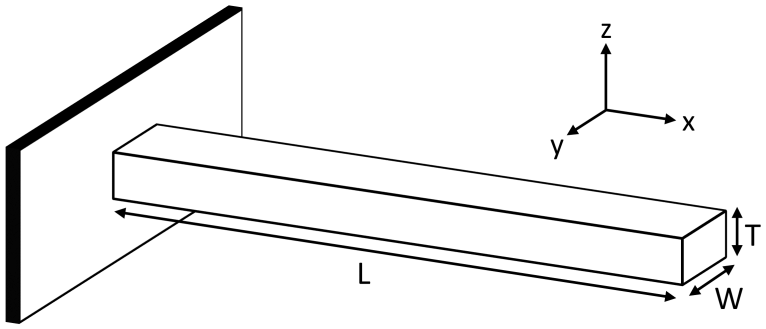

Figure 5.1: Definition of the coordinate system and cantilever geometry. The cantilevers have length L along the x-axis, the width W along the y-axis and the thickness T along the z-axis. Vibrations in z-direction are referred to as out-of-plane vibrations.

Static bending

For small deflections, the cantilever bending $u(x)$ is given by the Euler-Bernoulli beam theory as

$$\frac{\partial^2}{\partial x^2} u(x) = \frac{M(x)}{EI} \tag{5.1}$$

where M is the bending moment, E is the Young's modulus and $I = \iint_A z^2 \, dz \, dy = \frac{WT^3}{12}$ is the moment of inertia of the cantilever. The moment induced by a static

force F is $M(x) = F(L-x)$. This results in a bending along the cantilever

$$u(x) = \frac{F}{EI}\left(\frac{Lx^2}{2} - \frac{x^3}{6}\right) \tag{5.2}$$

and the deflection of the free end

$$u(L) = \frac{L^3}{3EI}F. \tag{5.3}$$

For small deflections, the restoring force is approximately linear. Therefore, by comparing Eq. (5.3) to Hooke's law $F = ku(L)$, we can get an expression for the spring constant k of the cantilever

$$k = \frac{EWT^3}{4L^3}. \tag{5.4}$$

Vibrations

As in the static case, the dynamics of thin beams (L>h) can also be described using the Euler-Bernoulli beam theory. To simplify the calculation of vibrational modes, it is convenient to first introduce several assumptions. We assume a linear elastic material and small deflections. Furthermore, we only consider out-of-plane oscillations along the z-axis. The equation of motion is then given by

$$EI\frac{\partial^4 z}{\partial x^4} + \rho A\frac{\partial^2 z}{\partial t^2} = F(x), \tag{5.5}$$

where E is the Young's modulus, I the moment of inertia, ρ the density and $A = WT$ the cross-section area[110, 111, 112]. Anticipating a time-periodic solution, we use the Ansatz

$$z(x,t) = u(x)e^{i\omega_n t}. \tag{5.6}$$

for the nth mode. As a result we obtain a differential equation for the position dependent mode shape $u(x)$

$$\frac{\partial^4 u(x)}{\partial x^4} = (\alpha_n)^4 u(x) \tag{5.7}$$

with $\alpha_n = (\rho A\omega_n^2/EI)^{1/4}$. The general solution of this differential equation is [111, 110]

$$u_n(x) = a_n \sin(\alpha_n x) + b_n \cos(\alpha_n x) + c_n \sinh(\alpha_n x) + d_n \cosh(\alpha_n x). \tag{5.8}$$

With the boundary conditions $u(0) = 0$, $\frac{\partial}{\partial x}u(0) = 0$, $\frac{\partial^2}{\partial x^2}u(L) = 0$ and $\frac{\partial^3}{\partial x^3}u(L) = 0$ (fixed clamping point at $x = 0$ and no curvature or momentum at free end $x = L$) we get an equation for allowed values of the parameter $K_n = \alpha_n L$

$$\cos(\alpha_n L)\cosh(\alpha_n L) + 1 = 0. \tag{5.9}$$

Numerical values for the first three modes are $K_1 = 1.8751$, $K_2 = 4.6941$, $K_3 = 7.8548$ [112]. Fig 5.2 shows the corresponding mode shapes. Using the defini-

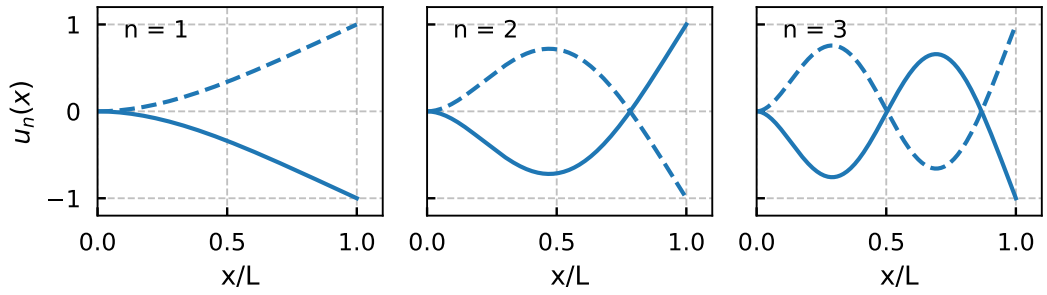

Figure 5.2: Normalized mode shapes $u_n(x)$ of the first 3 vibrational modes of a cantilever with length L and a clamping point at $x = 0$. The solid and dashed lines represent the maximum and minimum position of the oscillation.

tion of α_n, we get an expression for the mode frequencies

$$\omega_n = \left(\frac{K_n}{L}\right)^2 \sqrt{\frac{EI}{\rho A}} = T\left(\frac{K_n}{L}\right)^2 \sqrt{\frac{E}{12\rho}}. \tag{5.10}$$

5.2.2 The harmonic oscillator

Free undamped vibrations

For small driving forces, the dynamics of a cantilever can be approximated with an harmonic oscillator. The general equation of motion of an harmonic oscillator is

$$m_{\text{eff}}\ddot{z} + c\dot{z} + kz = F(t) \tag{5.11}$$

where m_{eff} is the effective mass, k is the spring constant, c is the damping coefficient and $F(t)$ is an external driving force. Inserting the Ansatz $z(t) = z_0 e^{i\omega t}$

while considering a free and umdamped harmonic oscillator ($F(t) = 0$ and $c = 0$), we get an expression for the eigenfrequency Ω of the oscillator

$$\Omega = \omega = \sqrt{\frac{k}{m_{\text{eff}}}}. \tag{5.12}$$

Using Eq. (5.10), Eq. (5.12) and Eq. (5.4) we can calculate the effective mass of a singly clamped cantilever

$$m_{\text{eff}} = \frac{3}{K_1^4}\rho LWT \approx \frac{1}{4}m. \tag{5.13}$$

Alternatively, the effective mass of arbitrarily-shaped mechanical resonators can be calculated by comparing the kinetic energy of the resonator and the harmonic oscillator model. In general, the effective mass is different for each vibrational mode of the resonator. For a mode n with the normalized mode shape $\phi_n(\mathbf{r})$ and the amplitude $U_{0,n}$ one gets

$$\frac{1}{2}\rho \int_V \left(\frac{\partial}{\partial t} U_{0,n}\phi_n(\mathbf{r})\cos(\omega t)\right)^2 d\mathbf{r} = \frac{1}{2}m_{\text{eff},n}\left(\frac{\partial}{\partial t} z_0 \cos(\omega t)\right)^2. \tag{5.14}$$

Setting $z_0 = U_{0,n}$, we get an expression for the effective mass

$$m_{\text{eff},n} = \rho \int_V \phi_n(\mathbf{r})^2 d\mathbf{r}. \tag{5.15}$$

Free damped vibrations

In case of a free weakly-damped oscillator ($F(x) = 0$ and $c \neq 0$), the solution of Eq. (5.11) is

$$z(t) = z_0 e^{-\Omega\zeta t}\cos(\Omega\sqrt{1-\zeta^2}t) \tag{5.16}$$

where $\zeta = \frac{c}{2\Omega}$ is the damping ratio [111]. Eq. (5.16) is plotted in Fig 5.3a. Note that this solution is only valid for $\zeta < 1$. The solution describes an exponentially decaying oscillation with the natural frequency $\omega_{\text{nat}} = \Omega\sqrt{1-\zeta^2}$. A common parameter to express the damping of a system is the quality factor Q. There are multiple definitions of the quality factor. However, all of them are equivalent for weakly damped systems. The quality factor can be defined as the ratio between the energy stored in a resonator and the energy lost during one cycle of the oscillation

$$Q := 2\pi\frac{W}{\Delta W}. \tag{5.17}$$

Calculating the stored energy and energy loss leads to a relation between the quality factor and the damping ratio

$$Q = \frac{\sqrt{1-2\zeta^2}}{2\zeta}. \tag{5.18}$$

For small damping ratios the quality factor can approximated as $Q \approx \frac{1}{2\zeta}$. Using Eq. (5.16), the exponential decay of a free oscillator can be expressed with the quality factor

$$z_0(t) = z_0(0)e^{-\frac{\Omega}{2Q}t}. \tag{5.19}$$

Thus, measuring the ringdown of an oscillating resonator can be used to determine the quality factor of the system.

Driven damped vibrations

For a damped oscillator, driven by a periodic external force $F = F_0 \sin \omega t$, the solution of Eq. (5.11) is [111]

$$z(t)\frac{F_0/m}{\sqrt{(\Omega^2-\omega^2)^2+4\zeta^2\Omega^2\omega^2}}\cos(\omega t+\varphi) \tag{5.20}$$

with the phase

$$\varphi = \arctan\frac{2\zeta\Omega\omega}{\omega^2-\Omega^2}. \tag{5.21}$$

The resonator oscillates with the drive frequency ω and has a phase-shift φ relative to the driving force. The oscillation amplitude is proportional to the driving force amplitude F_0. We can also express the amplitude and phase using the relative phase ω/Ω. This leads to the amplitude

$$|z_0| = \frac{F_0/k}{\sqrt{\left(1-(\frac{\omega}{\Omega})^2\right)^2+4\zeta^2(\frac{\omega}{\Omega})^2}} \tag{5.22}$$

and phase

$$\varphi = \arctan\frac{2\zeta(\frac{\omega}{\Omega})}{(\frac{\omega}{\Omega})^2-1}, \tag{5.23}$$

which are also shown in Fig 5.3b,c. The amplitude and phase behavior changes when the oscillator is driven by a periodic displacement. This is e.g. the case

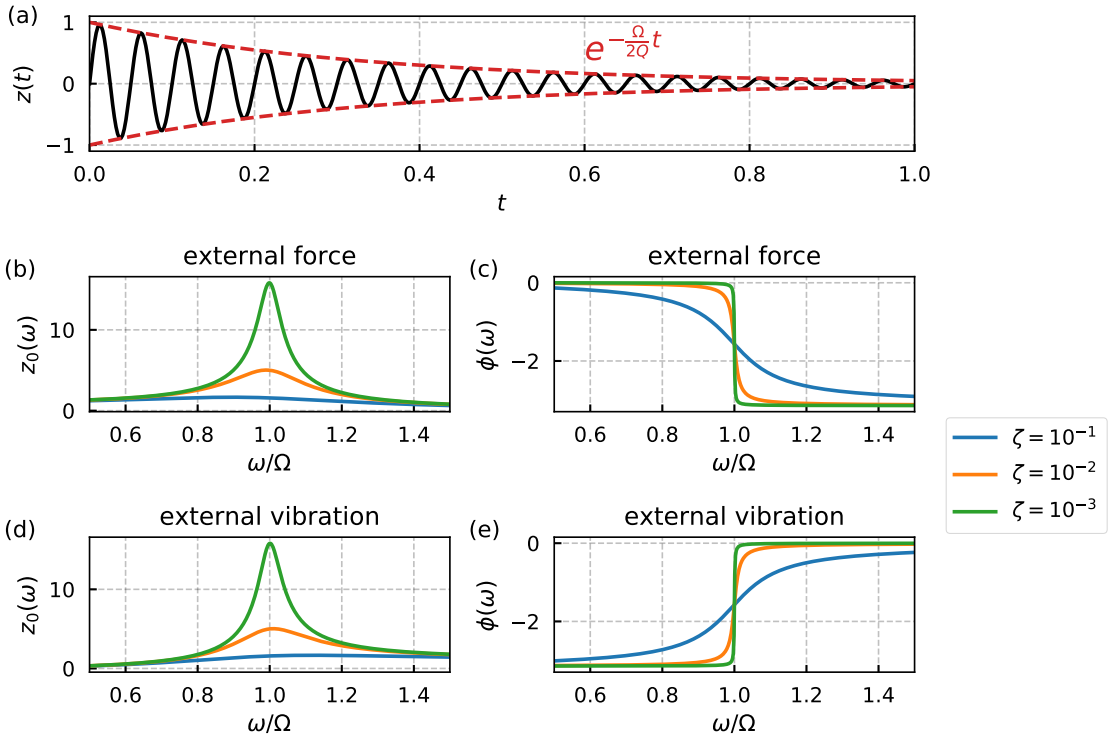

Figure 5.3: **(a)** Exponentially decaying oscillation of a free damped harmonic oscillator. The oscillator vibrates with the natural frequency ω_{nat} and a decay rate defined by the quality factor Q. **(b)** Amplitude z_0 and **(c)** phase φ of a damped harmonic oscillator, driven by an external force, over the relative frequency ω/Ω. A lower damping results in a higher amplitude and narrower resonance peak. **(d)** Amplitude and **(e)** phase when the harmonic oscillator is driven by a periodic displacement.

if the oscillator vibration is excited by a piezo-element shaking the sample. In this case the amplitude and phase are

$$|z_0| = \frac{\frac{F_0}{k}(\frac{\omega}{\Omega})}{\sqrt{\left(1-(\frac{\omega}{\Omega})^2\right)^2 + 4\zeta^2(\frac{\omega}{\Omega})^2}} \tag{5.24}$$

and

$$\varphi = \arctan\frac{2\zeta(\frac{\omega}{\Omega})}{(1-\frac{\omega}{\Omega})^2}. \tag{5.25}$$

Eq. (5.24) and Eq. (5.25) are displayed in Fig 5.3d,e. The drive frequency resulting in the highest amplitude is called the resonance frequency ω_r. In general, the resonance frequency does not coincide with the eigenfrequency Ω of the resonator. However, the difference between ω_r and Ω decreases with smaller damping rates. Thus, for high Q resonators $\omega_r \approx \Omega$ can be assumed. For driven oscillators, the quality factor can be defined as the ratio between the resonance frequency and the FWHM of the resonance peak

$$Q = \frac{\omega_r}{\Delta\omega}. \tag{5.26}$$

Two coupled harmonic oscillators

A pair of coupled mechanical resonators can be approximated as two harmonic oscillators connected by a spring with spring constant k' (see Fig 5.4b). At this point, we focus on symmetric systems, where both oscillators have the same mass m and spring constant k. The effect of imbalances between the two cantilevers is discussed in Section 5.7. The equations of motion are

$$-m\ddot{z}_1 = kz_1 + k'(z_1 - z_2) \tag{5.27}$$

and

$$-m\ddot{z}_2 = kz_2 + k'(z_2 - z_1). \tag{5.28}$$

The system exhibits two common ground modes at frequencies

$$\omega_1 = \sqrt{k/m} \;\; ; \quad \omega_2 = \sqrt{(k+2k')/m}. \tag{5.29}$$

ω_1 corresponds to the symmetric mode where both cantilevers oscillate in-phase. ω_2 on the other hand, corresponds to an anti-symmetric mode, where the cantilevers oscillate with a phase shift of π.

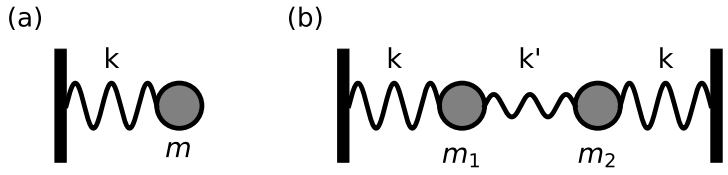

Figure 5.4: **(a)** Model of a harmonic oscillator consisting of a mass m fixed to a spring with spring constant k. **(b)** Model of two coupled harmonic oscillators. The two masses are connected via a spring with coupling constant k'.

5.2.3 Arrays of elastically coupled cantilevers

In this section, arrays of N elastically coupled cantilevers are discussed. An illustration of an array with $N = 6$ is shown in Fig 5.5. All cantilevers have the same geometry and are attached to a shared base plate of width B. They are distributed with an homogeneous spacing S. The coordinate system and the dimensions L, W and T of the cantilevers are as defined in Fig 5.1. The base plate and cantilevers have the same thickness. The coupling between the individual cantilevers is established purely mechanically via the shared base plate.

A cantilever pair ($N = 2$) is the smallest possible array of coupled cantilevers. The dynamics can be approximated by a system of two coupled harmonic oscillators, which was introduced in Section 5.2.2. Accordingly, the cantilever pair has two common modes - a symmetric mode at frequency ω_1 and an antisymmetric mode at frequency ω_2. A FEM simulation (COMSOL) of the mode shapes is shown in Fig 5.6a. Color-coded is the strain produced by the deformation of the structure. It can be seen that the strain is not limited to the cantilevers, but also extends into the shared base plate, visualizing the phonon-mediated coupling of the cantilevers.

To investigate the influence of the base plate geometry on the coupling strength between the cantilevers, FEM simulations of the resonance frequencies for different values of S and B were performed ($L = 100$ µm, $W = 4$ µm, $T = 2.5$ µm). Fig 5.6b shows the mode frequencies for different cantilever spacings at a fixed base plate width $B = 30$ µm. The frequency difference $d\omega = \omega_2 - \omega_1$ decreases

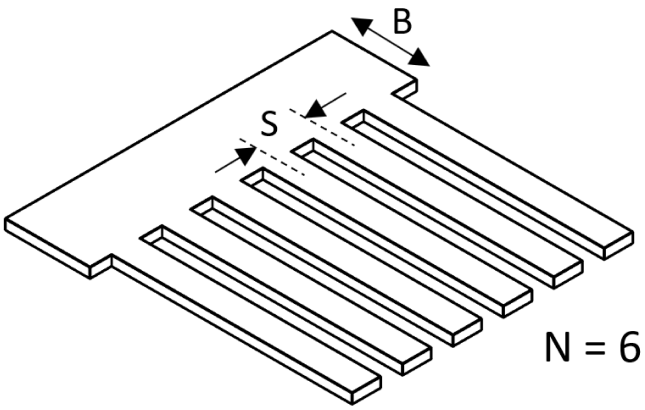

Figure 5.5: Illustration of an array of elastically coupled cantilevers with $N = 6$. The cantilevers are held by a shared base plate of width B. The cantilevers are homogeneously distributed with spacing S. The coupling between the cantilevers is mediated mechanically via the base plate.

with increasing cantilever distance. Accordingly, the relative coupling strength

$$\kappa = \frac{k'}{k} = \frac{\omega_2^2 - \omega_1^2}{\omega_1^2} \tag{5.30}$$

and the relative frequency difference

$$\xi = \frac{d\omega}{\omega_1} = \frac{\omega_2 - \omega_1}{\omega_1} \tag{5.31}$$

are both decreasing as shown in Fig 5.6c. The mode frequencies for different base plate width at a fixed spacing $S = 8$ µm is shown in Fig 5.6d. The corresponding relative couplings and frequency differences are presented in Fig 5.6e. The coupling increases with increasing B, as the area mediating the coupling gets larger. Consistently, the coupling vanishes for very small values of B, as no medium is left to transduce an interaction.

When using larger cantilever arrays, the scaling of the mode density with the number of cantilevers is important. An array of N cantilevers has N common modes. With a higher number of modes, the spacing between neighboring

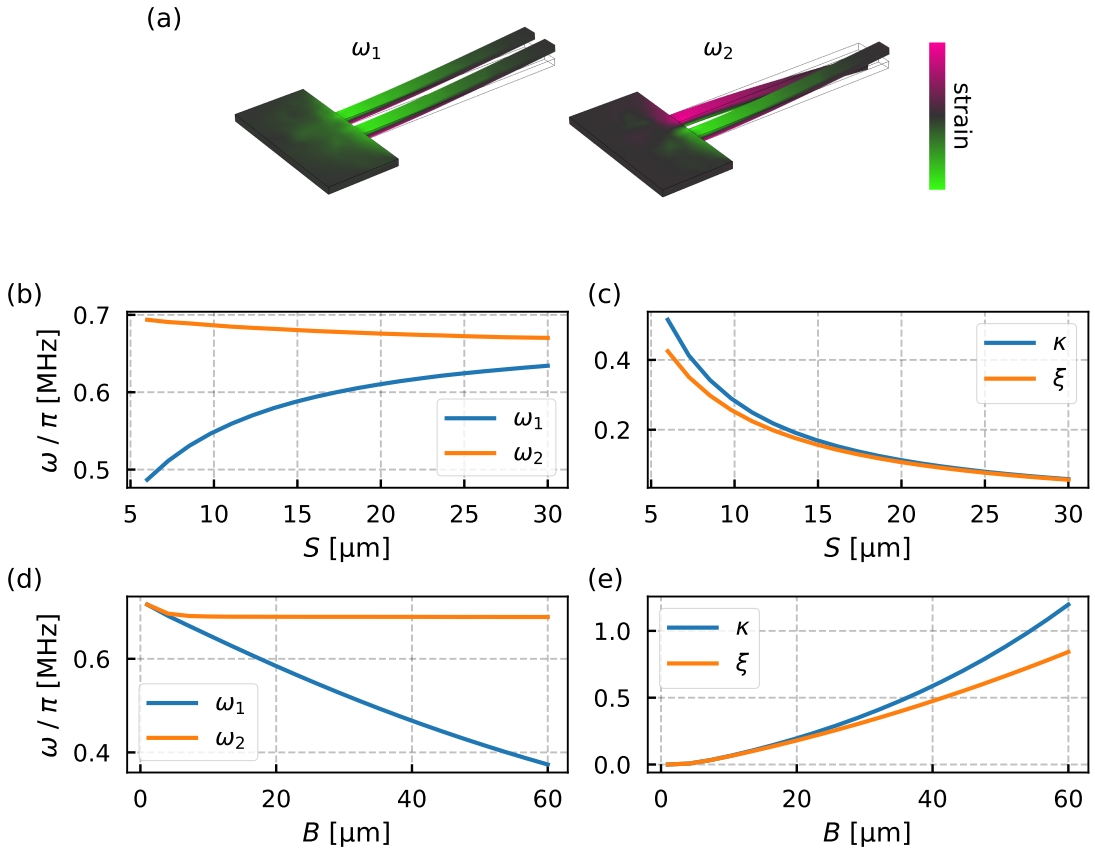

Figure 5.6: FEM simulation of a cantilever pair ($N = 2$). **(a)** Simulation of the mode shapes and the induced strain for both common modes. **(b)** Resonance frequencies of the system for varying spacings S of the cantilevers. **(c)** Relative coupling $\kappa = k'/k$ and relative frequency difference $\xi = d\omega/\omega_1$ for different cantilever spacings S. The coupling decreases with increasing distance between the cantilever. **(d)** Resonance frequencies of the system for varying widths B of the base plate. **(e)** Relative coupling and relative frequency difference for different widths B of the base plate. The coupling strength increases with increasing base plate width as the area mediating the cantilever-cantilever interaction is getting larger.

modes in frequency space will decrease. Hence, the mode density increases. At some point, the individual resonance peaks will partially overlap, rendering the addressing of individual modes impossible. To investigate the scaling behavior, FEM simulations of the frequencies of the first two modes were performed for a varying numbers of cantilever. Fig 5.7a shows the simulated values of the resonance frequency of the first (solid lines) and second (dashed lines) mechanical modes for a set of different widths of the base plate. The frequency of the first mode decreases with increasing B, as a larger sample area results in a reduced overall stiffness. Furthermore, the relative frequency difference decreases with the number of cantilevers (see Fig 5.7b). The solid lines are fitted curves of the form

$$\xi(N) = ae^{-\frac{N}{b}}. \tag{5.32}$$

The maximum number of cantilevers $N_{\max}$, that still allows resolving the first common mode, depends on the mechanical quality factor. Using 5.26 and 5.31, the maximum number of cantilevers can be estimated by the condition

$$\xi(N_{\max}) \stackrel{!}{=} \frac{1}{Q}. \tag{5.33}$$

From the fitted parameters of 5.32, the maximum number of cantilevers can be estimated as

$$N_{\max}(B, Q) = -b \ln\left(\frac{1}{aQ}\right). \tag{5.34}$$

Fig 5.7c shows the estimated maximum cantilever number over the width of the base plate for the quality factors $Q = 10^3$ and $Q = 10^6$. The calculated values show a roughly linear dependence and an increased maximum number of cantilevers with a higher quality factor. Furthermore, a wider base plate increases $N_{\max}$. This is expected as the cantilever coupling, and thereby the frequency spacing, is enhanced by the base plate width. $N_{\max}$ is plotted over the quality factor for different base plate widths in Fig 5.7d.

An important parameter of the cantilever array is its effective mass $m_{\text{eff},N}$. As can be seen in Eq. (5.15), the effective mass depends on the normalized mode shape $\phi_n \mathbf{r}$. To investigate the scaling of the effective mass, FEM simulations of the ground mode shapes for an increasing number of cantilevers were performed. As examples, the mode shapes for $N = 2$, $N = 10$ and $N = 20$ are shown in Fig 5.8a. The effective mass is then calculated from the mode shapes

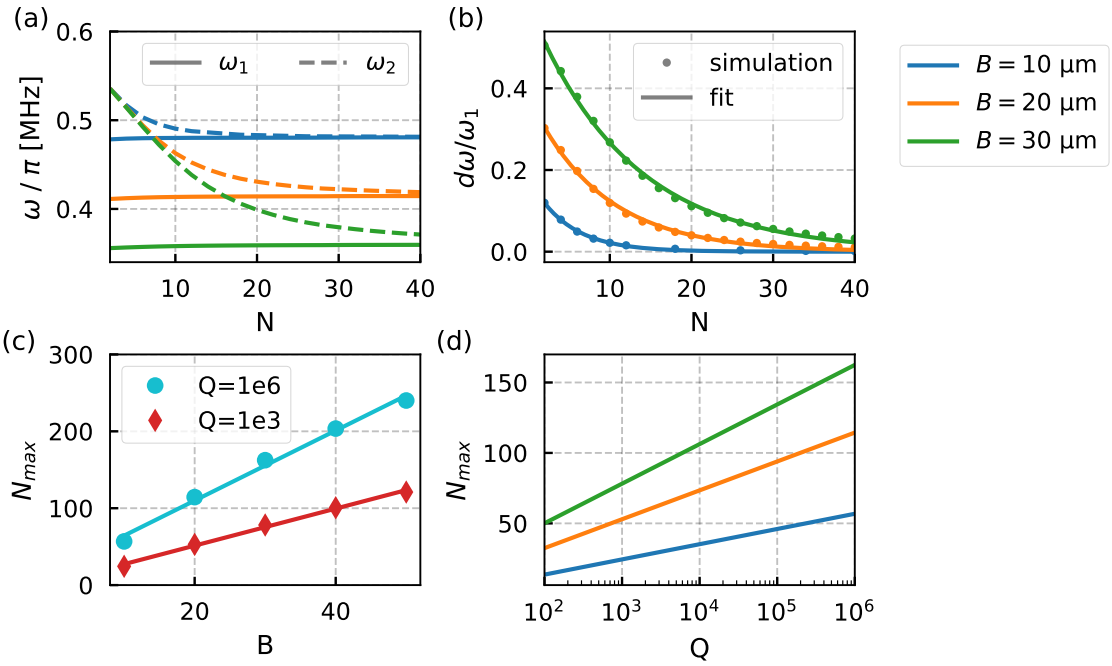

Figure 5.7: **(a)** FEM simulation of the first (solid lines) and second (dashed lines) resonance frequency of an array of N cantilevers. The simulation was performed for different width B of the base plate. **(b)** Relative frequency difference $\xi = (\omega_2 - \omega_1)/\omega_1$ of the simulated resonance frequencies. The mode density increases with the number of cantilevers, which is demonstrated by the decrease of the frequency difference. **(c)** Estimated maximum number of cantilevers N_{max} that still allow resolving the first mechanical mode. The values are generated from the fitted parameters of the curves in (b). A higher quality factor enables a higher amount of cantilever. **(d)** N_{max} over the quality factor of the array.

using Eq. (5.15). The resulting effective mass values are shown in Fig 5.8b. As a reference, the combined effective mass of N single and uncoupled cantilevers $N m_{\mathrm{eff},1} = N \frac{1}{4} \rho L W T$ is used. The deviation of the simulated effective mass from this reference is below 10% for $N < 40$. As the displacement of the base plate is relatively small, its influence on the overall effective mass is rather small. As a result, the approximation

$$m_{\mathrm{eff},N} \approx N m_{\mathrm{eff},1} \tag{5.35}$$

can be used for estimations of the system's scalability.

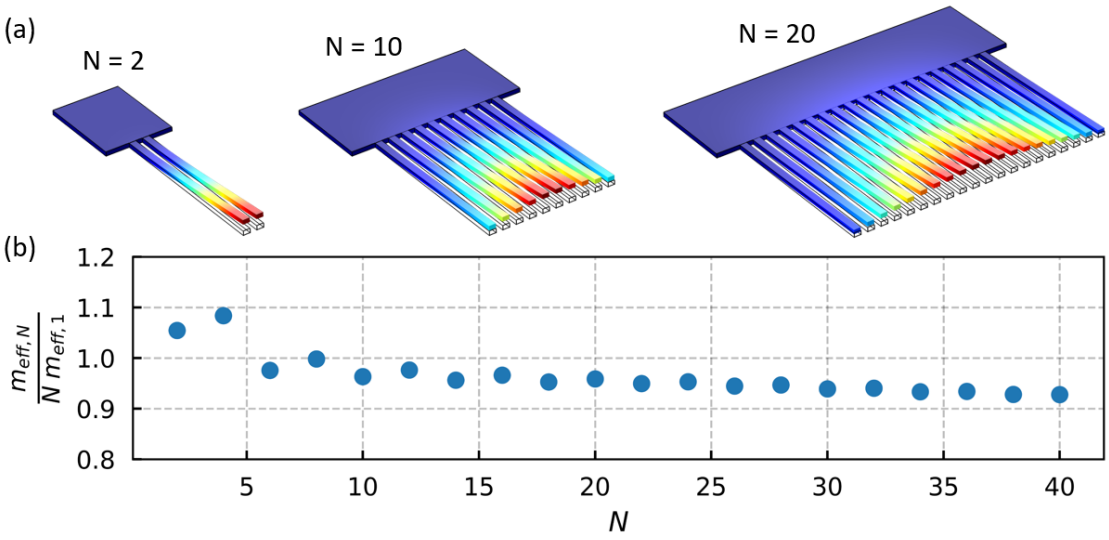

Figure 5.8: FEM simulation of the first vibrational mode of an array of N coupled cantilevers. **(a)** Mode shapes for different values for N. **(b)** Effective mass $m_{\mathrm{eff},N}$ of the cantilever array extracted from the simulation. The effective mass is compared to N-times the effective mass of a single cantilever $m_{\mathrm{eff},1} = \frac{1}{4} \rho L W T$. For $N < 40$, the deviation of the effective mass of the coupled array compared to N single cantilevers is below 10%.

5.2.4 Quantum mechanical description

The harmonic oscillator

In analogy to the classical undamped harmonic oscillator (see Eq. (5.11)), the quantum harmonic oscillator can be described by the Hamiltonian [113]

$$H = \frac{P^2}{2m} + \frac{1}{2}m\omega^2 X^2, \tag{5.36}$$

where X and P are the position and momentum operators, respectively. A useful tool to determine the energy eigenstates of the system are the so-called ladder operators

$$a = \sqrt{\frac{m\omega}{2\hbar}}\left(X + \frac{i}{m\omega}P\right) \tag{5.37}$$

and

$$a^\dagger = \sqrt{\frac{m\omega}{2\hbar}}\left(X - \frac{i}{m\omega}P\right). \tag{5.38}$$

With these operators the Hamiltonian can be rewritten as

$$H = \hbar\omega\left(a^\dagger a + \frac{1}{2}\right). \tag{5.39}$$

This shows that the energy of the system is quantized in units of $\hbar\omega$ and has a zero-point energy $\hbar\omega/2$.

$$N = a^\dagger a \tag{5.40}$$

is also known as the number operator since it returns the number of energy quanta of an energy eigenstate $|n\rangle$. Applying the ladder operators on an energy eigenstate gives

$$a^\dagger|n\rangle = \sqrt{n+1}\,|n+1\rangle \tag{5.41}$$

$$a|n\rangle = \sqrt{n}\,|n-1\rangle. \tag{5.42}$$

Hence, a removes a quanta from the state, while $a^\dagger$ adds a quanta.

Furthermore, the position and momentum operators can be expressed as

$$X = \sqrt{\frac{\hbar}{2m\omega}}(a^\dagger + a) \tag{5.43}$$

$$P = i\sqrt{\frac{m\omega\hbar}{2}}(a^\dagger - a) \tag{5.44}$$

using the ladder operators. The prefactor

$$x_{\mathrm{ZPF}} = \sqrt{\frac{\hbar}{2m\omega}} \tag{5.45}$$

in the position operator is the zero-point fluctuation (or motion) of the harmonic oscillator. It corresponds to the amplitude caused by the zero-point energy $\hbar\omega/2$.

Coupled harmonic oscillators

A system of coupled identical harmonic oscillators is described by the Hamiltonian [113, 42]

$$H = \hbar\omega \sum_i a_i^\dagger a_i + \frac{\hbar}{2} \sum_{i,j} \tilde{g}_{ij}(a_i^\dagger + a_i)(a_j^\dagger + a_j), \tag{5.46}$$

where ω is the resonance frequency of an individual oscillator and $\tilde{g}_{ij}$ are the coupling constants between the oscillators. By choosing the right basis, the Hamiltonian can be diagonalized into the form [113, 42]

$$H = \sum_n \hbar\omega_n a_n^\dagger a_n. \tag{5.47}$$

Hence, the coupled system can be viewed as a system of decoupled harmonic oscillators with the resonance frequencies ω_n and the respective ladder operators $a_n^\dagger$ and a_n.

5.3 Materials and methods

5.3.1 Diamond sample

Fig 5.9a shows optical microscopy images of a typical diamond sample used in the experiments presented in this chapter. The sample is a 2-5µm thin diamond membrane holding multiple cantilever pairs, varying in length, width and cantilever distance. The membrane is glued onto a bulk diamond with a hole. This provides robustness to the sample, while ensuring free motion of the cantilevers. The sample contains a random distribution of near-surface NV

centers produced by ion-implantation. A confocal image of the embedded NVs (right) is shown in Fig 5.9b, next to a scanning electron microscope (SEM) image of a cantilever pair (left).

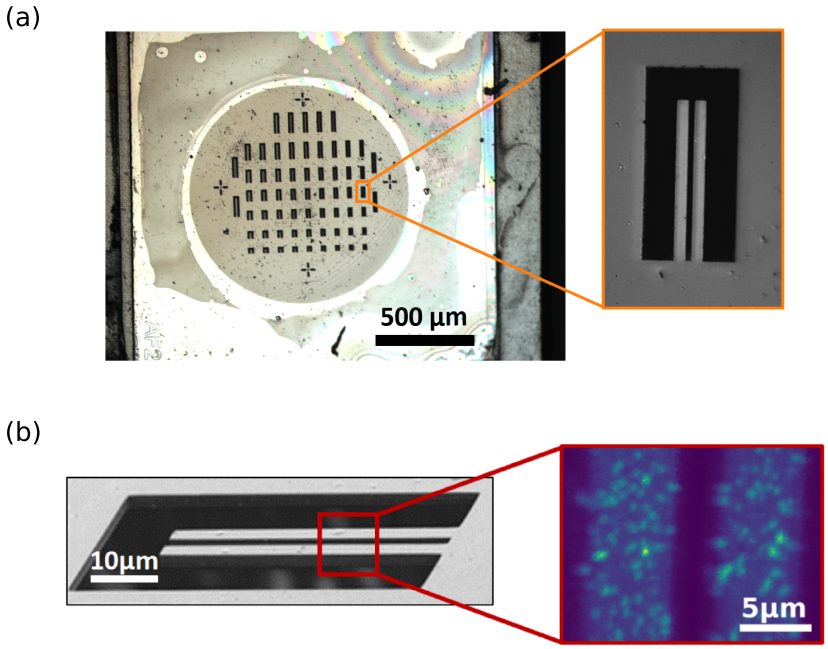

Figure 5.9: **(a)** Optical microscopy images of a typical cantilever pair sample. A 2-5µm thin diamond membrane holds cantilever pairs of different length, width and distance. **(b)** Scanning electron microscopy (SEM) image of a cantilever pair (left). Confocal image of the embedded NVs (right).

The sample is fabricated from an ultrapure single crystalline diamond membrane provided by Element Six and Delaware Diamond Knives (DDK). The initial 2x2 mm membrane has a thickness of ~30 µm. In a first step, the shallow NV centers are created by ion implantation of ^{15}N at 10 keV and subsequent annealing at 950°C for 2 h in a high vacuum (Fig 5.10a). Afterwards, the mechanical structures are created. All steps during this process are performed on the non-implanted side of the sample. First, a circular region (~1mm diameter) of the membrane is thinned down to ~2-4 µm. As an etching mask, a bulk

diamond with an according hole in the center is glued on top of the diamond membrane. The membrane is then thinned down by Ar/SF_6 RIE-ICP etching (Fig 5.10b). Afterwards, the bulk diamond is removed (Fig 5.10c) and a layer of PMMA is spin-coated onto the sample. The area around the cantilevers, that later will be etched through the diamond, is defined by electron beam lithography on the PMMA layer (Fig 5.10d). After development of the PMMA, only this area is left covered by the PMMA layer (Fig 5.10e). Afterwards, a 10 nm layer of chromium and a 150 nm layer of titanium are deposited on the sample by electron gun evaporation (Fig 5.10f). The remaining PMMA is lifted off by acetone, removing the metal layer in this area. The titanium acts as a mask during the subsequent O_2 RIE-ICP etching (Fig 5.10g). This etching process is used to remove all diamond material between the cantilevers and concludes the fabrication process (Fig 5.10e). The titanium layer is not removed from the sample as it enables the photo-thermal driving of the diamond cantilevers as described in Section 5.4.4.

5.4 Characterizing the mechanical system

Utilizing a cantilever pair in a spin-mechanical hybrid system requires knowledge of its mechanical properties. In this section, the methods used to characterize cantilever pairs are presented. As an example, experimental data measured on a typical cantilever pair is used. All mechanical parameters presented in this section belong to this specific cantilever pair.

5.4.1 Mode localization and identification

To localize the mechanical modes of the system, it was mechanically excited using a piezoelectric actuator that is glued onto the sample holder. The resulting cantilever motion was then measured by a purely optical readout method. The target cantilever was illuminated continuously by a focused 532 nm laser and the reflected light was collected by an APD. Fig 5.11a shows the photon count rate dependence on the objective z-position. Positioning the focus of the laser beam slightly above the diamond surface (orange line in Fig 5.11a) leads to a linear photon count rate change for small changes of the sample z-position

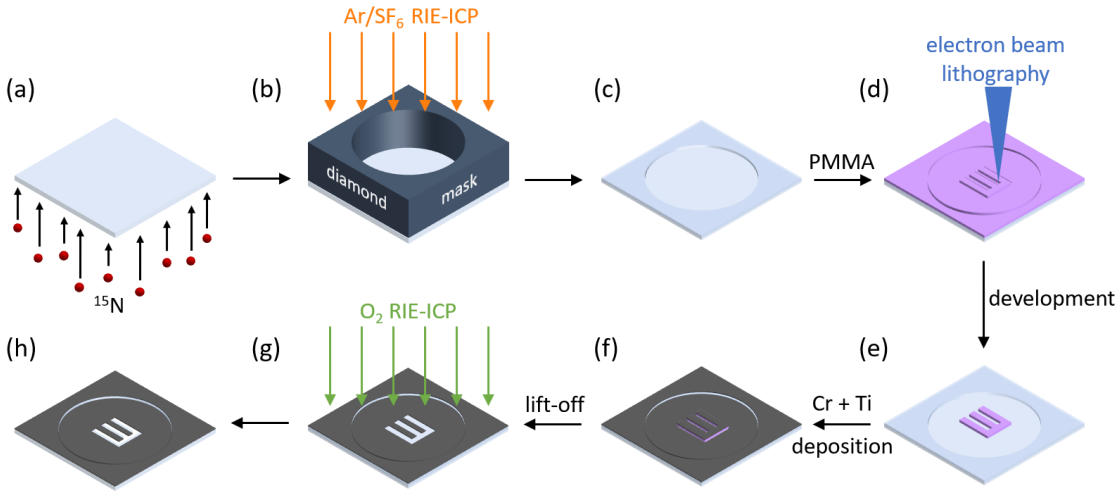

Figure 5.10: Fabrication process of the diamond cantilever sample. **(a)** The sample is fabricated from a ~30 µm thick diamond membrane. Shallow NV centers are created by ^{15}N ion-implantation at 10 keV. **(b)** A circular region in the center of the membrane is thinned down to ~3 µm by Ar/SF_6 RIE-ICP etching. A bulk diamond with an according hole is used as an etching mask. **(c)** Membrane with thin central area after removal of the diamond mask. **(d)** The mechanical structure is defined by electron beam lithography on a spin-coated layer of PMMA. **(e)** After development of the PMMA layer, PMMA is only left in the area around the cantilevers. **(f)** 10 nm of chromium and 150 nm of titanium are deposited on the membrane. **(g)** After the remaining PMMA is removed using acetone, only the area between the cantilever is exposed to the subsequent O_2 RIE-ICP etching. This etching process removes all the diamond material between the cantilevers. **(h)** Illustration of the final diamond sample. The titanium layer is kept on the sample to enhance the photo-thermal driving of the cantilevers.

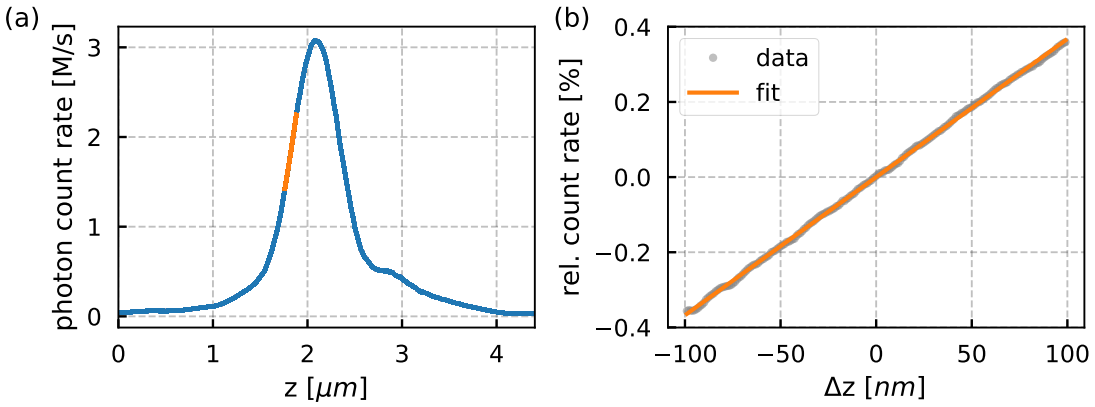

Figure 5.11: Z-profile of the photon count rate. **(a)** The profile shows the two surfaces of the diamond sample with differing reflectances. Around the highest slope of the photon count rate distribution, the z-dependence of the count rate is approximately linear (orange line). **(b)** Linear z-dependence of the photon count rate when the laser is focused slightly above the sample surface. The slope of the count rate enables a quantitative optical measurement of the cantilever z-position.

(< 100 nm). The linear slope of the photon count rate is depicted in Fig 5.11b. A displacement of the cantilever can then be directly measured as a change of the photon count rate. By time-correlating the collected photons to the cantilever drive signal, the cantilever oscillation is recorded as an oscillation of the measured photon count rate ν_{ph}. This measurement yields the amplitude, frequency and relative phase of the cantilever motion. Fig 5.12a shows an example of a typical photon count rate map. By calculating the variance of the photon time trace $\mathrm{Var}(\nu_{\mathrm{ph}})$ for every excitation frequency, a frequency spectrum of the system can be obtained (see Fig 5.12d).

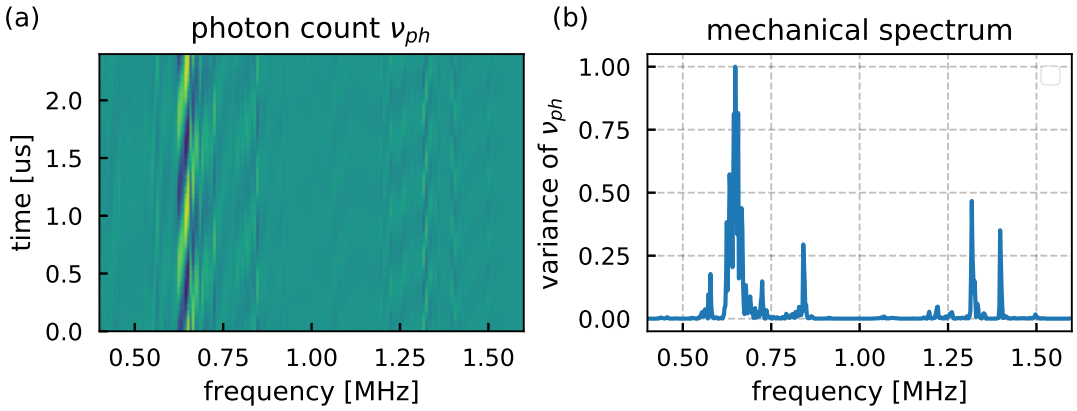

Figure 5.12: **(a)** Photon count rate ν_{ph} measured on a cantilever pair at different drive frequencies. For each frequency, the photons are collected time-correlated to the drive signal. As a result, mechanical oscillations can be observed as oscillations of the photon count rate. **(b)** Mechanical spectrum obtained by calculating the variance of the photon count rate $\mathrm{Var}(\nu_{\mathrm{ph}})$ for each drive frequency.

The spectrum shows multiple signals at various frequencies, each corresponding to a specific vibrational mode of the sample. The complex mechanical structure of the sample, composed of a thin membrane and multiple smaller mechanical structures, results in an equally complex vibrational behavior. Nevertheless, most observed modes can be categorized into two main classes - membrane modes and cantilever modes. While membrane modes stretch over the whole sample, cantilever modes are mostly localized to a specific cantilever

pair. As an example, Fig Fig 5.13 shows multiple mechanical modes of a thin circular membrane holding a single cantilever pair. The vibrational modes were simulated using a commercial finite-element simulation software (COMSOL). 5.13a displays a membrane mode that extends over the whole membrane. In contrast, the modes shown in Fig 5.13b,c are the two vertical cantilever modes, localized to the cantilever pair. For this work, only vertical cantilever modes are of interest, thus the identification and characterization of the observed modes is necessary.

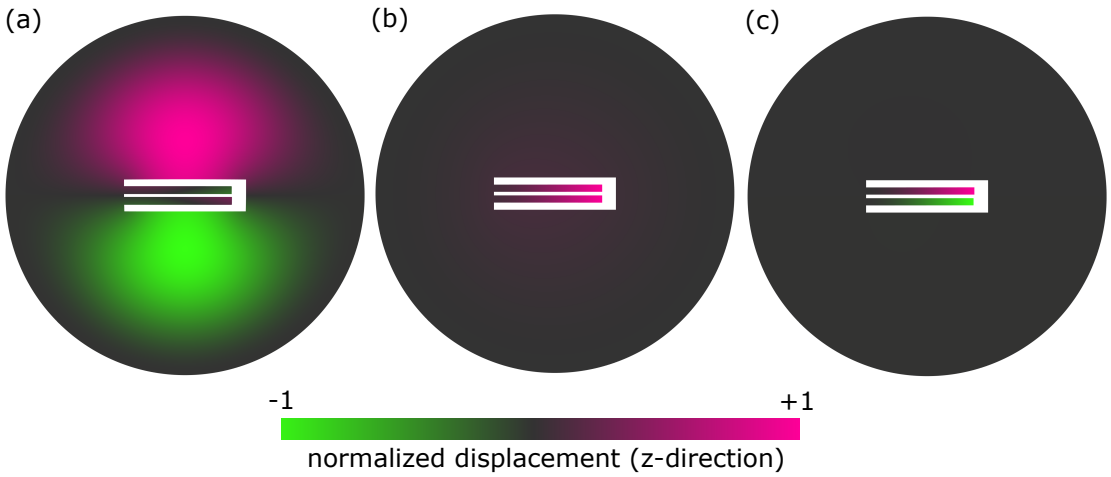

Figure 5.13: Finite-element simulation (COMSOL) of a thin diamond membrane holding a cantilever pair. **(a)** Membrane mode extending over the whole sample. **(b)** Fundamental symmetric cantilever mode. **(c)** Fundamental anti-symmetric cantilever mode.

To identify the modes, the exact vibrational motion and deformation of the sample has to be known. For this purpose, the mechanical excitation frequency is fixed to the resonance frequency of interest, while the laser focus is scanned laterally and vertically to the sample surface. For each position, a photon time trace is measured. The resulting dataset can be interpreted as confocal slices through the sample for each time step. This allows to track the sample position and shape for each phase of the drive signal. To visualize the sample motion over time, it is convenient to transform the photon count distribution along the z-axis into an actual z-position of the sample. This can be done by calculating the center of mass of the photon count data along the z-axis for each x- (or

y-) and time bin. The data can then be plotted as the time-evolution of the z-displacement of a line along the sample. For an unambiguous identification of the cantilever modes, scans along two perpendicular directions are required. Fig 5.14c-e shows scans perpendicular to the cantilever (along the green line in Fig 5.14a) for three different resonance frequencies - 0.84 MHz, 1.346 MHz and 1.426 MHz. At a drive frequency of 0.84 MHz, not only the cantilevers but also the rest of the membrane is oscillating (see Fig 5.14c). In contrast, for 1.31 MHz and 1.39 MHz, the membrane is not vibrating while the cantilevers oscillate in a symmetric (Fig 5.14b, 1.31 MHz) and anti-symmetric (Fig 5.14c, 1.39 MHz) fashion. From this, one can deduce that $\omega_1 = 2\pi \times 1.31$ MHz and $\omega_2 = 2\pi \times 1.39$ MHz are the frequencies of two vertical common modes of the cantilever pair. Fig 5.14b shows a scan along one of the cantilevers (pink line in Fig 5.14a) while the symmetric vertical cantilever mode is excited. The revealed shape of the vibrational mode proves that the observed cantilever modes are ground modes. In the following, only vertical ground modes will be used. Therefore, they will be from now on referred to simply as mechanical modes of the system. The lower (higher) frequency mode will be referred to as the symmetric (anti-symmetric) mode.

Fig 5.15c shows oscillation spectra of both cantilevers, each showing the two mechanical modes. The frequencies of the modes are $\omega_1 = 2\pi \times (1.346 \pm 0.008)$ MHz and $\omega_2 = 2\pi \times (1.426 \pm 0.001)$ MHz. The quality factor can be determined to be $Q = 1768 \pm 8$ from the width of the anti-symmetric mode (see Eq. (5.26)). The corresponding photon count data is displayed in Fig 5.15a,b. The relative amplitude difference between the two modes varies between the cantilevers. This can be explained by a possible fabrication imperfection that leads to parameter differences between the two cantilevers. These imbalances result in a partial localization of the common modes, which causes a change of the relative mode amplitudes. Cantilever imbalances and mode localization are discussed in more detail in Section 5.7.

Comparing the photon histograms of both cantilevers, measured at the two resonance frequencies (ω_1 in Fig 5.15d and ω_2 in Fig 5.15e), directly shows the symmetric and anti-symmetric behavior of the common modes.

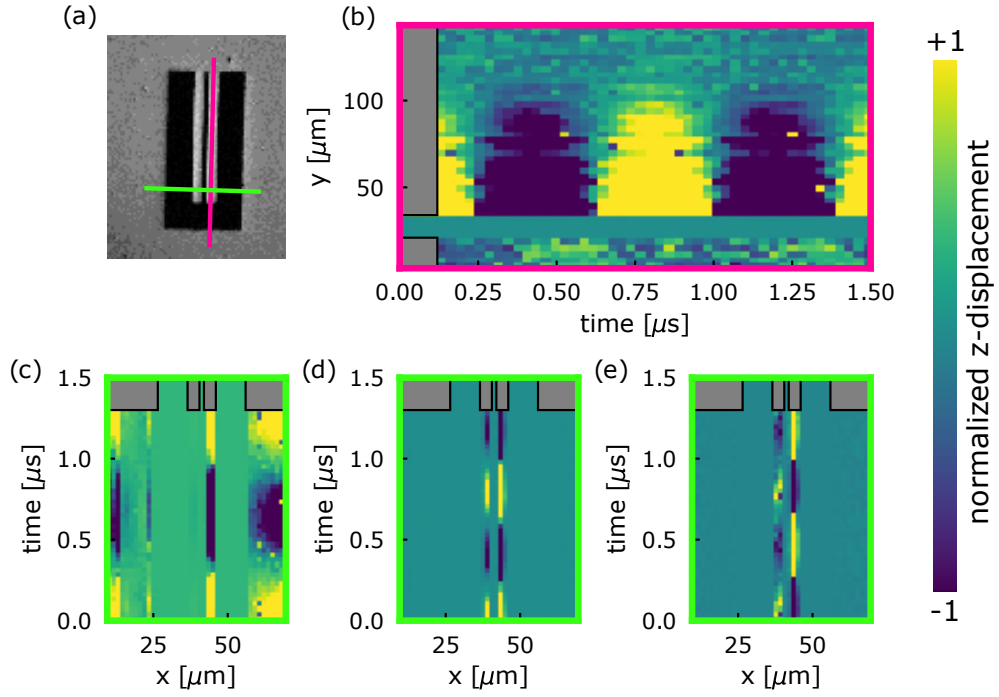

Figure 5.14: Time-dependent z-displacement of the sample while it is mechanically excited. The displacement is measured optically for different lateral positions of the readout laser. **(a)** SEM image of the cantilever pair. The green and pink lines indicate the different positions of the readout laser focus. **(b)** Z-displacement along the cantilever (pink line in (a)) while driven at the symmetric cantilever mode. The deflection profile along the y-axis shows that a fundamental mode is observed. **(c-e)** Z-displacement perpendicular to the cantilever (green line in (a)) for three different driving frequencies. As the membrane in (c) is oscillating, this drive frequency corresponds to a membrane mode. The data shown in (c) and (d) corresponds to the symmetric and anti-symmetric cantilever mode, respectively.

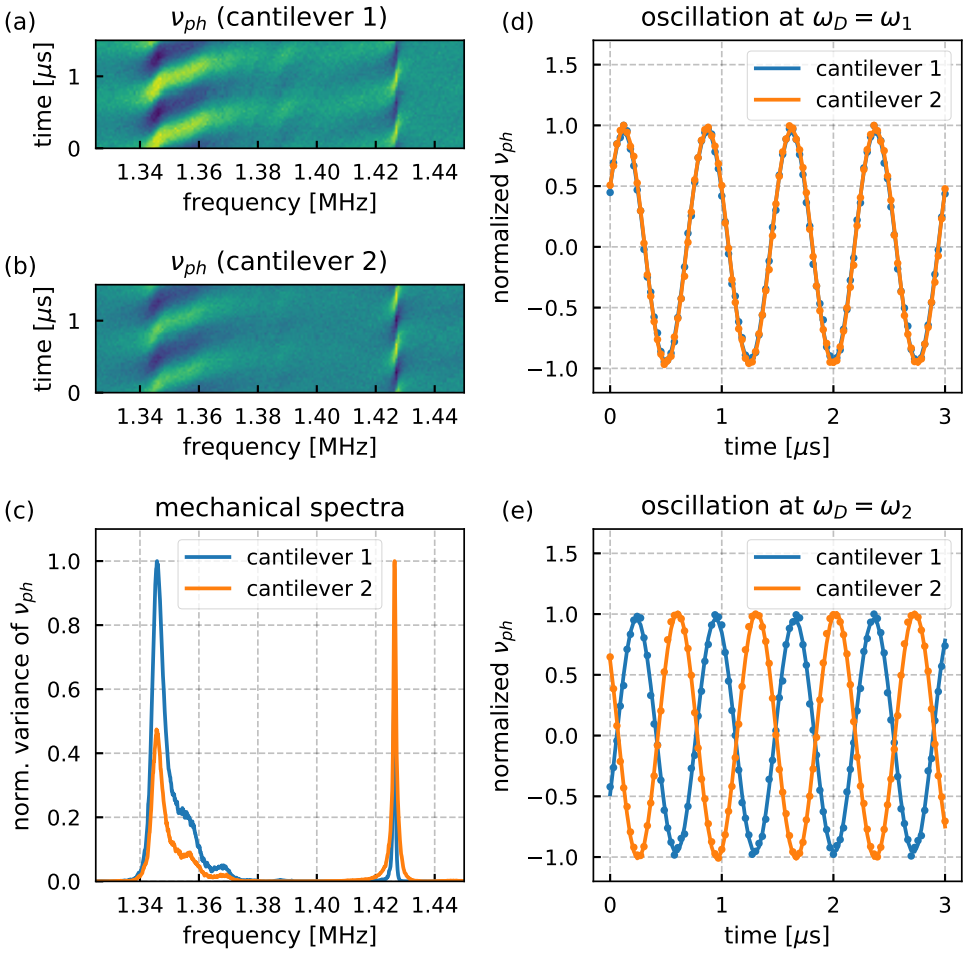

Figure 5.15: **(a,b)** Time-dependent photon count rate ν_{ph} measured at different mechanical drive frequencies. The photon count rate was recorded consecutively with the readout laser focused on cantilever 1 (a) and cantilever 2 (b). **(c)** Mechanical spectra of both cantilevers generated by calculating the variance of the photon count rate $\mathrm{Var}(\nu_{\mathrm{ph}})$ for each drive frequency. **(d,e)** Photon count histogram recorded on the two cantilevers at the symmetric mode with frequency ω_1 (d) and at the anti-symmetric mode with frequency ω_2 (e).

5.4.2 Parameters of the mechanical system

From the mechanical frequency spectrum, several system parameters can be deduced. In the following, the mechanical properties of the sample will be determined.

Quality factor

The quality factor can be determined by the ratio between resonance frequency and the width of the resonance peak (see Eq. (5.26)). Fig 5.16a shows a typical resonance peak at ambient conditions. For this specific cantilever pair, the measured quality factor is $Q_{\text{ambient}} = 1768 \pm 8$. The quality factors of the mechanical resonators investigated in this thesis vary between 500 and 2000 under ambient conditions. At low temperature and ultra-high vacuum the quality factor increases dramatically [47, 48]. A resonance peak acquired at a temperature of $T = 4.8$ K and a pressure of $P = 2{\times}10^{-9}$ mbar is shown in Fig 5.16b. As expected, the peak is narrower, but at the same time, it is not following a Lorentzian function anymore. This modulation originates from the finite frequency width of the piezo-actuated drive. To measure the quality factor independent of the specific drive mechanism, the ringdown of the free cantilever can be recorded. For this purpose, an oscillation of the cantilever is first excited using a piezo-actuator. Afterwards, the drive is turned of and the amplitude of the oscillation is measured over time. From the exponential decay of the amplitude, the quality factor can be determined using Eq. (5.19). A ringdown, measured at low temperature and ultra-high vacuum, can be seen in Fig 5.16c. The observed cantilever exhibits a quality factor of $Q_{\text{LT,UHV}} = (0.374 \pm 0.008) \times 10^6$. This corresponds to an improvement over ambient conditions of $\approx 10^3$.

Sample thickness

The dimensions of the mechanical resonators need to be known. While the width and length of the cantilevers are well defined by the used etching mask, knowledge of the sample thickness is limited. However, the thickness can be determined using the observed resonance frequencies. From Eq. (5.10), we can

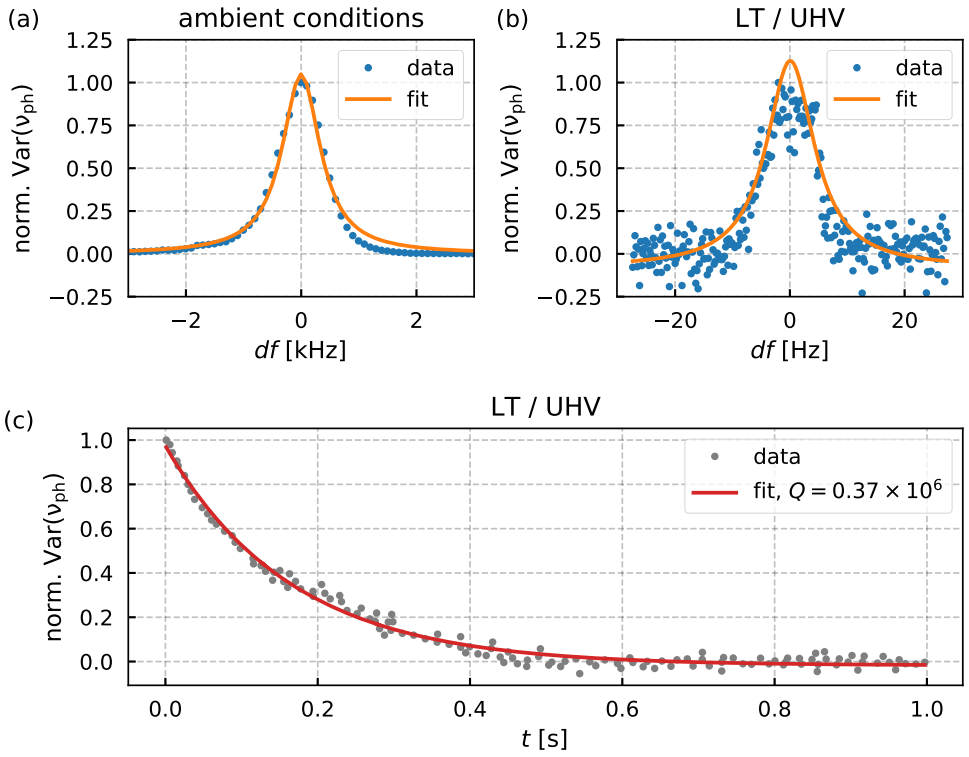

Figure 5.16: **(a)** Resonance peak of a mechanical mode under ambient conditions. From the fitted curve (orange) a quality factor of $Q_{ambient} = 1768 \pm 8$ can be deduced. **(b)** Resonance peak at low temperature ($T = 4$ K) and ultra-low vaccum ($P = 2 \times 10^{-9}$ mbar). The shape and width of the peak is distorted by the imperfect driving. **(c)** Free amplitude decay of a previously excited cantilever at low temperature and ultra-high vacuum. From the fitted exponential decay (red), the quality factor can be determined independent of the driving mechanism. The measured quality factor is $Q_{LT,UHV} = (0.374 \pm 0.008) \times 10^6$. This is an improvement by a factor of $\approx 10^3$ compared to ambient conditions.

get an expression for the cantilever thickness

$$T = \omega_1 \left(\frac{L}{1.87}\right)^2 \sqrt{\frac{12\rho}{E}}. \tag{5.48}$$

With length $L = 100 \pm 1\,\mu$m and the measured mode frequencies, we get a sample thickness of $T = 4.84 \pm 0.21\,\mu$m. Note, that although this equation was derived for a single cantilever, finite-element simulations (COMSOL) show that the frequency of the first mode barely changes with the number of coupled cantilevers (see Fig 5.7a).

Spring constants k and k'

From Eq. (5.29) the expressions $k = m_{\text{eff}} = m\omega_1^2$ and $k' = \frac{m_{\text{eff}}}{2}(\omega_2^2 - \omega_1^2)$ for the spring constants can be derived. Using Eq. (5.35) as an approximation for the effective mass of the cantilever array, the spring constants can be written as

$$k = \frac{N}{4}\rho LWT\omega_1^2 \tag{5.49}$$

and

$$k' = \frac{N}{8}\rho LWT(\omega_2^2 - \omega_1^2), \tag{5.50}$$

where $N = 2$ is the number of cantilevers. For the investigated cantilever pair the values $k = 150 \pm 20$ N/m and $k' = 9.2 \pm 1.2$ N/m are obtained.

5.4.3 Mechanical susceptibility

Mechanically driving the cantilevers with a piezoelectric actuator allows for well-controlled and reproducible excitation of mechanical oscillations. This is crucial for the quantitative measurement of the spin-phonon coupling. Furthermore, the piezo-based excitation is used as a reference for the characterization of the photo-thermal driving presented in Section 5.4.4. Therefore, it is important to determine the mechanical susceptibility χ_m. This is achieved by quantitatively measuring the oscillation amplitude a_0 for varying piezo-voltage amplitudes V_0. The measurement of the oscillation amplitude is performed using the optical readout technique introduced in Section 5.4.1. Photon count rate oscillations, resulting from different driving voltages are shown in Fig 5.17a. The

photon count rate amplitudes can be translated into actual mechanical oscillation amplitudes using the relative photon count rate change over the z-position shown in Fig 5.11b. Fig 5.17b shows the amplitude response of a specific cantilever pair to a varying driving voltage. The slope of the amplitude change represents the mechanical susceptibility of the investigated system. Repeating the same procedure multiple times for the same mechanical resonator pair, shows that the values obtained for χ_m vary more than the error of each individual measurement (see Fig 5.17c). This most likely is caused by drifts of the laser focus position during the measurements. The average and distribution of the individual values yield a mechanical susceptibility of $\chi_m = 11.80 \pm 0.1$ nm/V.

5.4.4 Photo-thermal driving of cantilevers

Optical driving, damping and amplification of cantilever systems based on photo-thermal heating[114, 115, 116, 117] and radiation pressure[118] was already successfully demonstrated. In this section, the working principle and experimental demonstration of photo-thermal driving of diamond cantilevers are discussed. Photo-thermal driving relies on the periodic heating of a single cantilever by a focused laser beam. In contrast to piezo-actuated driving, the forces of this method only act on a single cantilever in the array. Thus, this interaction can be considered as a driving mechanism localized to a single resonator. This enables new possibilities to investigate the behavior of the coupled resonator system. While manipulating a specific cantilever, the effects of this interactions on distant cantilevers or spins can be investigated. This way the cantilever-cantilever coupling can be directly observed and characterized. In this scenario, the photo-thermally induced forces can be understood as an emulation of forces interesting in future experiments, like e.g. the magnetic forces on a cantilever by an embedded electron spin.

Furthermore, utilizing a localized photo-thermal force removes spurious membrane modes and horizontal cantilever modes from the mechanical spectrum of the cantilever pair, making localization of the out-of-plane vibrational cantilever modes easier.

Further potential applications are tuning of single cantilevers in an array or parametric amplification of cantilever oscillations.

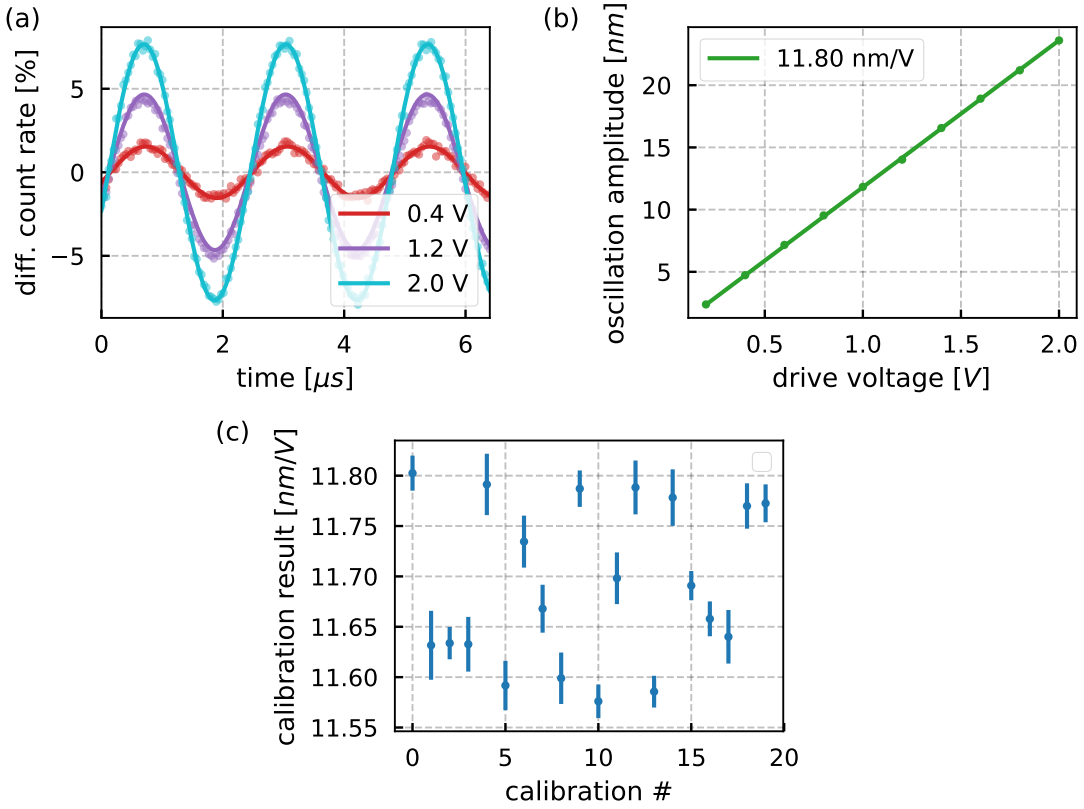

Figure 5.17: **(a)** Oscillations of the photon count rate resulting from different drive voltages. **(b)** Amplitude of the mechanical motion for different drive voltages. The amplitude increases linearly with the drive voltage. The slope corresponds to the mechanical susceptibility χ_m. **(c)** Results of consecutive measurements of the mechanical susceptibility. The deviation of the acquired values is higher than the error of the individual measurements. This is caused by drifts and instabilities of the system during the measurements.

Working principle

Photo-thermal driving relies on the localized heating of a resonator by absorption of photons. The resulting temperature gradients will lead to a bending of the cantilever. If this heating process is repeated periodically, the bending forces can drive oscillations of the cantilever. This method was already demonstrated for bare silicon AFM cantilevers[116, 115]. For pure diamond cantilevers, this process is ineffective as they exhibit low absorption and high thermal conductivity, and thereby small temperature gradients. However, the photo-thermal driving efficiency can be strongly increased by depositing a layer of a different material onto the diamond surface. The coating, on one hand, can increase the absorption of the system. On the other hand, the difference of thermal expansion coefficients of the materials will lead to a stronger bending of the cantilever.

Experimental realization

To enhance the photo-thermal excitation process, the diamond cantilevers are coated with a 200 nm layer of titanium. To generate the photo-thermal heating, a home-built IR diode laser with a wavelength of 850 nm and a maximum optical output power of 200 mW was used. To enable optical readout and excitation at two separate positions on the sample, the IR laser was implemented in a way that it can be scanned relative to the 532nm readout laser. The lateral position of the laser focus is changed by varying the inclination angle of the beam into the objective. At the same time, it needs to be ensured that the beam enters the objective always at the center of the back aperture. This is achieved by sending the IR beam through a so-called 4f-setup, consisting of a two-axis galvo scanner (Thorlabs GVS212/M), two concave mirrors (Thorlabs CM750-500-P01) and the objective. An illustration of the optical setup is shown in Fig 5.18. To improve the readability of the illustration, the mirrors are replaced by convex lenses. The beam first passes the galvo scanner and is deflected away from the optical axis by some angle. The galvo scanner is positioned in the focal point of the first concave mirror. Thus, after passing the first mirror, the beam is parallel to the optical axis but has an offset that depends on the galvo scanner angle. The second concave mirror will reflect the beam into the back aperture

of the objective. As the focal points of the two concave mirrors coincide, the beam will be collimated after passing the second mirror. The IR laser beam is reflected onto the optical axis of the green laser by a dichroic mirror (805nm shortpass, Thorlabs DMSP805) positioned between lense 2 and the objective.

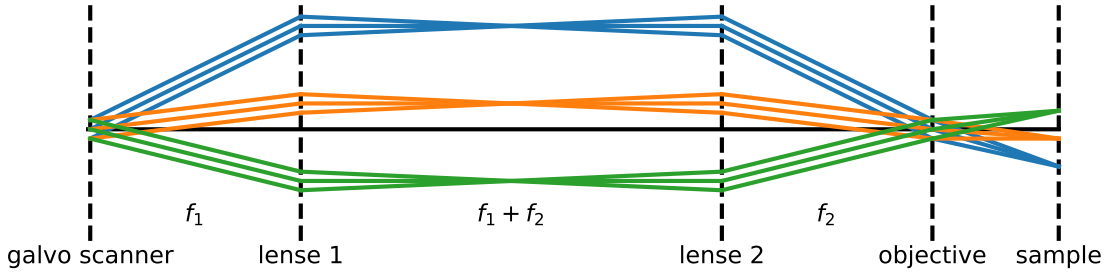

Figure 5.18: Optical paths through the 4f setup for 3 different deflection angles of the galvo scanner. The lenses ensure that the beam will enter the objective in the center of the back aperture of the objective independent of the angle at the galvo scanner. Additionally, the beams will be parallel again after lense 2, as the focal points of the two lenses coincide. Because of the different inclination angles into the objective, the lateral position of the laser focus on the sample will change. Thus, by scanning the deflection angle of the galvo scanner, the beam focus is scanned along the sample surface.

Periodic driving

IR laser pulses with a repetition rate ω_d and a duty cycle of 0.5 are used to excite oscillations of the cantilever system. Fig 5.19a shows the time-resolved photon counts ν_{ph} for different drive frequencies (the optical readout is described in greater detail in Section 5.4.1). Although, only one cantilever is directly exposed to the driving mechanism, both modes of the cantilever pair are visible in the spectrum shown in Fig 5.19b. This demonstrates that the optical drive is exciting the common modes of the coupled cantilever pair. Comparing the phase of the photon count signal for the two resonance frequencies reveals the symmetric and anti-symmetric behavior of the two modes (see Fig 5.19c,d).

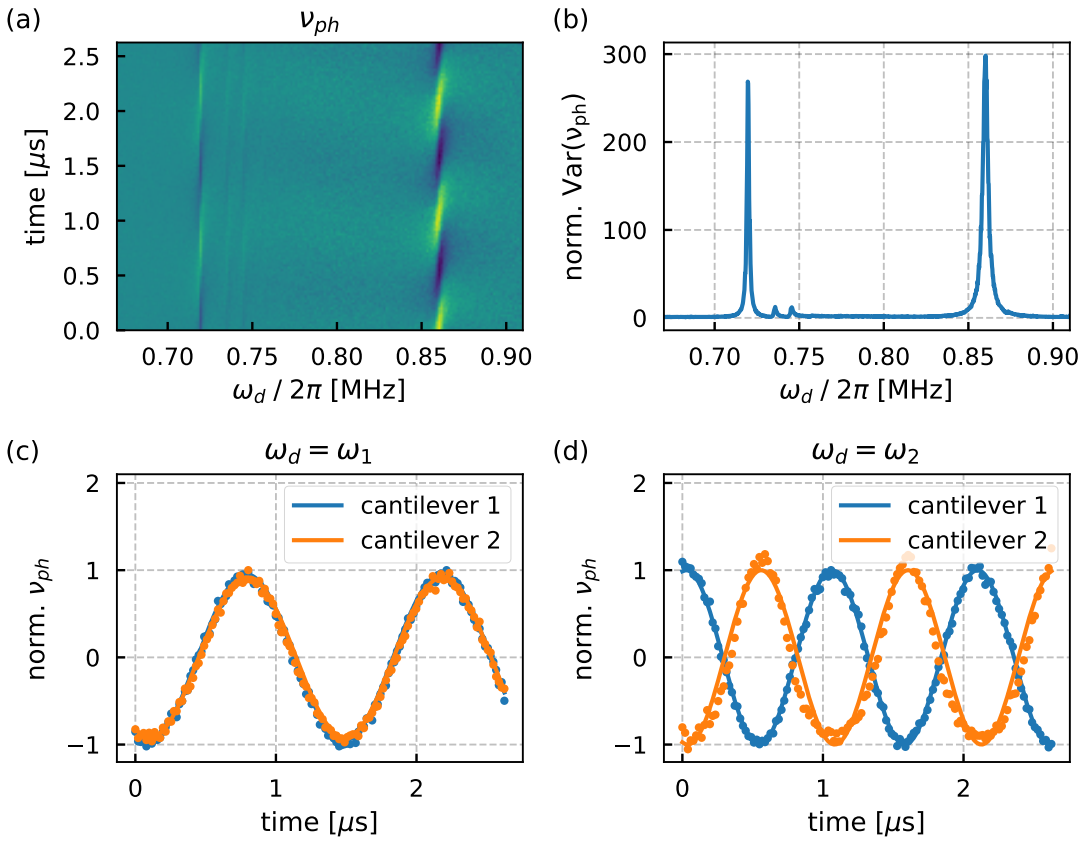

Figure 5.19: **(a)** Time-correlated photon counts ν_{ph} from a cantilever in a cantilever pair for different repetition rates ω_d of the IR laser. **(b)** Mechanical spectrum of a cantilever pair generated by calculating the normalized variance of ν_{ph} for each drive frequency. **(c,d)** Histograms of the photon count of both cantilevers while the system is photo-thermally driven at the symmetric mode **(c)** and the anti-symmetric mode **(d)**

So far, optical driving of mechanical modes was demonstrated. However, the physical process that translates the incoming photons into an actual force, acting onto the cantilever, was not experimentally determined. Instead of a photothermal process, the cantilevers could also be actuated by radiation pressure. In the following, two experimental observations, ruling out a radiation pressure dominated driving mechanism, are discussed. By fitting a function of the form $f(t) = a_0 sin(\omega t + \phi_0 + d\phi)$ to each photon histogram, the relative phase of the cantilever oscillation for each driving frequency can be obtained. Here, ϕ_0 is the constant delay between the drive signal and the start of the measurement. The change of the relative phase $d\phi$ at both resonances is shown in Fig 5.20. The observed phase signal resembles the phase behavior expected for a harmonic oscillator excited by a periodic displacement as shown in Fig 5.3e. The same phase change is observed when exciting the sample with a piezo-actuator (see Fig 5.12a,b). If the system instead would be driven by an external force, like e.g. radiation pressure, the sign of the phase change would be different as shown in Fig 5.3c. As comparison, a resonance peak resulting from a radiation pressure based drive of a cantilever can be seen in the work of Ma et al. [119].

Further insight into the driving mechanism can be gained by investigating the direction of the driving force. For this purpose, a cantilever was resonantly excited using the optical drive and the resulting oscillation was detected optically. Afterwards, the sample was flipped and the measurement repeated. Radiation pressure always acts into the direction of the laser beam, thus, flipping the sample will not change the measurement result. The direction of the force generated by photon-induced heating, on the other hand, is defined by the position of titanium coating. Therefore, flipping the sample will also flip the direction of the driving force (see Fig 5.21a). This change of the force direction is observed in the measurement as a change of the sign of the cantilever oscillation (see Fig 5.21b). This strongly indicates that photo-thermal heating is the dominant driving process.

Static bending

The photo-thermal heating can also be used to create a static bending of a cantilever. To demonstrate this, a cantilever was exposed to long, far off-resonant,

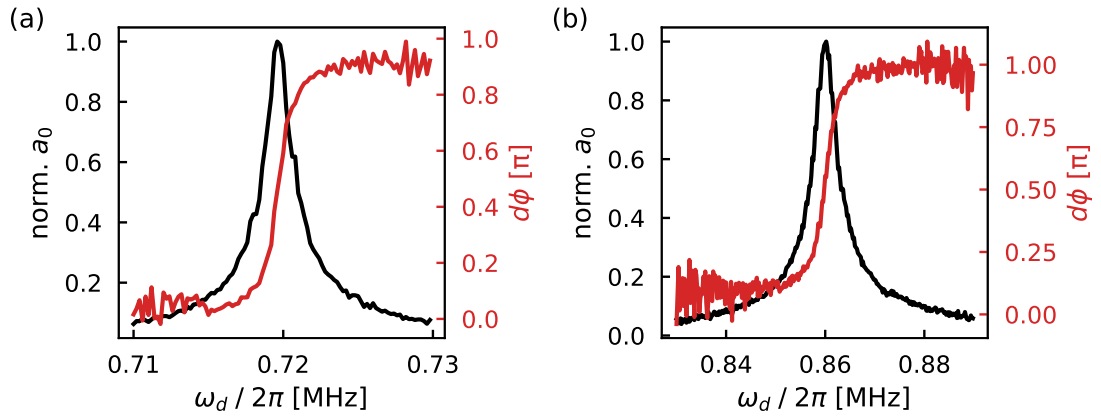

Figure 5.20: Mechanical resonances of the cantilever pair. The amplitude (black) and phase (red) of the cantilever oscillation is measured optically. The observed phase signal resembles the phase behavior of a harmonic oscillator excited by a periodic displacement (instead of an external force). This rules out radiation pressure as the dominant driving mechanism. **(a)** Resonance peak of the symmetric mode. **(b)** Resonance peak of the anti-symmetric mode.

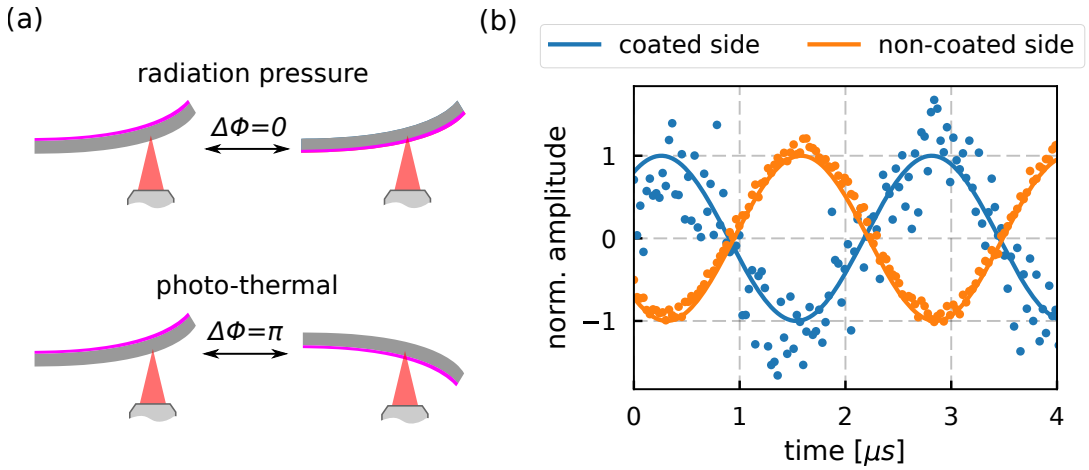

Figure 5.21: **(a)** Illustration of the experimental scheme to investigate the direction of the force associated with the optical driving. The oscillation resulting from a resonant optical drive is recorded. Afterwards, the sample is flipped and the same measurement is repeated. If radiation pressure is the dominant force, the measured signal would not change, as the direction of the force is independent of the sample. In contrast, if photo-thermally induced bending is the dominant process, the sign of the oscillation will change, as the direction of the force is determined by the relative position of the titanium layer. **(b)** The oscillation changes when flipping the sample, indicating that photo-thermal heating is the dominant driving mechanism.

laser pulses while optically measuring the deflection in z-direction. Before the measurement, the z position dependence of the photon count rate was calibrated, allowing a quantitative readout of the cantilever deflection (see Section 5.4.3). The response of the cantilever to the heating is displayed in Fig 5.22a. The blue markers are the measured data points, while the orange line represents a simulation of the cantilever bending. The simulation consists of two steps. First, the temperature distribution along the cantilever for each time step is simulated based on Fourier's law. In a second step, the temperature distributions are translated into a bending of the cantilever.

For the simulation of the temperature distribution, only the diamond layer is taken into account. As the titanium layer is much thinner and has a lower heat conductivity, its effect onto the heat flow along the cantilever is neglectable. The cantilever is separated into n segments of length l (thus $L = nl$). At the first time step, all segments are at the lab temperature $T_{\mathrm{lab}} = 300$ K. Afterwards, for every time interval dt, the heat dQ flowing between neighboring segments is calculated using Fourier's law

$$dQ = \frac{A(T_i - T_{i+1})\lambda}{l} dt. \tag{5.51}$$

Here, A is the cross-sectional surface area, T_i is the temperature of the i-th segment and λ is the thermal conductivity. Subsequently, the total heat accumulated in each segment Q_i is used to calculate the new temperature distribution along the segments using the expression

$$T_i = \frac{Q_i}{c\rho l A}, \tag{5.52}$$

where c is the specific heat capacity of diamond at ambient conditions and $\rho = 3.5 \times 10^3$ kg m^{-3} is the density of diamond. Due to the large dimensions of the diamond membrane and the exceptionally high heat conductivity of diamond, the clamping point is approximated to be a perfect heat sink by fixing the temperature of the first segment to $T = T_{\mathrm{lab}} = \mathrm{const}$. Additionally, the photo-thermal heating is introduced by adding a specific amount of heat per time interval to segments exposed to the laser beam. The heat generated along the segments is modeled as a Gaussian distribution with a total power P and a FWHM of 2 μm. The simulated temperature distributions for different moments in time are shown in Fig 5.22b,c.

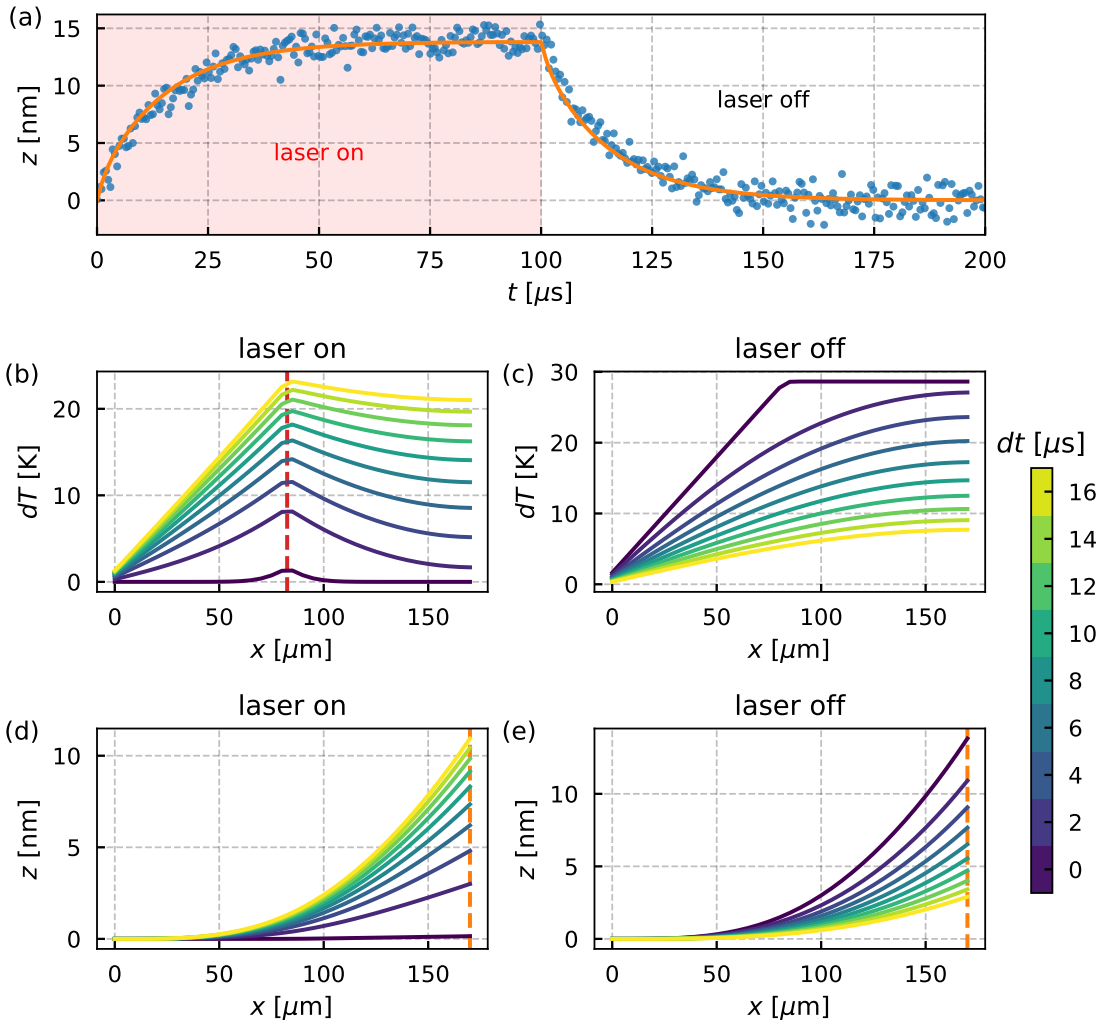

Figure 5.22: **(a)** Response of a cantilever to long off-resonant laser pulses. The blue markers are measured data points. The orange line is a simulation of the cantilever bending due to photo-thermal heating. **(b)** Simulated temperature distributions at different times during the photo-thermal heating. **(c)** Simulated temperature distributions while the cantilever is cooling down after the laser pulse ended. **(d)** Numerically calculated bending of the cantilever resulting from the temperature distributions shown in (b). **(e)** Numerically calculated bending of the cantilever resulting from the temperature distributions shown in (c).

For a cantilever composed of two layers of different materials, the bending $z(x)$ resulting from a certain temperature distribution $dT(x)$ can be numerically calculated using the following differential equation $dT(x)$[114]

$$\frac{d^2z}{dx^2} = 6(\gamma_2 - \gamma_1)\frac{t_1 + t_2}{t_2^2 K} dT(x), \tag{5.53}$$

where t is the thickness and γ is the thermal expansion coefficient with the subscripts referring to the two layers. The function K is defined as

$$K = 4 + 6\left(\frac{t_1}{t_2}\right) + 4\left(\frac{t_1}{t_2}\right)^2 + \frac{E_1}{E_2}\left(\frac{t_1}{t_2}\right)^3 + \frac{E_2}{E_1}\left(\frac{t_2}{t_1}\right) \tag{5.54}$$

with the Young's modulus E. The bending of each individual segment is evaluated from its temperature for each time step. Subsequently, the bendings of the individual segments are transformed into the total deflection along the cantilever. The cantilever shape for different time steps are shown in Fig 5.22d,e. The simulated values (orange line) in Fig 5.22a are the z positions of the last cantilever segment, indicated by the dashed orange line in Fig 5.22d. The parameters used for the simulation are displayed in Table 5.4.1. For the material properties, values found in literature are used. The layer thicknesses are known from fabrication. The only free parameter left is the absorbed laser power P. For $P = 6.2$ mW the simulation fits best to the measured data. This corresponds to an absorption of 3.44%. The good agreement of simulation and experiment strongly suggests photo-thermal heating as the dominant process of the observed optical driving mechanism.

Table 5.4.1: Material parameters used for simulating the temperature distribution and bending of the cantilever.

material	**diamond** [120, 50]	**titanium** [46]
Young's modulus E [GPa]	1050	110
thermal conductivity λ [W/mK]	2000	-
thermal expansion coefficient γ [10^{-6} 1/K]	1.0	8.6
layer thickness T [μm]	4.5	0.2
heat capacity [J/m^{3}K]	1.78×10^6	-

Fig 5.22a shows that the time scale of the heat dissipation is longer than the oscillation period of the cantilever resonance (~1 µs). As a result, resonant optical driving leads to an increased average temperature of the driven cantilever. Fig 5.23a,b show the optically detected positions of two coupled cantilevers. Cantilever 1 is photo-thermally excited for the first 1 ms of the measurement. Cantilever 2 is never exposed to a driving mechanism besides its coupling to cantilever 1. While the driving is active, both cantilevers start to oscillate with increasing amplitude (dashed lines Fig 5.23a,b). It can be seen that the central position of the driven cantilever (cantilever 1) is changing during the excitation due to the accumulation of heat. When the cantilever is excited, heat accumulates and the average temperature along the cantilever rises. As a result, the equilibrium position of the cantilever is changing to the static bending caused by this new average temperature, and thus, moving the central position of the oscillation (solid line in Fig 5.23a). Afterwards, the cantilever is cooling down and the central position returns to the initial state. This is not observed for cantilever 2 as it is not heated.

Position-dependency of the photo-thermal excitation

The efficiency of the photo-thermal excitation depends strongly on the lateral position of the driving laser focus. Fig 5.24a shows the optically measured oscillation amplitude for different lateral positions of the excitation laser. During the measurement, the readout laser was positioned on the tip of the cantilever, while the excitation laser position was scanned using the galvo-scanner (see Section 5.4.4). The data indicates the cantilever shape (aligned roughly along the x-axis). Additionally, it shows a distinct pattern of the drive efficiency perpendicular to the cantilever. As this pattern is consistent over a long range along the cantilever, it is unlikely to be caused by local irregularities or defects of the absorbing titanium layer. The pattern could arise from the interaction between the laser light and the geometry of the cantilever. For example, by the excitation of different optical modes, depending on the entry position of the laser light. Due to these variations the photo-thermal excitation is influenced by drift and each small repositioning of the excitation laser potentially changes the drive efficiency.

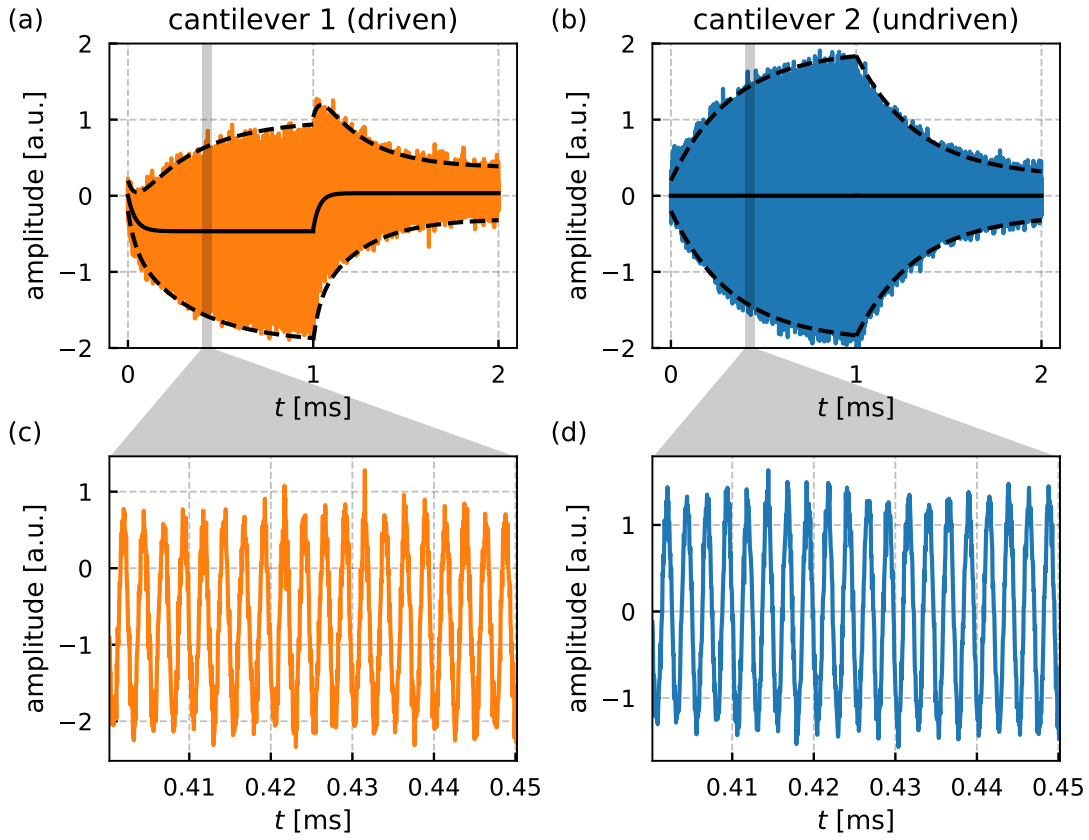

Figure 5.23: Simultaneous motion of two coupled cantilevers (cantilever 1 in (a) and cantilever 2 in (b)) resulting from a 1ms long resonant photo-thermal excitation of cantilever 1. The black lines in (a) and (b) are fitted to the amplitude (dashed lines) and central position (solid lines) of the oscillation. While the amplitude increases and decays equally for both cantilevers, the central position of cantilever 1 is shifting due to an increased average temperature. As the driving frequency is faster than the cool down time of the cantilever, heat is accumulated. Cantilever 2 is not exposed to photo-thermal heating and, thus, its central position is not changing. (c)/(d) shows a small subset of the data presented in (a)/(b), displaying the sinusoidal oscillation of the cantilevers.

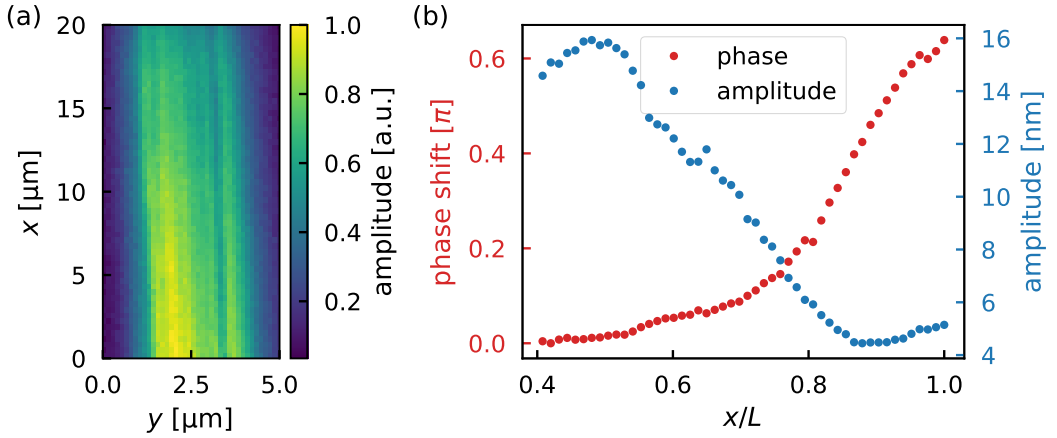

Figure 5.24: **(a)** Optically detected oscillation amplitude for different lateral positions of the excitation laser. The shape of the cantilever (aligned roughly along the y-axis) is reflected in the amplitude data. The drive efficiency varies strongly along the x-axis. **(b)** Measured amplitude and phase of the cantilever oscillation for different positions of the excitation laser along the cantilever. The amplitude has a maximum close to the center of the cantilever. The phase is changing towards the open end ($x = L$) of the cantilever.

The drive efficiency also varies along the cantilever, but with a significantly slower rate. Fig 5.24b shows the oscillation amplitude and phase for different excitation positions along the cantilever (x-axis). The amplitude is maximal close to the center of the cantilever ($x/L = 0.5$). Towards the tip of the cantilever, the amplitude is reduced by a factor of ~4. This result is rather unintuitive. Heating the cantilever close to the tip leads to a higher overall temperature, as the heat sink (clamping point) is further away from the heat source. This higher temperature results in a stronger bending. Furthermore, Fig 5.24b shows an unexpected change of the oscillation phase. To help understand the observed behavior, the temporal and positional heat, accumulating in the cantilever during the photo-thermal drive, was simulated. The simulation described in the following paragraph uses the same methods and parameters (Table 5.4.1) as the simulation introduced in Section 5.4.4. For each time step ($dt = 1$ ns), the heat distribution along the cantilever is simulated. The simulation is performed for multiple positions of the drive laser along the x-axis. From the heat, the temperature and bending of each cantilever segment can be derived. Fig 5.25c shows the simulated heat distribution at five time steps ((1) to (5), see Fig 5.25a) during a driving period. The upper graphs display the simulation results of a photo-thermal excitation at the center of the cantilever ($x/L = 0.5$, A in Fig 5.25b), while the lower graphs correspond to an excitation at the tip of the cantilever ($x/L = 1.0$, B in Fig 5.25b). The blue region represents the residual heat from the previous drive cycle and the red region indicates the heat added by the current laser pulse. From these simulated values, the maximal temperature variation along the cantilever can be retrieved (see Fig 5.25d). The highest temperature variation is caused at the position of the driving laser. Fig 5.25e shows the corresponding variations of the beam deflection. A centrally positioned excitation laser leads to a higher overall change of the deflection and thereby to a more efficient drive. This is caused by the fact that a bending of the cantilever closer to the clamping point has a higher influence on the overall deflection, as the bending changes the z-position of all following cantilever segments. Furthermore, the simulation shows that the timescale of the heat dispersion along the cantilever is on the same order as the driving period. This results in the observed phase shift of the oscillation. At first, the heat generated at the tip of the cantilever does not result in a significant deflection. While diffusing towards

the clamping point, the overall deflection caused by the heat increases. This results in a time-delayed, and thus phase-shifted, oscillation.

To compare the simulation to the experimental data, the simulated deflection over time is fitted by a sine wave. Fig 5.25 shows the simulated and measured deflection amplitude (f) and relative phase (g). Although, only the static bending resulting from the generated heat, and not the mechanical drive itself, is simulated, the simulated data shows good agreement with the experimentally observed behavior.

5.5 Spin-phonon coupling

The electron spin of a NV center is susceptible to magnetic and electric fields. This has led to two well-established methods for spin-phonon coupling in NV-based devices: strain-mediated coupling and magnetic field gradient coupling. While magnetic field gradient coupling can achieve significantly higher spin-phonon coupling rates, it in general suffers from experimental instabilities and drifts as it relies on external high gradient magnetic fields. In contrary, the spin-mediated coupling originates from the generation of effective electric fields inside the diamond material due to strain. As this coupling mechanism is intrinsic to the cantilever-NV system, it does not suffer from drifts. In the following subsections, both coupling mechanisms are discussed and experimentally demonstrated.

5.5.1 Strain-mediated coupling

The deformation of the diamond lattice, associated with a deflection of a cantilever, induces a strain field described by the tensor $\boldsymbol{\epsilon}(r)$. A FEM simulation of the strain in a bent cantilever is shown in Fig 5.27a. The strain is maximal at the surface and in the vicinity of the clamping point. Neglecting shear forces, the strain at the position of a NV center can be expressed as a diagonal tensor in the NV center's basis with the diagonal components $\{\epsilon_x, \epsilon_y, \epsilon_z\}$. It is convenient to distinguish axial strain $\epsilon_{\parallel} = \epsilon_z$ along the NV axis and transverse strain $\epsilon_{\perp} = \sqrt{\epsilon_x^2 + \epsilon_y^2}$ perpendicular to the NV axis. The effect of strain on a NV center can be modeled as an effective electric field.[121] The Hamiltonian can be

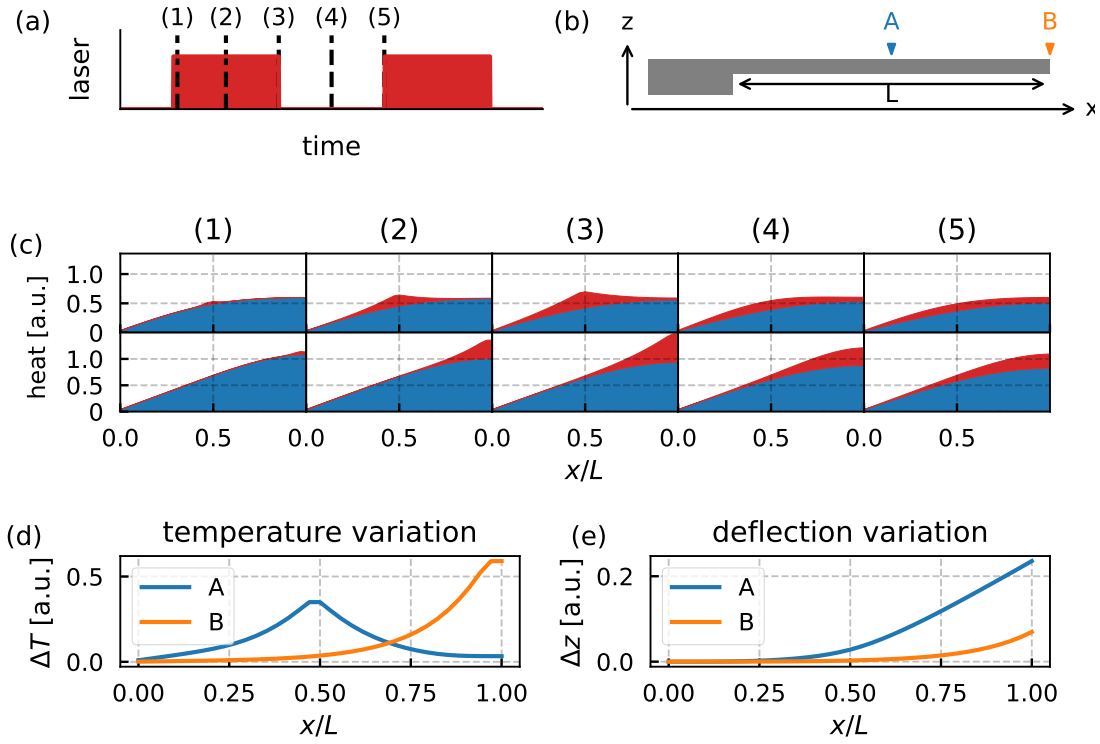

Figure 5.25: Simulation of the heat generation and diffusion during the resonant photo-thermal excitation. **(a)** Sequence of the photo-thermal drive with indications (dashed lines) of the time steps of the data presented in (c). **(b)** Sketch of the simulated cantilever with length L aligned along the x-axis. A and B indicate the positions of the laser excitation of the data presented in (c). **(c)** Simulated heat distribution along the cantilever for the time steps indicated in (a). The upper (lower) graphs correspond to the excitation position A (B) shown in (b). The blue region represents the residual heat of the previous driving cycle. The red region is the heat generated by the current laser pulse. **(d)** Maximal variation of the temperature along the cantilever for excitation positions A and B. The maximal variation occurs at the position of the excitation laser focus. **(e)** Variation of the deflection along the cantilever resulting from the temperature variations shown in (d). The variation of the deflection is higher for position A.

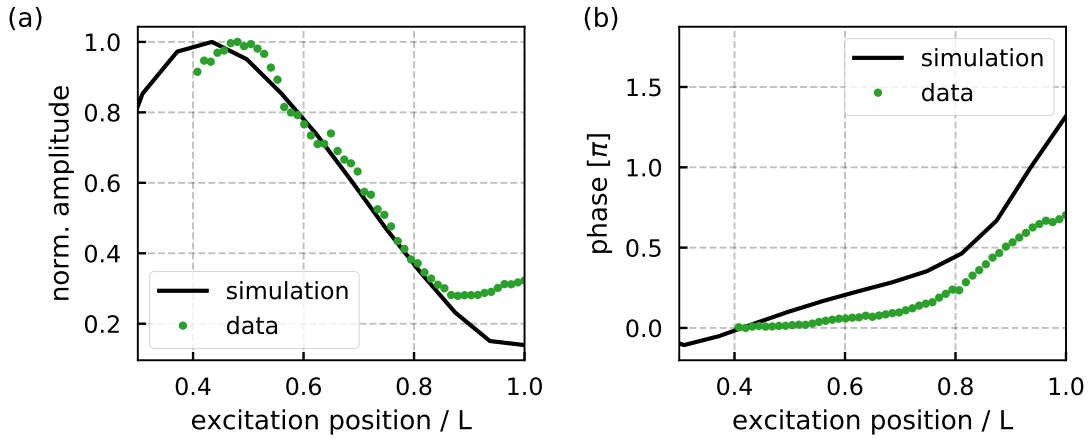

Figure 5.26: Comparison of the simulated and measured cantilever oscillations for different positions of the excitation laser along the cantilever. **(a)** Measured oscillation amplitude (green) and simulated amplitude of the cantilever deflection caused by photo-thermally induced heating of the cantilever (black). **(b)** Relative phase of the measured and simulated cantilever oscillations.

written as [33]

$$H = (D_0 + d_{\parallel}\epsilon_{\parallel})S_z^2 + \gamma_{\mathrm{NV}}\mathbf{S}\cdot\mathbf{B} + \frac{d_{\perp}\epsilon_{\perp}}{2}(e^{-i\phi_s}S_+^2 + e^{i\phi_s}S_-^2) \tag{5.55}$$

where D_0 is the zero-field splitting, $d_{\parallel}$ and $d_{\perp}$ are the axial and transverse strain susceptibilities, $S_{\pm}$ are the spin-1 raising and lowering operators and $\tan\phi_s = \epsilon_y/\epsilon_x$. Axial strain shifts the zero-field splitting, while transverse strain is causing a mixing of the $m_s = |\pm 1\rangle$ states. If the static magnetic field $\mathbf{B}$ is aligned to the NV axis, the eigenvalues of the new eigenstates $\{|0\rangle, |\pm\rangle\}$ are

$$E_0 = 0$$
$$E_{\pm} = D_0 + d_{\parallel}\epsilon_{\parallel} \pm \sqrt{(\gamma_{\mathrm{NV}}B_z)^2 + (d_{\perp}\epsilon_{\perp})^2}.$$

While axial strain shifts the energy levels of the $|\pm 1\rangle$ states symmetrically by $d_{\parallel}\epsilon_{\parallel}$, transverse strain introduces a energy splitting of $2d_{\perp}\epsilon_{\perp}$. The strain-induced energy shifts are illustrated in Fig 5.27b. For a strong enough magnetic field aligned along the NV axis ($\gamma_{\mathrm{NV}}B_z \gg d_{\perp}\epsilon_{\perp}$), the effect of transverse strain is suppressed.

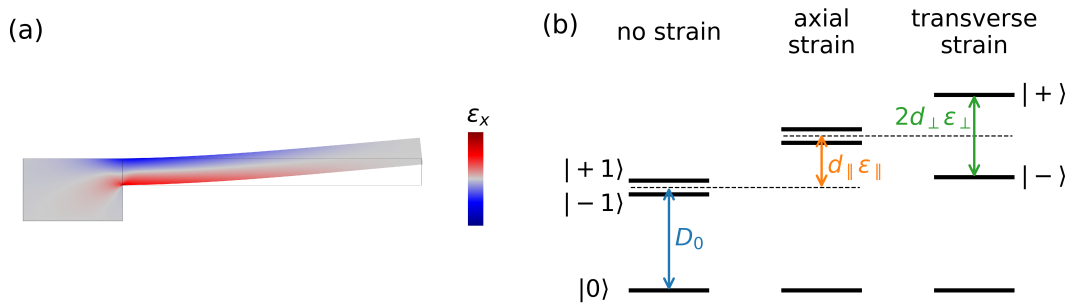

Figure 5.27: **(a)** FEM simulation of the strain in x-direction ϵ_x in a deflected cantilever. The strain is increases towards the sample surface. The highest strain occurs in the vicinity of the clamping point. **(b)** Ground-state energy levels in the presence of strain. Axial strain shifts the zero-field splitting. Transverse strain leads to a mixing of the $m_s = |\pm 1\rangle$ states.

For small deflections of the cantilever, the induced strain is proportional to the cantilever deflection z. The strain-induced interaction Hamiltonian can then be written as

$$H_{str} = d_\parallel \epsilon_\parallel S_z^2 = d_\parallel \frac{\partial \epsilon_\parallel}{\partial z}\bigg|_{z=0} \hat{z} S_z^2 = g'_{str} \hat{z} S_z^2, \tag{5.56}$$

where $g'_{str} = d_\parallel \frac{\partial \epsilon_\parallel}{\partial z}|_{z=0}$ is the ratio between the energy shift of the NV spin and the deflection of the cantilever and $\hat{z}$ is the position operator. Using $\hat{z} = x_{\mathrm{ZPF}}(a + a^\dagger)$ the interaction Hamiltonian can be written as

$$H_{str} = g_{str}(a + a^\dagger) S_z^2 \tag{5.57}$$

with the strain-induced spin-phonon coupling $g_{str} = g'_{str} x_{\mathrm{ZPF}}$.

To quantify the spin-mechanical coupling of a NV-cantilever system, the effect of a well-defined cantilever deflection onto the NV resonance frequencies is required. For this purpose, the mechanical susceptibility of the cantilever to the piezo-based excitation is measured (see Section 5.4.3). This allows to create cantilever oscillations with known amplitudes. The vibrations result in an oscillating strain field at the NV center's position. This field can be detected using a Hahn echo sequence. Fig 5.28 shows the spin contrast resulting from a Hahn

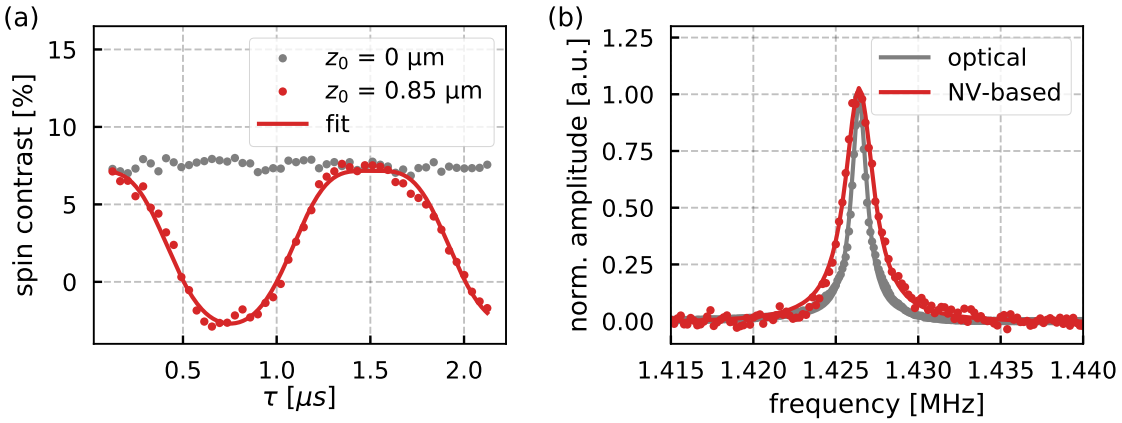

Figure 5.28: **(a)** Cantilever oscillation imprinted into the spin polarization by a Hahn echo sequence. The coupling is mediated by the oscillating strain field created by the cantilever motion. From the fitted curve, the spin-phonon coupling $g_{str}/2\pi = 3.0 \pm 0.1$ mHz can be determined. **(b)** Mechanical spectrum acquired optically (gray) and via the spin-based readout of the cantilever motion. The methods show a good agreement with each other. The spin-based readout adds a broadening due to the finite width of the Hahn echo filter function.

echo sequence with and without an oscillation of the cantilever. It can be seen that the mechanical motion is imprinted into the spin polarization, demonstrating the presence of a spin-phonon coupling. The spin polarization can be fitted with the function [122]

$$H(\tau) = AJ_0\left(4\frac{gz_0}{\omega x_{\mathrm{ZPF}}}\sin^2\left(\frac{\omega\tau}{4}\right)\right)e^{-\chi(\tau)}e^{-\left(\frac{\tau}{T_2}\right)^{\gamma}} + C. \tag{5.58}$$

Here, g is the spin-phonon coupling, z_0 is the amplitude of the cantilever oscillation, ω is the mechanical drive frequency, T_2 is the coherence time of the NV spin and x_{ZPF} is the zero-point fluctuation. A, B and γ are fitting parameters. $\chi(\tau)$ is the decoherence caused by thermal motion and can be neglected in the strongly driven regime [122]. Because the drive frequency ω and the cantilever amplitude z_0 are known, the spin-mechanical coupling $g'_{str} = \frac{g_{str}}{x_{\mathrm{ZPF}}} = 2\pi \times (1.21 \pm 0.05)$ kHz nm^{-1} can be obtained from the fitted parameters. With the zero-point fluctuation $x_{\mathrm{ZPF}} = \sqrt{\frac{\hbar}{2m_{\mathrm{eff}}\omega}} = 1.77 \times 10^{-15}$ m the spin-phonon coupling $g_{str} = g'_{str}x_{\mathrm{ZPF}} = 2\pi \times (2.14 \pm 0.08)$ mHz can be determined.

The NV-based readout of the mechanical motion can also be used to acquire a spectrum of the mechanical modes. For this purpose, the inter-pulse spacing τ of the Hahn echo sequence is set to match half the period of the cantilever drive $\tau = \pi/\omega_d$. Thus, the filter function of the decoupling sequence is always tuned into the cantilever frequency ω_d. By sweeping the drive frequency, mechanical modes of the system can be observed as a change in NV spin polarization. Fig 5.28b shows a mechanical spectrum measured optically (see Section 5.4.1) and via the NV spin. The results of both techniques are in good agreement with each other. The spin-based readout leads to a broadening due to the finite width of the Hahn echo filter function.

5.5.2 Magnetic field gradient coupling

A spin-mechanical coupling can be introduced by an external magnetic field gradient $\delta B_z = \frac{\partial B_z}{\partial z}|_{z=0}$. A deflection of a cantilever leads to a positional change of the embedded NV center and thus to a change of the magnetic field at the NV center's position. For sufficiently small deflections, δB_z can be approximated to be constant. In this case, the interaction Hamiltonian is

$$H_{mag} = \gamma_{\mathrm{NV}}\delta B_z \hat{z} S_z = g'_{mag}\hat{z}S_z \tag{5.59}$$

with $g'_{mag} = \gamma_{\mathrm{NV}} \delta B_z$.

The interaction Hamiltonian can be expressed using the magnetically induced spin-phonon coupling $g_{mag} = g'_{mag} x_{\mathrm{ZPF}}$ as

$$H_{mag} = g_{mag}(a + a^{\dagger}) S_z. \tag{5.60}$$

The highest magnetic field gradient can be achieved by bringing a small magnet as close as possible to the NV center position. An additional benefit of this approach is that the absolute magnetic field is minimized. This reduces the spin mixing of the NV caused by the off-axis magnetic field produced by the magnet. In the following experiments, the magnetic field gradient is employed by a magnetized tip that is positioned ~50nm above the sample surface using an atomic force microscope (Asylum Research, MFP3D). A graphical representation of the setup is depicted in Fig 5.29a. The tip was fabricated by coating a pulled fiber (tip diameter ~100 nm) with a 25 nm layer of Nickel. Afterwards, the Nickel was magnetized by a superconducting magnet (~3T). Fig 5.29b shows the spin signal of a NV center exposed to the magnetic field gradient. The signal was generated using a Hahn echo sequence and consists of the coherence decay, governed by the decoherence time T_2, superimposed with the influence of the mechanical oscillation. Analogous to the strain-mediated coupling case, the data can be fitted by Eq. (5.58). From the fitted parameters, the spin-mechanical coupling $g'_{mag} = \gamma_{\mathrm{NV}} \delta B_z = 2\pi \times (0.49 \pm 0.03)$ MHz/nm and the spin-phonon coupling $g_{mag} = 2\pi \times (0.87 \pm 0.03)$ Hz is determined (see Section 5.5.1). Furthermore, the magnetic field gradient $\delta B_z = (1.8 \pm 0.1) \times 10^5$ T/m was obtained. The influence of the mechanical oscillation can be highlighted by subtracting the fitted coherence decay from the data. The resulting spin contrast is presented in Fig 5.29c.

The magnetized tip reduces the coherence time of the NV spin. A comparison of the decay with and without the tip nearby is shown in Fig 5.29d. The coherence time is reduced by ~50%, from $T_2 = 3.10$ μs to $T_2 = 1.16$ μs. This hints at magnetic noise emanating from the magnetized tip. Furthermore, the overall spin contrast is decreased by the finite off-axial magnetic field produced by the tip at the NV position.

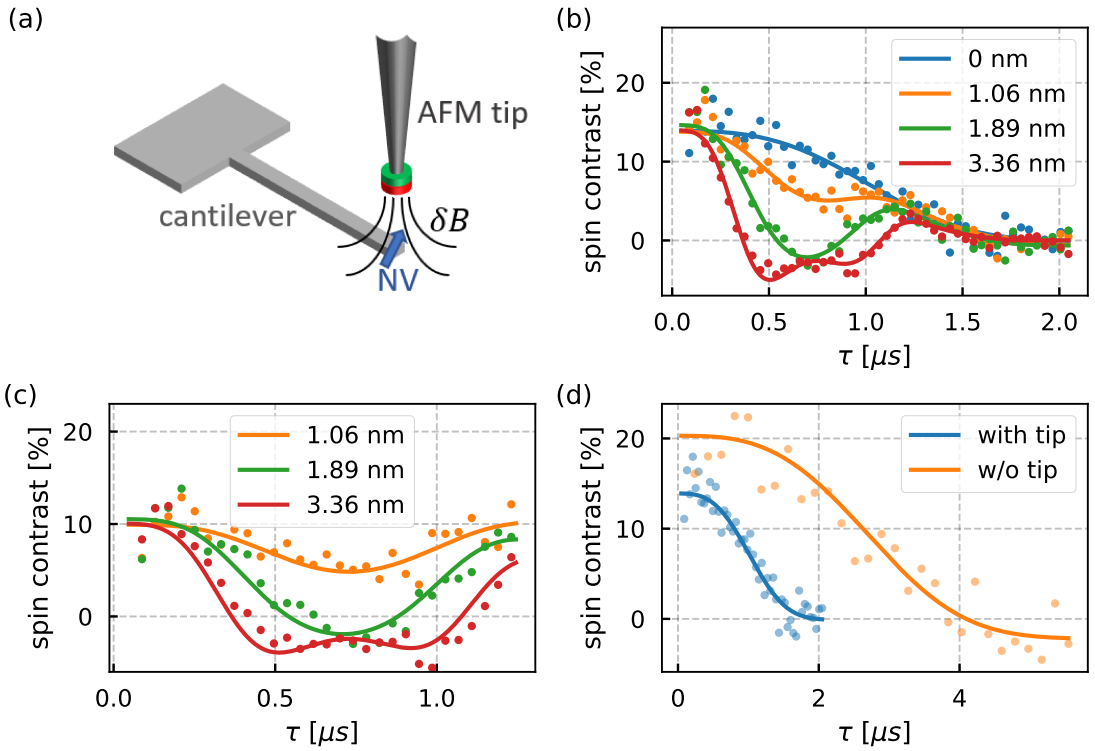

Figure 5.29: **(a)** Sketch of the setup used to establish spin-phonon coupling based on a high magnetic field gradient. A magnetic tip is positioned ~50nm above the cantilever surface, creating a magnetic field gradient at the NV position. A deflection of the cantilever leads to a positional change of the NV and thereby a change of the magnetic field at the NV position. **(b)** Hahn echo signal of a NV inside the magnetic field gradient for different oscillation amplitudes of the cantilever. The influence of the mechanical oscillation on the spin signal increases with increasing amplitude. Without an oscillation (blue) the spin signal only shows the spin decay governed by the decoherence time T_2. **(c)** Isolated imprint of the mechanical oscillation into the spin signal. The T_2 decay was subtracted from the data shown in (b). **(d)** Influence of the magnetized tip onto the spin signal. If the magnetized tip is close to the NV (blue), the decoherence time and overall spin contrast is decreased. The orange line presents the spin signal without a magnetized tip close by.

5.5.3 Spin-phonon cooperativity

The spin-phonon cooperativity

$$C = \frac{g^2}{\Gamma_s \Gamma_m} \tag{5.61}$$

is an important figure of merit of spin-mechanical hybrid systems. It compares the spin-phonon coupling g to the dissipation of the spin system (Γ_s) and the mechanical resonator (Γ_m). An important regime is $C > 1$, where the spin-mechanical interaction becomes coherent. For NV center based systems, reaching this regime is a very demanding task. So far, coherent spin-phonon coupling was not experimentally demonstrated in such systems.

It is convenient to rewrite the cooperativity in terms of the experimental parameters. Using the coherence time T_2, the dissipation of the spin system Γ_s can be written as

$$\Gamma_s = \frac{1}{2\pi T_2}. \tag{5.62}$$

The mechanical losses are described by the phonon decay rate $\Gamma_m = \hat{n}\gamma_m$, where $\hat{n}$ is the average number of phonons and $\gamma_m = \frac{\omega}{Q}$ is the mechanical ring-down time. For $k_B T \gg \hbar\omega$, the number of phonons can be approximated as $\hat{n} \approx \frac{k_B T}{\hbar\omega}$. The cooperativity can then be written as

$$C \approx \frac{2\pi\hbar g^2 Q T_2}{k_B T}. \tag{5.63}$$

The spin-phonon cooperativity for different sets of experimental parameters are presented in Table 5.5.2. The used parameters are based on the experimental settings and measurement results presented in Section 5.4.2, Section 5.5.1 and Section 5.5.2.

Even at LT and UHV, the cooperativity of the investigated system is below $C < 10^{-6}$ and orders of magnitude lower than the coherent coupling regime. Therefore, improvements of the experimental parameters are needed. While the spin coherence time and the spin-phonon coupling require adjustments to the sample, the temperature and quality factor are mainly determined by the sample environment. State of the art cryogenic systems offer temperatures below 100 mK and UHV capability. Under such conditions, diamond cantilevers possess quality factors up to 10^6 [47] (see Section 5.4.2). A cooperativity map,

Table 5.5.2: **Spin-phonon cooperativity** for different sets of experimental parameters. The values are based on the experimental parameters and measurement results presented in Section 5.4.2, Section 5.5.1 and Section 5.5.2.

spin-phonon coupling	ambient conditions	LT + UHV (4.8K, 2×10^{-9}mbar)
strain-mediated	2.3×10^{-17}	1.4×10^{-12}
magnetic field gradient	3.8×10^{-12}	2.4×10^{-7}

generated using Eq. (5.63), for $T = 100$ mK and $Q = 10^6$ is shown in Fig 5.30a. The dashed line indicates the boundary of the coherent coupling regime ($C = 1$). The orange dot marks the cooperativity that would be achieved with the sample used in this thesis. To achieve a cooperativity larger than one, the spin coherence time and the spin-phonon coupling need be increased.

For NV centers located deep inside bulk diamonds, coherence times in the order of millisecond have been observed under ambient conditions [123]. At low temperature (77 K), values of $T_2 > 500$ ms were recorded [124]. However, strain-mediated and magnetic field gradient based spin-phonon coupling both require NV centers close to the diamond surface. T_2 of such shallow NV centers is decreased by magnetic and electric noise emanating from the diamond surface [54, 55, 56, 58, 57]. Due to advances in implantation and fabrication techniques, spin coherence times of $T_2 > 100$ μs for shallow NV centers were achieved [59, 60, 61, 125].

Using magnetic field gradient based spin-phonon coupling, the coupling $g_{mag} = \gamma_{\mathrm{NV}}\delta B x_{\mathrm{ZPF}}$ is determined by the zero-point fluctuation x_{ZPF} and the magnetic field gradient δB. The spin-phonon coupling for different magnetic field gradients and zero-point fluctuations is shown in Fig 5.30b. The magnetic field gradient can be enhanced by improving the external magnetic field source. Magnetic field gradients of $\delta B > 10^6 T/m$ produced by magnetized AFM tips [13] and hard-disk-drive write heads [126] were successfully observed. Positioning and positional stability of such nanoscale magnetic devices is crucial to avoid off-axis magnetic field and magnetic noise. Overcoming these difficulties will lead to even higher magnetic field gradients.

Reducing the size, and thereby the mass of the mechanical resonator, is the

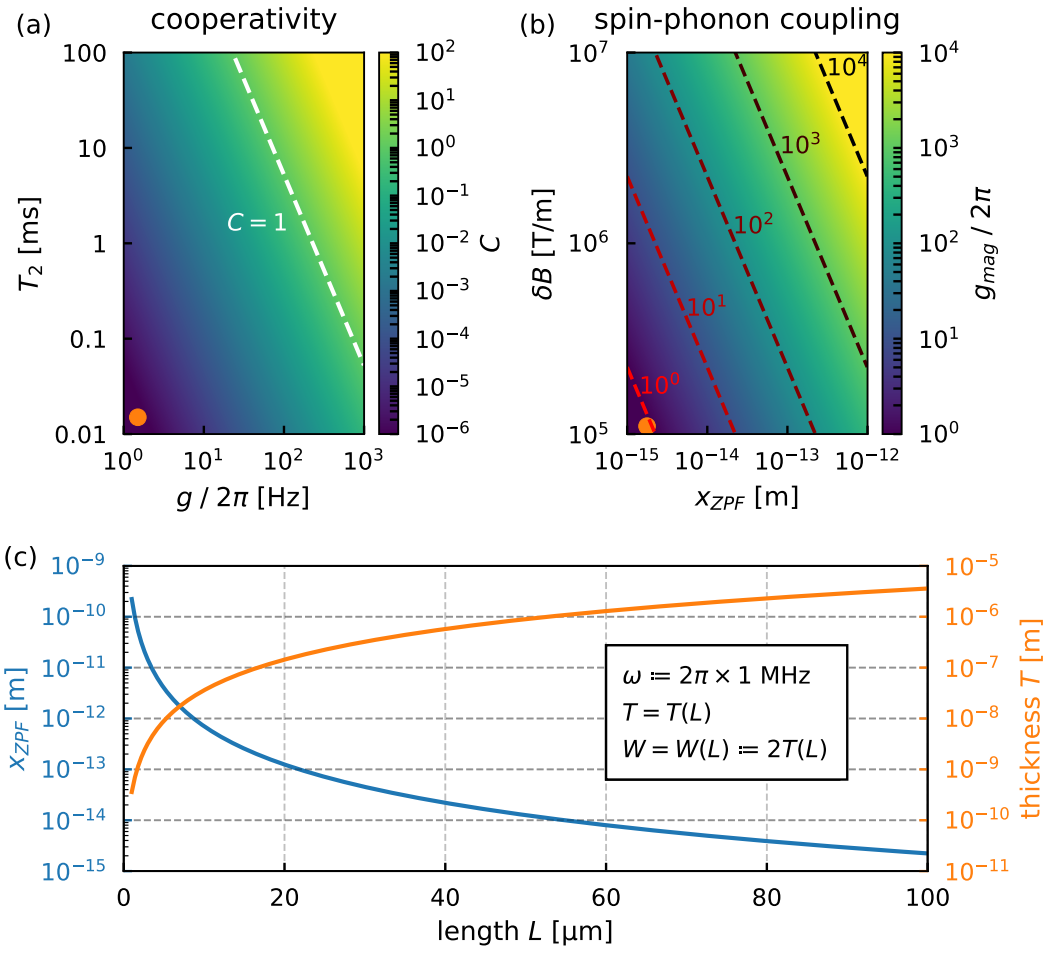

Figure 5.30: **(a)** Spin-phonon cooperativity map based on a temperature of 100 mK and a quality factor of 10^6. The dashed line represents the lower boundary of the coherent coupling regime ($C = 1$). The orange marker indicates the cooperativity of the sample used in this thesis. **(b)** Map of the calculated magnetic field gradient based spin-phonon coupling. The orange marker indicates the coupling of the sample used in this thesis. **(c)** Zero-point fluctuation (blue) and sample thickness (orange) for varying cantilever lengths. The resonance frequency of the cantilever is fixed to 1 MHz and the width is set to be double the thickness. The thickness is determined by the resonance frequency and the length.

main route to increase the zero-point motion. To investigate the achievable zero-point fluctuation, it is convenient to fix the resonance frequency. In this case, the thickness only depends on the cantilever length (see Eq. (5.48)). By additionally fixing the ratio between width and thickness α ($W = \alpha T$), the length is the only free parameter left. Using Eq. (5.48) and Eq. (5.45) the zero-point motion can be written as

$$x_{\mathrm{ZPF}} = \sqrt{\frac{1.87^4 \hbar E}{6\rho^2 \omega^3 \alpha L^5}}. \tag{5.64}$$

As an example, Fig 5.30c shows the zero-point fluctuation and corresponding thickness for $\omega = 2\pi \times 1$ MHz and $\alpha = 1.5$. From a practical point of view, the sample thickness can not be arbitrarily small and thus limits the achievable zero-point fluctuation. First of all, fabrication of thin samples is very demanding as exact knowledge of the etch rates is required. Furthermore, too thin cantilevers become too fragile to be processed and handled reliably. Nevertheless, utilizing sophisticated fabrication techniques, device thicknesses of ≈ 100 nm can be achieved [36]. In the previously used example ($\omega = 2\pi \times 1$ MHz, $\alpha = 1.5$), at length $L = 17$ µm and thickness $T = 104$ nm, the zero-point fluctuation is $x_{\mathrm{ZPF}} \approx 1.9 \times 10^{-13}$.

Finally, combining reported values for the various system parameters ($T = 100$ mK, $Q = 10^6$, $T_2 = 100$ µs, $\delta B = 10^6$ T/m, $\omega = 2\pi \times 1$ MHz, $L \times W \times T = 17 \times 0.15 \times 0.1$ µm) would lead to a cooperativity of $C \approx 1.3$ and a spin-phonon coupling $g_{mag} \approx 830$ kHz. Thus, achieving a coherent spin-phonon coupling is a demanding but possible task. Technical advances that improve one or more of the important system parameters would allow to access the high-cooperativity regime.

However, it is important to note that the key difficulty is to realize sufficient values for all system parameters at the same time. For example, reducing the size of a mechanical resonator typically increases the mechanical losses and thereby degrades the quality factor. Additionally, the reduced size increases effects of surface noise onto the NV center spin, reducing its coherence time.

5.6 Coupled diamond cantilevers as a quantum bus

In this section, the coupling of single spins to the common modes of a cantilever pair is discussed. First, the detection of common modes via NV spins in each cantilever is presented. In this initial experiment, the whole mechanical structure is excited simultaneously by the piezo-electric actuator. The experiment demonstrates the coupling of separate spins across both cantilevers to the same mechanical modes of the mechanical system. In a second step, the piezo-electric drive is replaced by a localized photo-thermal excitation of a single cantilever. The resulting mechanical oscillations are again detected by spins in both cantilevers. This demonstrates the transduction of an interaction from a local force to a distant spin system located in a different cantilever.

5.6.1 Strain-mediated detection of mechanical common modes

To allow phonon-mediated long-range interactions between individual spin system, the spins need to be coupled to the same mechanical mode. In this subsection, the coupling of individual spins to the mechanical common modes of the system is demonstrated. For this purpose, mechanical oscillations are resonantly excited using the piezo-electric actuator attached to the sample holder. The oscillations are then imprinted into the polarization of individual spins in both cantilevers. The used phase-locked XY8-N sequence is depicted in Fig 5.31a. The XY8-N microwave sequence is executed with a controllable delay θ relative to the mechanical drive signal. The inter-pulse spacing τ is fixed to match half the period of the cantilever drive signal $\tau = \pi/\omega_d$. Consequently, the filter function of the decoupling sequence is always tuned into the cantilever frequency ω_d and the accumulated phase is maximized.

Between the π-pulses, the mechanical motion imprints a relative phase φ into the superposition state $|\psi\rangle = \frac{1}{\sqrt{(2)}}(|0\rangle + e^{i\varphi}|-1\rangle)$ (see Section 1.5.7). For small cantilever deflections, the rate of the phase accumulation χ is proportional to the cantilever deflection [33, 36]. For a cantilever oscillation $z(t) = z_0 cos(\omega_d t + \alpha)$, the time-dependent rate can be written as

$$\chi(t, \theta, \alpha) = \chi_0 \cos(\omega_d(t + \theta) + \alpha), \tag{5.65}$$

where $\chi_0 = 2\pi g'_{str} z_0$ is the maximal phase accumulation rate and α is the initial

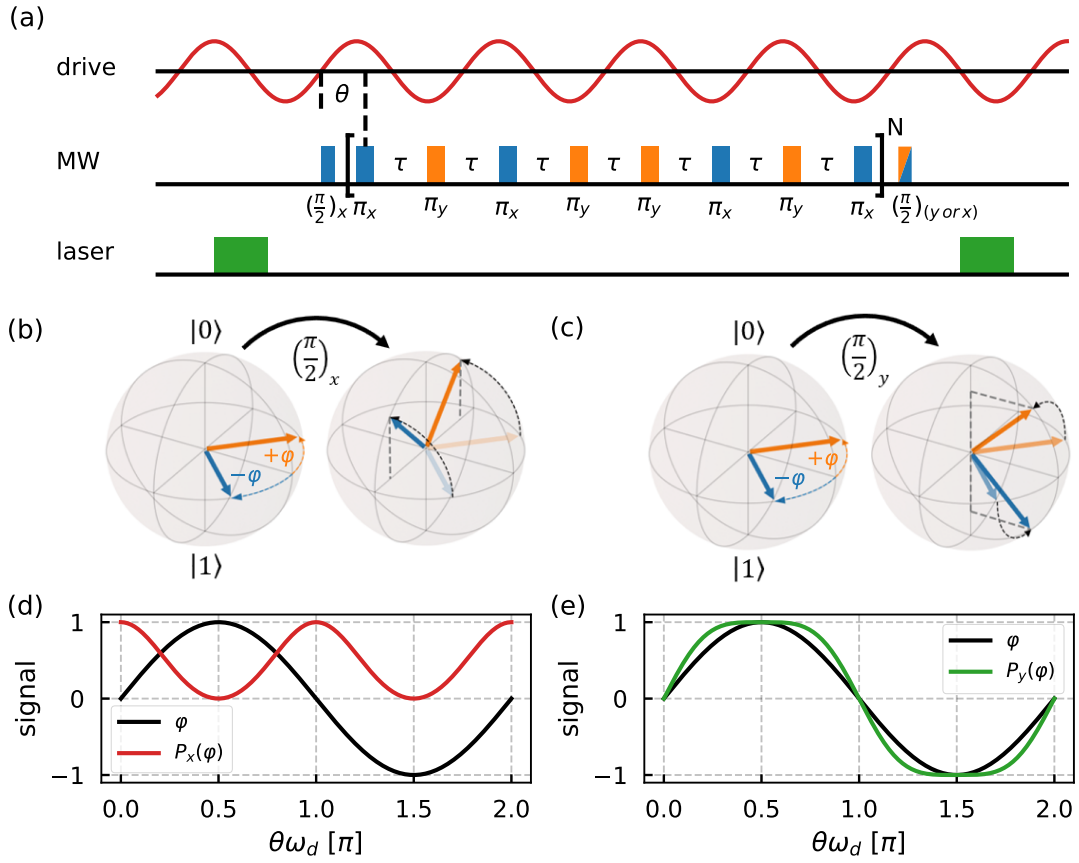

Figure 5.31: **(a)** Phase-locked XY8-N sequence used to map the mechanical motion into the spin polarization. The dynamical decoupling sequence is executed with a fixed delay ϕ relative to the mechanical drive signal. **(b)** Illustration of the X-projection of the accumulated phase onto the spin polarization using a $(\pi/2)_x$-pulse. A positive (orange) and negative (blue) phase result in the same spin polarization. Thus, the result is independent of the sign of the accumulated phase. **(c)** Illustration of the Y-projection of the accumulated phase onto the spin polarization using a $(\pi/2)_y$-pulse. The sign of the accumulated phase is stored in the resulting spin polarization. **(d)** X-projection (red) of an oscillating accumulated phase φ (black). As the sign of the phase is not influencing the projected results, the oscillation of the spin polarization signal is doubled. **(e)** Y-projection (green) of an oscillating accumulated phase φ (black). The projected signal oscillates with the frequency of the accumulated phase.

phase offset of the oscillation. The total phase acquired during a XY8-N sequence can be calculated by integrating the rate of phase accumulation over all free evolution intervals between the π-pulses. As the waiting time τ is synchronized to the periodicity of the mechanical oscillation, all even and odd interpulse intervals are equivalent. Thus, it is sufficient to integrate over the first two intervals. Using the relation $\tau = \pi/\omega_d$, the total acquired phase can be written as

$$\varphi(\theta,\alpha) = \frac{N}{2}\Big[\int_0^{\pi/\omega_d} \chi(t,\theta,\alpha)dt - \int_{\pi/\omega_d}^{2\pi/\omega_d} \chi(t,\theta,\alpha)dt\Big]. \tag{5.66}$$

Integrating gives the total acquired phase

$$\varphi(\theta,\alpha) = \frac{16\chi_0}{\omega_d}\cos(\omega_d\theta + \alpha). \tag{5.67}$$

The accumulated phase oscillates in θ with the frequency and phase of the mechanical oscillation. The projection of the phase into the spin polarization can be realized by a rotation around the x-axis or the y-axis depending on the relative phase of the final $\frac{\pi}{2}$-pulse. A $(\frac{\pi}{2})_x$-pulse results in a spin polarization

$$P_x\Big(\varphi(\theta,\alpha)\Big) = \cos\Big(\varphi(\theta,\alpha)\Big), \tag{5.68}$$

while a $(\frac{\pi}{2})_y$-pulse leads to a polarization

$$P_y\Big(\varphi(\theta,\alpha)\Big) = \sin\Big(\varphi(\theta,\alpha)\Big). \tag{5.69}$$

As illustrated in Fig 5.31b, the projection around the x-axis will map the phases $-\varphi$ and $+\varphi$ into the same spin polarization

$$P_x(-\varphi) = P_x(+\varphi). \tag{5.70}$$

Using $\varphi(\theta,\alpha) = -\varphi(\theta,\alpha+\pi)$ and Eq. (5.70), we get $P_x\Big(\varphi(\theta,\alpha)\Big) = P_x\Big(\varphi(\theta,\alpha+\pi)\Big)$. Thus, when using the x-projection, the spin polarization signal is not changed when the detected signal is shifted by π. Consequently, the π phase shift between the two cantilevers at the anti-symmetric mode can not be observed in the spin polarization in this case. Fig 5.31d shows calculated values for the accumulated phase (black) and the x-projected spin polarization (red) caused by an oscillating strain field. The frequency of the spin polarization is effectively doubled relative to the initial signal.

The projection around the y-axis, on the other hand, imprints the sign of the phase into the spin polarization (see Fig 5.31c). Therefore, the recorded spin polarization is not invariant under a π phase shift of the detected oscillation. Hence, the y-projection can be used to identify the anti-symmetric mode of the coupled cantilever pair, by observing the phase shift between the cantilevers. Fig 5.31d shows theoretical values of the spin polarization (green) and accumulated phase (black) resulting from a sinusoidal detected signal. The periodicity of the initial signal, the accumulated phase and the spin polarization are identical. Thus, the projection around the y-axis directly shows the frequency and phase of the detected oscillation.

Fig 5.32 shows the spin polarization of two individual NVs generated by a phase-locked XY8-1 sequence with a final $(\frac{\pi}{2})_y$-pulse. The NVs are located at the clamping points of each cantilever of the coupled system. The delay between the microwave sequence and the mechanical drive signal θ is swept. During the measurement shown in Fig 5.32a (Fig 5.32b) the symmetric (anti-symmetric) mode of the cantilever pair is excited by a piezo-electric actuator. The oscillations seen in the spin signal are a result of the strain-mediated coupling to the mechanical motion. For both mechanical modes, the generated spin signal oscillates with the frequency of the mechanical drive signal ω_d. At the symmetric mode, the spin signals of the two NV centers oscillate in-phase, while they are shifted by π at the anti-symmetric mode. The characteristic mode shapes are imprinted into the NV spin, demonstrating the coupling of the spin systems to the common modes of the mechanical structure.

5.6.2 Detecting local forces with a distant spin

In this section, the photo-thermal driving technique (see Section 5.4.4) is used to demonstrate the mediation of interactions between distant systems coupled to the cantilever pair. Fig 5.33a depicts the different subsystems of the coupled system. The cantilevers are coupled to each other with a coupling constant $\tilde{g}$, resulting in the common modes. At the same time, spins embedded in the cantilevers are coupled to the mechanical degrees of freedom with a coupling constant g. The spins are influenced by the mechanical motion but can also apply forces to the cantilevers. In the investigated hybrid system, the forces

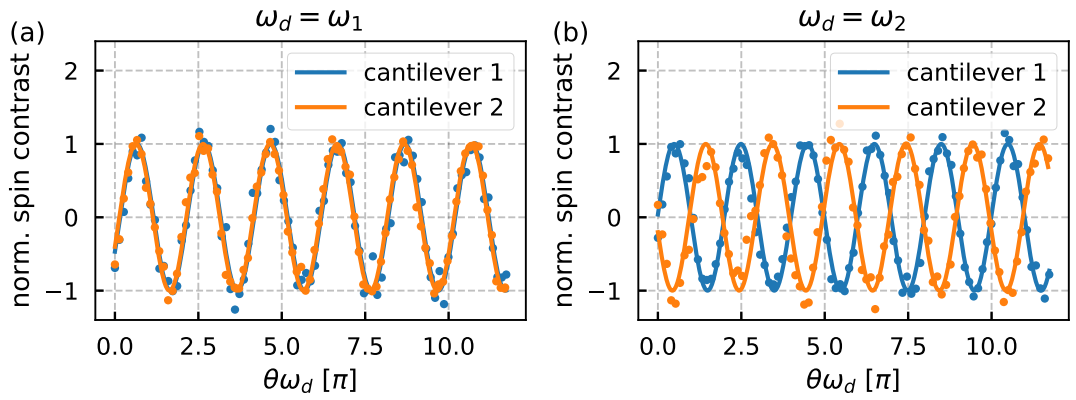

Figure 5.32: Detection of the two mechanical common modes via NV spins. The motion of both cantilevers is imprinted into the spin polarization using a phase-locked XY8-1 sequence with varying delay θ. The cantilever oscillation is excited by a piezo-electric actuator. **(a)** Oscillations at the symmetric mode. **(b)** Oscillations at the anti-symmetric mode.

exerted by the NV center spins are too weak to be observed experimentally. However, the local force associated with the photo-thermal heating can be used to emulate this interaction. In the presented experiment, the effect of the drive laser interacting with one of the cantilevers is observed via a spin located in the other cantilever, as illustrated in Fig 5.33b.

The spin used for the readout is positioned close to the clamping point to increase the strain-mediated coupling. The drive laser was pulsed at the frequency of the anti-symmetric mode of the cantilever pair. A phase-locked XY8-5 sequence was performed on the readout spin. The delay θ was swept to observe the influence of the mechanical motion. During the measurement, the final projecting pulse of the microwave sequence was alternating between a $(\frac{\pi}{2})_x$- and $(\frac{\pi}{2})_y$-pulse. This way, the x- and y-projected spin polarization were measured simultaneously. The experiment was performed with the drive laser once focused onto the cantilever hosting the NV and once focused onto the other cantilever. The recorded spin signals are shown in Fig 5.34a and b. P_x and P_y were simultaneously fitted by Eq. (5.68) and Eq. (5.68), respectively.

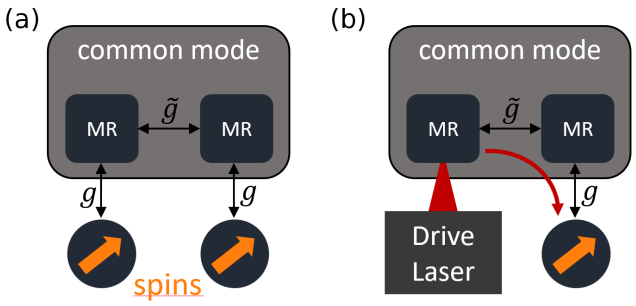

Figure 5.33: Illustration of the coupling between the different subsystems of the hybrid system. **(a)** The mechanical resonators (MR) are coupled with a coupling constant $\tilde{g}$. The spins embedded in the resonators are coupled with a coupling constant g to the mechanical degrees of freedom. **(b)** Depiction of the experimental scheme. The force between spin and cantilever is emulated by the local force produced by the drive laser. The effect of this interaction is observed via a spin located in the other cantilever. This demonstrates the mediation of interactions between separate systems coupled to the cantilever pair.

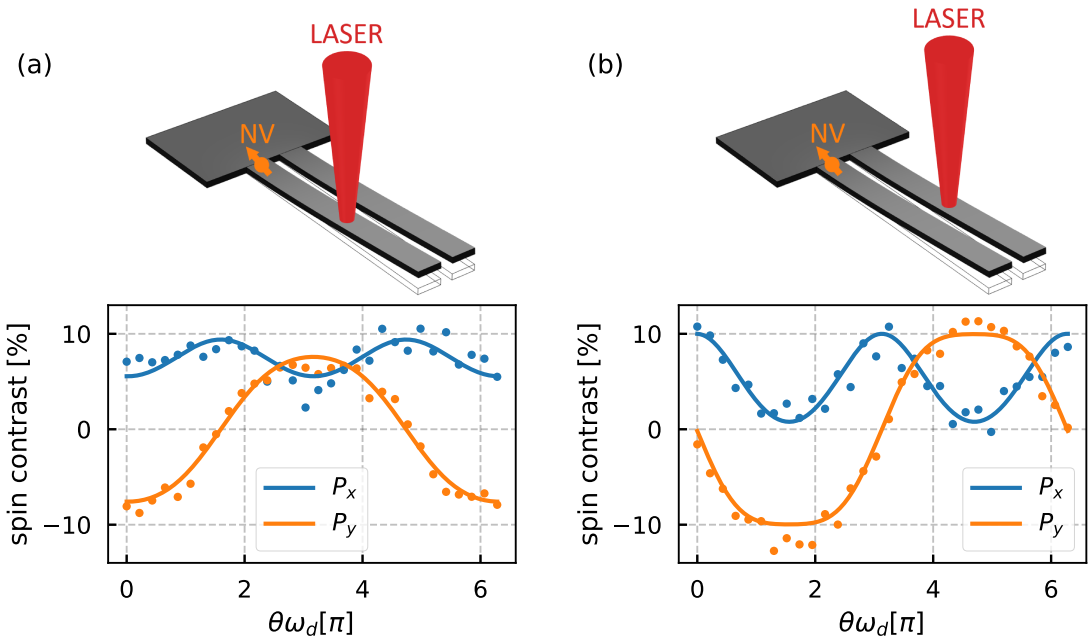

Figure 5.34: Cantilever motion detected by an embedded NV center. The projections P_x and P_y are simultaneously measured by alternating the final $\frac{\pi}{2}$-pulse of the phase-locked XY8-5 between a $(\frac{\pi}{2})_x$- and $(\frac{\pi}{2})_y$-pulse. The cantilever oscillation is excited by a resonant photothermal drive at the anti-symmetric mode. **(a)** The drive laser is positioned on the cantilever hosting the NV center. **(b)** The drive laser is moved to the other cantilever. The cantilever motion is still detected by the NV center. Hence, the effects of the local force generated by the drive laser is mediated to the NV center via the mechanical structure.

For both drive laser positions, the mechanical motion is detected by the NV center. Hence, the effects of the local force, exerted by the photo-thermal drive, are mediated through the complete cantilever pair. This experimentally demonstrates the potential of the coupled cantilever pair as a quantum bus, which transduces interactions between local systems coupled to the mechanical system.

5.6.3 Estimation of an upper bound for the spin-spin interaction

In this section, an estimate of the upper bound of the phonon-mediated effective spin-spin interaction in the cantilever pair is derived. Let's assume that there are two spins (spin 1 and spin 2 in the following), each positioned at the apex of one of the cantilevers. Both spins are exposed to a high magnetic field gradient in z-direction δB_z. First, the oscillation amplitude of the mechanical system caused by a rotation of spin 1 is calculated. Due to its magnetic moment, spin 1 experiences a force of $F = \mu_B \delta B_z S_1^z$ in the magnetic field gradient. Thus, a rotation of the magnetic moment of spin 1 results in an oscillating force with amplitude $F_0 = \mu_B \delta B_z$. Ideally, this force is completely applied to the cantilever. For low damping, the resulting saturated oscillation amplitude is approximately $A_0 = \frac{F_0 Q}{k}$, where Q is the quality factor and k the spring constant. The cantilever pairs investigated in this work are coupled sufficiently strong, such that both cantilevers will exhibit the same oscillation amplitude if only one of the them is exposed to a driving force. This assumption is supported by the experimental results shown Fig 5.23. Note that variations between the parameters of the individual cantilevers (e.g. slightly different lengths due to fabrication imperfections) can result in an asymmetric mechanical spectrum and different amplitudes as described in Section 5.7.

The mechanical motion results in an energy shift of the states of spin 2. From the experiments presented in Section 5.5.2, we determined the ratio g'_{mag} between the energy shift and the oscillation amplitude. Using this parameter, we get the energy shift experienced by spin 2

$$dE = g'_{mag} A_0 = g'_{mag} \frac{\mu_B \delta B_z Q}{k}. \tag{5.71}$$

As this energy shift is solely generated by a rotation of spin 1, it can be seen as an estimate of the effective spin-spin coupling $g_{s-s} = dE$. However, as a saturated oscillation amplitude is assumed and losses due to deformation of the diamond material are ignored, the real value of the effective spin-spin coupling must be smaller. Hence, the estimated value has to be regarded as an upper bound of the effective coupling.

Using the experimentally determined values $\delta B = 1.8 \times 10^5$ T/m, $Q = 1768$ and $g'_{mag} = 2\pi \times 0.49$ MHz/nm, the effective coupling is $g_{s-s} = 60.1$ mHz. In this case, the force applied by spin 1 is $F_0 = 1.7 \times 10^{-18}$ N and the oscillation amplitude is $A_0 = 1.97 \times 10^{-17}$ m. It is important to note that the calculated oscillation amplitude is smaller than the zero-point fluctuation of the cantilever pair. This shows the need for improvements of the system parameters to observe spin-spin interactions experimentally.

With a quality factor of $Q = 10^6$ (LT and UHV), the effective coupling increases to $g_{s-s}(Q = 10^6) = 34.26$ Hz. Under these conditions, the oscillation amplitude $A_0 = 1.11 \times 10^{-14}$ m is higher than the zero-point fluctuation.

5.6.4 Scalability of the cantilever array

An important aspect of a potential quantum bus is its scalability, as effective quantum information processing devices require a high number of coupled qubits. Increasing the number of cantilevers N in the array effects the performance of the system in two ways.

First, the increasing mass of the system reduces the zero-point fluctuation. The FEM simulation presented in Fig 5.8 shows that the effective mass can be approximated to increase linearly with the number of cantilevers $m_{\text{eff}} \propto N$ (see Eq. (5.35)). Accordingly, the zero-point fluctuation $x_{\text{ZPF}} = \sqrt{\frac{\hbar}{2m_{\text{eff}}\omega}}$ and the spin-phonon coupling $g = g' x_{\text{ZPF}}$ both scale with $\propto \frac{1}{\sqrt{N}}$. Hence, an increasing number of cantilever raises the requirements for the system parameters.

Second, an increasing number of cantilevers increases the number of mechanical modes accordingly, and thereby the mode density. A too high mode density will render individual addressing of single mechanical modes impossible. A FEM simulation to estimate the maximum number of cantilevers for a given quality factor is presented in Section 5.2.3 and Fig 5.7. A quality factor of

$Q = 10^6$ allows for cantilever numbers of $N > 100$.

However, the limitation set by the discussed scaling behavior can be circumvented by adding a layer of encapsulation to the mechanical structure. A high number of resonators can be realized as a set of small cantilever arrays, interconnected by a switchable capacitive interaction [42]. In this setup, each cantilever array is small enough to operate in the coherent spin-phonon coupling regime. If a transfer of information between two spins in different arrays is needed, the two arrays can be temporarily coupled via the switchable interaction. This way, the scalability behavior of the hybrid system only limits the number of resonators in a single sub-array, but not the total number of resonators in the quantum network.

A similar result can be achieved using advanced phononic structure to isolate sub-arrays in a large quantum network [127].

5.7 Mass sensing with coupled resonators

Conventionally, mass sensing protocols, based on mechanical resonators, exploit the resonance frequency shift caused by a mass added to the resonator. This techniques is used with different mechanical systems, like e.g. cantilevers [128], nanoelectromechanical systems (NEMS) [129] and carbon nanotubes [130]. The potential of NV-based devices using this approach have already been studied [131]. In a system of coupled mechanical resonators, an introduced mass imbalance does not only lead to a frequency shift, but additionally to a change of the relative amplitudes of the common modes (see Fig 5.35). This amplitude changes can be used as a measure for the added mass. Under certain conditions, this can be exploited to enhance the mass sensitivity in comparison to frequency shift based techniques [132]. In this section, the mass sensing capabilities of the double diamond cantilever system are explored.

Assuming an undamped oscillation of the coupled resonators, the equations of motion of the system can be expressed as an eigenvalue problem

$$\begin{bmatrix} 1+\kappa & -\kappa \\ -\kappa & (1+\kappa)/(1+\delta) \end{bmatrix} \boldsymbol{u} = \lambda \boldsymbol{u}, \tag{5.72}$$

where $\kappa = k'/k$ is the relative coupling and $\delta = \Delta m/m$ is the ratio between the

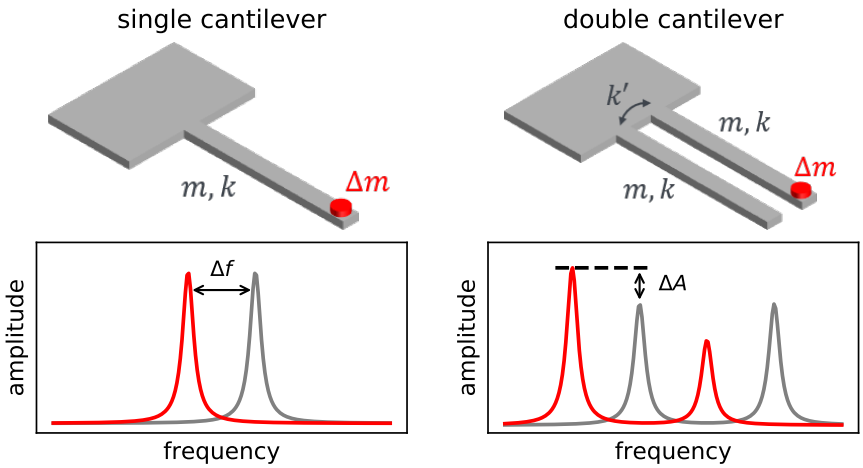

Figure 5.35: Effect of an added mass Δm to a single (left) and double (right) cantilever system. The resonance frequencies of both systems are shifted due to the additional mass. However, the mass imbalance in a cantilever pair will also lead to a change of the amplitudes. This is the result of a partial localization of the common modes. The amplitude change can be used as a measure for the added mass.

added mass and the mass of the cantilever. The state vector $\boldsymbol{u}$ is defined by $[z_1 \;\; z_2]^T = \boldsymbol{u}e^{i\lambda t}$, where z_1 and z_2 are the deflections of the cantilevers. For $\delta = 0$, the eigenvalues are $\lambda_1^0 = 1$ and $\lambda_2^0 = 2\kappa+1$. The corresponding normalized eigenstates are $\boldsymbol{u}_1^0 = 1/\sqrt{2}[1 \;\; 1]^T$ and $\boldsymbol{u}_2^0 = 1/\sqrt{2}[1 \;\; -1]^T$. By performing a perturbation expansion in δ, an approximation for the relative change of the eigenvalues and eigenstates, caused by a change of δ, can be obtained [132]. The relative change of the eigenvalues is

$$\Gamma_f = \frac{\lambda - \lambda^0}{\lambda^0} = -\frac{\delta}{2}. \tag{5.73}$$

while the relative change of the eigenstates is

$$\Psi_A = \frac{|\boldsymbol{u}_i - \boldsymbol{u}_i^0|}{|\boldsymbol{u}_i^0|} = \left(\frac{1}{4} + \frac{1}{4\kappa}\right)\delta, \quad i = 1, 2. \tag{5.74}$$

It is convenient to express Γ_f and Ψ_A using our experimental parameters. Therefore, we will relate to Γ_f as the relative frequency change

$$\Gamma_f = \frac{\Delta f}{f_0}, \tag{5.75}$$

where Δf is the change of the mode frequency after a mass is added to one of the cantilevers ($\delta > 0$) and f_0 is the resonance frequency for $\delta = 0$. In the same way we correspond to Ψ_A as the relative change of the oscillation amplitude

$$\Psi_A = \frac{dA}{A_0} \tag{5.76}$$

due to an added mass. Here, dA is the change of the oscillation amplitude and A_0 is the amplitude for $\delta = 0$.

In contrast to the relative frequency change, the relative amplitude change depends on the relative coupling of the system. The susceptibility of the oscillation amplitude to mass imbalances can be increased drastically by lowering the coupling. Fig 5.36a shows FEM simulations of the resonance frequencies (upper) and relative amplitudes (lower) for an increasing added mass. The simulation was performed for three different relative couplings. The frequency barely changes with decreasing κ. In contrast, the relative amplitude change for small δ is increasing with decreasing κ. This increase comes at the cost of a smaller dynamic mass sensitivity range. The green dashed lines indicate the

approximated relative frequency (Eq. (5.75)) and amplitude (Eq. (5.73)) change. To provide a better insight into the dynamics of the cantilever pair, Fig 5.36b shows approximations of the cantilever spectra for different relative couplings and added masses. The spectra were created by adding two Lorentzian functions with the simulated resonance frequency and amplitude values. It can be seen that the changes of the amplitudes, caused by mass changes, are increased for lower relative couplings.

To get an estimate for the achievable mass sensitivity, we first assume that κ is small. The relative amplitude change is then $\Psi_A \approx \delta/4\kappa$. By additionally replacing dA with the amplitude sensitivity η_A we get an expression for the mass sensitivity η_m of the system

$$\eta_m = 4\frac{\kappa m}{A_0}\eta_A. \tag{5.77}$$

The photon shot-noise limited amplitude sensitivity can be expressed as [131, 133]

$$\eta_A = \frac{1}{2\pi K g'\sqrt{T_2}}. \tag{5.78}$$

Here, K is a setup-dependent constant with a typical value being $K = 0.01$. Further, g' is the spin-mechanical coupling (see Section 5.5) and T_2 is the coherence time. Using Eq. (5.78), the mass sensitivity can be written as

$$\eta_m = \frac{2\kappa m}{\pi A_0 K g'\sqrt{T_2}}. \tag{5.79}$$

For a cantilever with the dimensions 5x0.1x0.1 μm, a small relative cantilever coupling $\kappa = 10^{-3}$, $A_0 = 50$ nm, $g' = 2\pi \times 0.49$ MHz nm^{-1}, $T_2 = 100$ μs and $K = 0.01$, the mass sensitivity is $\eta_m \approx 7$ zg Hz$^{-1/2}$. This value is comparable to studies performed on single cantilever systems [131].

In the following, we will compare the mass sensitivity achievable by the two effects - frequency and amplitude change. For this purpose, we assume that both effects are independent of each other and determine the sensitivity achieved by only considering a change of the frequency or the amplitude change. To make the comparison easier, we assume that the frequency shift is measured by driving the system slightly off-resonant and monitoring the oscillation amplitude. In this case, a change of the resonance frequency will lead

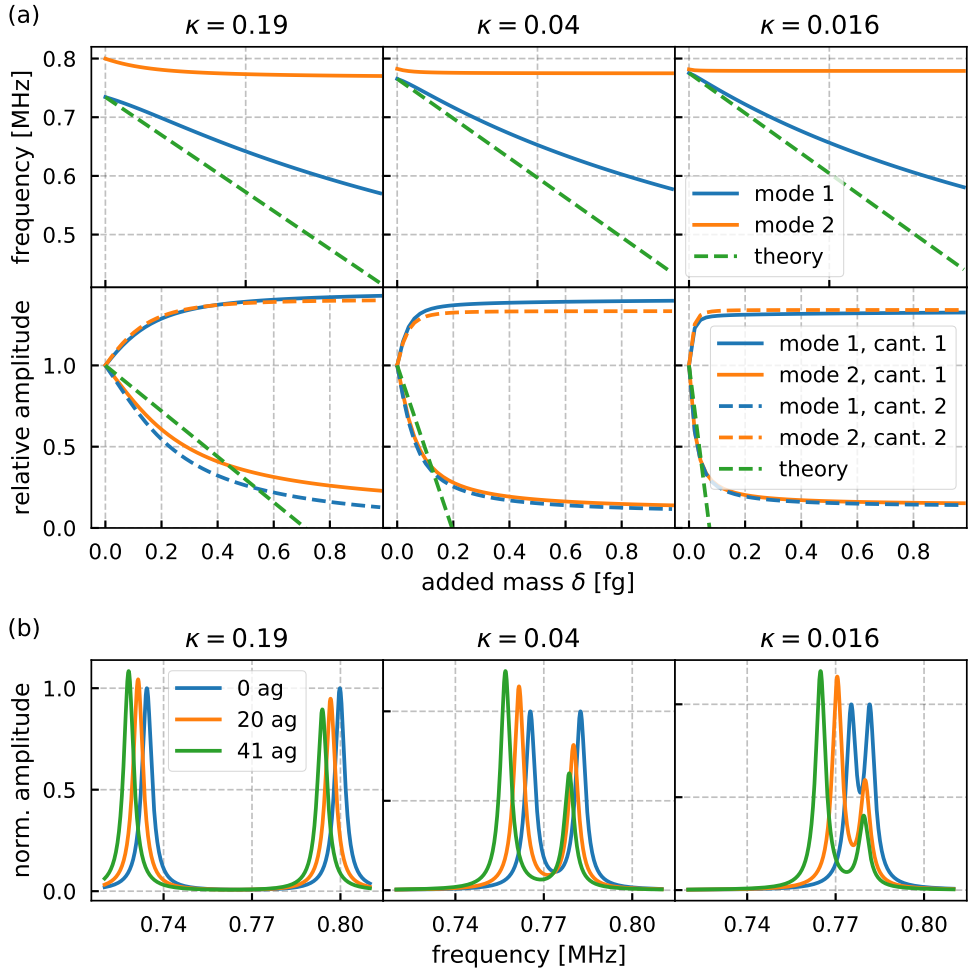

Figure 5.36: **(a)** FEM-simulation of the frequency and amplitude changes resulting from a mass added to a cantilever pair. The simulation was performed with different relative coupling strength κ. With decreasing κ, the maximum slope of amplitude change increases, indicating an increasing mass sensitivity. At the same time, the dynamic range for mass detection is decreasing. Thus, a high mass sensitivity is only possible for small mass changes. **(b)** Mechanical spectra generated using the simulated frequency and amplitudes values from (a). The width of the peaks is set to 2 kHz, which corresponds to a quality factor of ~400. The spectra are plotted for different added masses. The frequency spacing between the modes decreases with decreasing coupling. Thus, the mechanical modes can not be resolved for too small couplings.

to an effective change of the amplitude dA_f. We define the relative amplitude change Γ_f caused by the frequency shift as

$$\Psi_f = dA_f/A_0. \tag{5.80}$$

For the estimation, it is sufficient to assume that the resonance curve of the system follows a Lorentzian function of the form

$$f(x) = a\frac{b}{(x-x_0)^2+b^2}. \tag{5.81}$$

The highest slope of this Lorentzian function is

$$\max\left(\frac{df(x)}{dx}\right) = \frac{9a}{8\sqrt{3}b^2} = C\frac{a}{b^2} \tag{5.82}$$

with $C = \frac{9}{8\sqrt{3}}$. Thus, the largest possible amplitude change dA_f, due to a frequency shift df, is

$$dA_f = C\frac{a}{b^2}df. \tag{5.83}$$

It is convenient to express the HWHM b with the experimental parameters Q and f_0. This gives $b = f/2Q$. With the amplitude of Eq. (5.81) $A_0 = a/g$, Eq. (5.83) and Eq. (5.73) we can express the relative amplitude change as a function of the relative frequency or mass change:

$$\Psi_f = 2CQ\Gamma_f = CQ\delta. \tag{5.84}$$

Finally, the ratio

$$\frac{\Psi_f}{\Psi_A} = \frac{CQ}{\frac{1}{4}+\frac{1}{4\kappa}} \tag{5.85}$$

can be used to estimate the benefit of the relative amplitude change Ψ_A. Notably, this ratio only depends on the quality factor and coupling of the system. This allows for a comparison independent of the actual cantilever geometry and the mass change of interest. The ratio is shown in Fig 5.37b. The orange line is an iso-line along $\Psi_f/\Psi_A = 1$. It can be seen that the relative amplitude change only offers an improvement for low quality factors and low couplings.

For a mass sensing application, the relative coupling κ cannot be arbitrarily small. The smallest usable κ is limited by the quality factor of the system. The

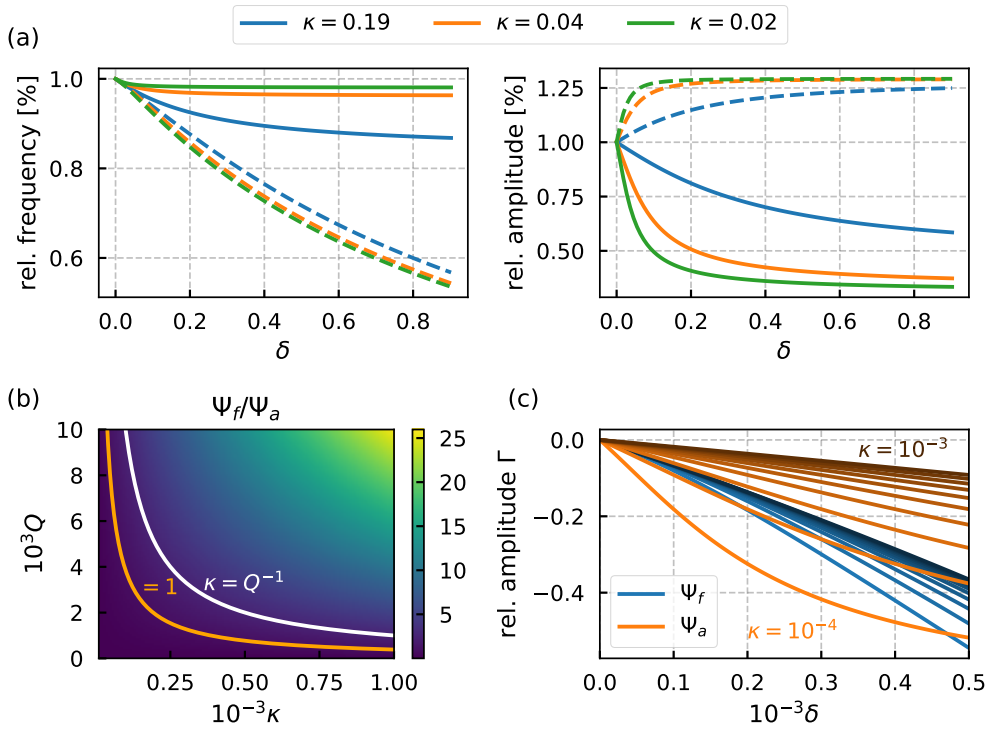

Figure 5.37: **(a)** Resonance frequencies and amplitudes for different relative couplings κ and relative mass changes δ. The values were generated by numerically solving the eigenstate problem Eq. (5.72). The values fit well to the FEM simulation shown in Fig 5.36. **(b)** Ratio between the amplitude change caused by a frequency shift (Ψ_f) and caused by the partial localization of the common modes (Ψ_A). The orange line indicates a ratio of $\Psi_f/\Psi_A = 1$. For values below one, the double cantilever system leads to an enhancement of the mass sensitivity. For values above one, there is no benefit of double cantilevers over a single one. The white line shows the minimal quality factor Q_{min} needed to resolve the two mechanical modes. **(c)** Relative amplitude change caused by a frequency shift (blue lines) and by the partial localization of the common modes (orange lines). The cantilever-cantilever coupling is coded into the brightness of the lines (bright: $\kappa = 10^{-4}$, dark: $\kappa = 10^{-3}$). All lines are calculated for a quality factor of $Q = 1000$. A higher slope of the relative amplitude implies a higher mass sensitivity. Only for $\kappa = 10^{-4}$ the slope for Ψ_a is higher than for Ψ_f. This fits well to the ratio shown in (b).

maximum usable relative coupling $\kappa_{min}(Q)$ can be determined by comparing the splitting $f_2 - f_1$ and width Δf of the common modes

$$f_2 - f_1 = \frac{1}{2\pi}\left(\sqrt{\frac{k+2k'}{m}} - \sqrt{\frac{k}{m}}\right) = \frac{1}{2\pi}\frac{\sqrt{k/m}}{Q} = \Delta f. \tag{5.86}$$

We get the minimum relative coupling

$$\kappa_{min}(Q) = \frac{1}{2Q^2} + \frac{1}{Q} \approx \frac{1}{Q}. \tag{5.87}$$

In Fig 5.37b, κ_{min} is indicated by the white line. It can be seen that the regime $\Psi_f/\Psi_A < 1$ can not be used as the two common modes cannot be resolved.

To verify this approximated comparison, the resonance frequencies and amplitudes of the system for varying mass changes were calculated numerically using Eq. (5.72). The calculated values are displayed in Fig 5.37a and fit well to the finite-element simulation shown in Fig 5.36a. To further compare Ψ_f and Ψ_a, the frequency change is expressed as an amplitude change using Eq. (5.83). For this transformation, a quality factor of $Q = 1000$ was used. The result for varying relative couplings is shown in Fig 5.37c. It can be seen that for $\kappa = 2 \times 10^{-4}$ the slopes of the relative amplitudes are approximately the same. For $\kappa = 1 \times 10^{-4}$, an improvement of Ψ_A over Ψ_f can be seen. This corresponds well to the previous estimate of the ratio Ψ_f/Ψ_A.

5.8 Conclusion and outlook

The demonstrated coupling of NV centers to the common modes of coupled mechanical resonators is a key step towards scalable phonon-based quantum transducers in diamond. But achieving high effective spin-spin couplings, necessary for phonon-mediated spin-spin entanglement, remains an elusive goal. However, as discussed in Section 5.5.3, the high cooperativity regime ($C > 1$) can be reached under realistic experimental conditions. The key challenge is to meet all requirements at the same. An important task is to create NV centers, with pristine spin properties, in highly-processed nanostructures. Additionally, new techniques, like e.g. orbital-strain coupling [35], offer new routes to enhance the performance of NV-mechanical hybrid devices.

Reaching the high cooperativity regime, enables the use of phonon-cooling techniques [134, 29, 135, 136], to bring the mechanical system close to its motional ground state. Furthermore, experimental realization of spin-phonon entanglement and mechanical squeezed states becomes feasible.

Bibliography

[1] Planck, M. Entropie und Temperatur strahlender Wärme. *Annalen der Physik* **306**, 719–737 (1900).

[2] Einstein, A. Über einen die Erzeugung und Verwandlung des Lichtes betreffenden heuristischen Gesichtspunkt. *Annalen der Physik* **322**, 132–148 (1905).

[3] MacFarlane A. G. J., Dowling Jonathan P. & Milburn Gerard J. Quantum technology: The second quantum revolution. *Philosophical Transactions of the Royal Society of London. Series A: Mathematical, Physical and Engineering Sciences* **361**, 1655–1674 (2003).

[4] Kimble, H. J. The quantum internet. *Nature* **453**, 1023–1030 (2008).

[5] Ladd, T. D. *et al.* Quantum computers. *Nature* **464**, 45–53 (2010).

[6] DiVincenzo, D. P. Quantum Computation. *Science* **270**, 255–261 (1995).

[7] Pirandola, S., Bardhan, B. R., Gehring, T., Weedbrook, C. & Lloyd, S. Advances in photonic quantum sensing. *Nature Photonics* **12**, 724 (2018).

[8] Degen, C. L., Reinhard, F. & Cappellaro, P. Quantum sensing. *Reviews of Modern Physics* **89**, 035002 (2017).

[9] Gisin, N., Ribordy, G., Tittel, W. & Zbinden, H. Quantum cryptography. *Reviews of Modern Physics* **74**, 145–195 (2002).

[10] Jeschke, G., Pannier, M. & Spiess, H. W. Double Electron-Electron Resonance. In Berliner, L. J., Eaton, G. R. & Eaton, S. S. (eds.) *Distance Measurements in Biological Systems by EPR*, Biological Magnetic Resonance, 493–512 (Springer US, Boston, MA, 2000).

[11] Timmel, C. R. & Harmer, J. R. (eds.) *Structural Information from Spin-Labels and Intrinsic Paramagnetic Centres in the Biosciences*. Structure and Bonding (Springer-Verlag, Berlin Heidelberg, 2013).

[12] Schlipf, L. *et al.* A molecular quantum spin network controlled by a single qubit. *Science Advances* **3**, e1701116 (2017).

[13] Grinolds, M. S. *et al.* Subnanometre resolution in three-dimensional magnetic resonance imaging of individual dark spins. *Nature Nanotechnology* **9**, 279–284 (2014).

[14] Balasubramanian, G. *et al.* Nanoscale imaging magnetometry with diamond spins under ambient conditions. *Nature* **455**, 648–651 (2008).

[15] Tisler, J. *et al.* Single Defect Center Scanning Near-Field Optical Microscopy on Graphene. *Nano Letters* **13**, 3152–3156 (2013).

[16] Tetienne, J.-P. *et al.* Nanoscale imaging and control of domain-wall hopping with a nitrogen-vacancy center microscope. *Science* **344**, 1366–1369 (2014).

[17] Häberle, T., Schmid-Lorch, D., Reinhard, F. & Wrachtrup, J. Nanoscale nuclear magnetic imaging with chemical contrast. *Nature Nanotechnology* **10**, 125–128 (2015).

[18] Rondin, L. *et al.* Stray-field imaging of magnetic vortices with a single diamond spin. *Nature Communications* **4**, 1–5 (2013).

[19] Maletinsky, P. *et al.* A robust scanning diamond sensor for nanoscale imaging with single nitrogen-vacancy centres. *Nature Nanotechnology* **7**, 320–324 (2012).

[20] Neumann, P. *et al.* Single-Shot Readout of a Single Nuclear Spin. *Science* **329**, 542–544 (2010).

[21] Häberle, T. *et al.* Nuclear quantum-assisted magnetometer. *Review of Scientific Instruments* **88**, 013702 (2017).

[22] Teufel, J. D. *et al.* Sideband cooling of micromechanical motion to the quantum ground state. *Nature* **475**, 359–363 (2011).

[23] O'Connell, A. D. *et al.* Quantum ground state and single-phonon control of a mechanical resonator. *Nature* **464**, 697–703 (2010).

[24] Chan, J. *et al.* Laser cooling of a nanomechanical oscillator into its quantum ground state. *Nature* **478**, 89–92 (2011).

[25] Rocheleau, T. *et al.* Preparation and detection of a mechanical resonator near the ground state of motion. *Nature* **463**, 72–75 (2010).

[26] LaHaye, M. D., Suh, J., Echternach, P. M., Schwab, K. C. & Roukes, M. L. Nanomechanical measurements of a superconducting qubit. *Nature* **459**, 960–964 (2009).

[27] Etaki, S. *et al.* Motion detection of a micromechanical resonator embedded in a d.c. SQUID. *Nature Physics* **4**, 785–788 (2008).

[28] Pirkkalainen, J.-M. *et al.* Hybrid circuit cavity quantum electrodynamics with a micromechanical resonator. *Nature* **494**, 211–215 (2013).

[29] Jöckel, A. *et al.* Sympathetic cooling of a membrane oscillator in a hybrid mechanical–atomic system. *Nature Nanotechnology* **10**, 55–59 (2015).

[30] Rugar, D., Budakian, R., Mamin, H. J. & Chui, B. W. Single spin detection by magnetic resonance force microscopy. *Nature* **430**, 329–332 (2004).

[31] Arcizet, O. *et al.* A single nitrogen-vacancy defect coupled to a nanomechanical oscillator. *Nature Physics* **7**, 879–883 (2011).

[32] Kolkowitz, S. *et al.* Coherent Sensing of a Mechanical Resonator with a Single-Spin Qubit. *Science* **335**, 1603–1606 (2012).

[33] Ovartchaiyapong, P., Lee, K. W., Myers, B. A. & Jayich, A. C. B. Dynamic strain-mediated coupling of a single diamond spin to a mechanical resonator. *Nature Communications* **5**, 4429 (2014).

[34] Ali Momenzadeh, S. *et al.* Thin Circular Diamond Membrane with Embedded Nitrogen-Vacancy Centers for Hybrid Spin-Mechanical Quantum Systems. *Physical Review Applied* **6**, 024026 (2016).

[35] Lee, K. W. *et al.* Strain Coupling of a Mechanical Resonator to a Single Quantum Emitter in Diamond. *Physical Review Applied* **6**, 034005 (2016).

[36] Meesala, S. *et al.* Enhanced Strain Coupling of Nitrogen-Vacancy Spins to Nanoscale Diamond Cantilevers. *Physical Review Applied* **5**, 034010 (2016).

[37] Teissier, J., Barfuss, A., Appel, P., Neu, E. & Maletinsky, P. Strain Coupling of a Nitrogen-Vacancy Center Spin to a Diamond Mechanical Oscillator. *Physical Review Letters* **113**, 020503 (2014).

[38] Barfuss, A., Teissier, J., Neu, E., Nunnenkamp, A. & Maletinsky, P. Strong mechanical driving of a single electron spin. *Nature Physics* **11**, 820–824 (2015).

[39] MacQuarrie, E. R., Gosavi, T. A., Bhave, S. A. & Fuchs, G. D. Continuous dynamical decoupling of a single diamond nitrogen-vacancy center spin with a mechanical resonator. *Physical Review B* **92**, 224419 (2015).

[40] MacQuarrie, E. R., Gosavi, T. A., Jungwirth, N. R., Bhave, S. A. & Fuchs, G. D. Mechanical Spin Control of Nitrogen-Vacancy Centers in Diamond. *Physical Review Letters* **111**, 227602 (2013).

[41] Golter, D. A. *et al.* Coupling a Surface Acoustic Wave to an Electron Spin in Diamond via a Dark State. *Physical Review X* **6**, 041060 (2016).

[42] Rabl, P. *et al.* A quantum spin transducer based on nanoelectromechanical resonator arrays. *Nature Physics* **6**, 602–608 (2010).

[43] Zaitsev, A. M. Vibronic spectra of impurity-related optical centers in diamond. *Physical Review B* **61**, 12909–12922 (2000).

[44] Zaitsev, A. M. *Optical Properties of Diamond: A Data Handbook* (Springer-Verlag, Berlin Heidelberg, 2001).

[45] Klein, C. A. & Cardinale, G. F. Young's modulus and Poisson's ratio of CVD diamond. *Diamond and Related Materials* **2**, 918–923 (1993).

[46] Lide, D. R. *CRC Handbook of Chemistry and Physics, 85th Edition* (CRC Press, 2004).

[47] Ovartchaiyapong, P., Pascal, L. M. A., Myers, B. A., Lauria, P. & Bleszynski Jayich, A. C. High quality factor single-crystal diamond mechanical resonators. *Applied Physics Letters* **101**, 163505 (2012).

[48] Tao, Y., Boss, J. M., Moores, B. A. & Degen, C. L. Single-crystal diamond nanomechanical resonators with quality factors exceeding one million. *Nature Communications* **5**, 3638 (2014).

[49] Rath, P., Ummethala, S., Nebel, C. & Pernice, W. H. P. Diamond as a material for monolithically integrated optical and optomechanical devices. *physica status solidi (a)* **212**, 2385–2399 (2015).

[50] Victor, A. C. Heat Capacity of Diamond at High Temperatures. *The Journal of Chemical Physics* **36**, 1903–1911 (1962).

[51] Najar, H. *et al.* High quality factor nanocrystalline diamond micromechanical resonators limited by thermoelastic damping. *Applied Physics Letters* **104**, 151903 (2014).

[52] Walker, J. Optical absorption and luminescence in diamond. *Reports on Progress in Physics* **42**, 1605–1659 (1979).

[53] Aharonovich, I., Greentree, A. D. & Prawer, S. Diamond photonics. *Nature Photonics* **5**, 397–405 (2011).

[54] Chrostoski, P., Sadeghpour, H. R. & Santamore, D. H. Electric Noise Spectra of a Near-Surface Nitrogen-Vacancy Center in Diamond with a Protective Layer. *Physical Review Applied* **10**, 064056 (2018).

[55] Rosskopf, T. Investigation of Surface Magnetic Noise by Shallow Spins in Diamond. *Physical Review Letters* **112** (2014).

[56] Myers, B. A. *et al.* Probing Surface Noise with Depth-Calibrated Spins in Diamond. *Physical Review Letters* **113**, 027602 (2014).

[57] Ofori-Okai, B. K. *et al.* Spin properties of very shallow nitrogen vacancy defects in diamond. *Physical Review B* **86**, 081406 (2012).

[58] Romach, Y. *et al.* Spectroscopy of Surface-Induced Noise Using Shallow Spins in Diamond. *Physical Review Letters* **114**, 017601 (2015).

[59] Ohno, K. *et al.* Engineering shallow spins in diamond with nitrogen delta-doping. *Applied Physics Letters* **101**, 082413 (2012).

[60] de Oliveira, F. F. *et al.* Tailoring spin defects in diamond by lattice charging. *Nature Communications* **8**, 1–8 (2017).

[61] Cui, S. *et al.* Reduced Plasma-Induced Damage to Near-Surface Nitrogen-Vacancy Centers in Diamond. *Nano Letters* **15**, 2887–2891 (2015).

[62] Gruber, A. *et al.* Scanning Confocal Optical Microscopy and Magnetic Resonance on Single Defect Centers. *Science* **276**, 2012–2014 (1997).

[63] Oeckinghaus, T. *et al.* A compact, diode laser based excitation system for microscopy of NV centers. *Review of Scientific Instruments* **85**, 073101 (2014).

[64] Rogers, L. J., Armstrong, S., Sellars, M. J. & Manson, N. B. Infrared emission of the NV centre in diamond: Zeeman and uniaxial stress studies. *New Journal of Physics* **10**, 103024 (2008).

[65] Doherty, M. W. *et al.* The nitrogen-vacancy colour centre in diamond. *Physics Reports* **528**, 1–45 (2013).

[66] Rogers, L. J. *et al.* Singlet levels of the NV-centre in diamond. *New Journal of Physics* **17**, 013048 (2015).

[67] Lenef, A. & Rand, S. C. Electronic structure of the N-V center in diamond: Theory. *Physical Review B* **53**, 13441–13455 (1996).

[68] Fuchs, G. D. *et al.* Excited-State Spectroscopy Using Single Spin Manipulation in Diamond. *Physical Review Letters* **101**, 117601 (2008).

[69] Felton, S. *et al.* Hyperfine interaction in the ground state of the negatively charged nitrogen vacancy center in diamond. *Physical Review B* **79**, 075203 (2009).

[70] Smeltzer, B., McIntyre, J. & Childress, L. Robust control of individual nuclear spins in diamond. *Physical Review A* **80**, 050302 (2009).

[71] Steiner, M., Neumann, P., Beck, J., Jelezko, F. & Wrachtrup, J. Universal enhancement of the optical readout fidelity of single electron spins at nitrogen-vacancy centers in diamond. *Physical Review B* **81**, 035205 (2010).

[72] Brown, R. W., Cheng, Y.-C. N., Haacke, E. M., Thompson, M. R. & Venkatesan, R. *Magnetic Resonance Imaging: Physical Principles and Sequence Design* (Wiley-Blackwell, Hoboken, New Jersey, 2014), 2. edn.

[73] Slichter, C. P. *Principles of Magnetic Resonance*. Springer Series in Solid-State Sciences (Springer-Verlag, Berlin Heidelberg, 1990), third edn.

[74] Levitt, M. H. *Spin Dynamics: Basics of Nuclear Magnetic Resonance* (Wiley, Chichester, England ; Hoboken, NJ, 2008), 2. edn.

[75] Ramsey, N. F. A Molecular Beam Resonance Method with Separated Oscillating Fields. *Physical Review* **78**, 695–699 (1950).

[76] Hahn, E. L. Spin Echoes. *Physical Review* **80**, 580–594 (1950).

[77] Meiboom, S. & Gill, D. Modified Spin-Echo Method for Measuring Nuclear Relaxation Times. *Review of Scientific Instruments* **29**, 688–691 (1958).

[78] Uhrig, G. S. Keeping a Quantum Bit Alive by Optimized $\ensuremath{\pi}$-Pulse Sequences. *Physical Review Letters* **98**, 100504 (2007).

[79] Souza, A. M., Álvarez, G. A. & Suter, D. Robust dynamical decoupling. *Philosophical Transactions of the Royal Society A: Mathematical, Physical and Engineering Sciences* **370**, 4748–4769 (2012).

[80] Maudsley, A. A. Modified Carr-Purcell-Meiboom-Gill sequence for NMR fourier imaging applications. *Journal of Magnetic Resonance (1969)* **69**, 488–491 (1986).

[81] Gullion, T. & Schaefer, J. Elimination of resonance offset effects in rotational-echo, double-resonance NMR. *Journal of Magnetic Resonance (1969)* **92**, 439–442 (1991).

[82] Kendrew, J. C. *et al.* A Three-Dimensional Model of the Myoglobin Molecule Obtained by X-Ray Analysis. *Nature* **181**, 662–666 (1958).

[83] Ilari, A. & Savino, C. Protein Structure Determination by X-Ray Crystallography. In Keith, J. M. (ed.) *Bioinformatics: Data, Sequence Analysis and Evolution*, Methods in Molecular Biology™, 63–87 (Humana Press, Totowa, NJ, 2008).

[84] Cross, T. & Opella, S. Protein Structure from Solid-State NMR. *Journal of the American Chemical Society* **105** (2003).

[85] Pezzagna, S., Naydenov, B., Jelezko, F., Wrachtrup, J. & Meijer, J. Creation efficiency of nitrogen-vacancy centres in diamond. *New Journal of Physics* **12**, 065017 (2010).

[86] Momenzadeh, S. A. *et al.* Nanoengineered Diamond Waveguide as a Robust Bright Platform for Nanomagnetometry Using Shallow Nitrogen Vacancy Centers. *Nano Letters* **15**, 165–169 (2015).

[87] de Lange, G. *et al.* Controlling the quantum dynamics of a mesoscopic spin bath in diamond. *Scientific Reports* **2**, 1–5 (2012).

[88] Mamin, H. J., Sherwood, M. H. & Rugar, D. Detecting external electron spins using nitrogen-vacancy centers. *Physical Review B* **86**, 195422 (2012).

[89] Shi, F. *et al.* Single-protein spin resonance spectroscopy under ambient conditions. *Science* **347**, 1135–1138 (2015).

[90] Neumann, P. *et al.* Quantum register based on coupled electron spins in a room-temperature solid. *Nature Physics* **6**, 249–253 (2010).

[91] Osipov, V. Y., Shames, A. I. & Vul', A. Y. Exchange coupled pairs of dangling bond spins as a new type of paramagnetic defects in nanodiamonds. *Physica B: Condensed Matter* **404**, 4522–4524 (2009).

[92] Diaspro, A., Chirico, G., Usai, C., Ramoino, P. & Dobrucki, J. Photobleaching. In *Handbook of Biological Confocal Microscopy: Third Edition*, 690–702 (2010).

[93] Huelga, S. F. *et al.* Improvement of Frequency Standards with Quantum Entanglement. *Physical Review Letters* **79**, 3865–3868 (1997).

[94] Hopper, D. A., Shulevitz, H. J. & Bassett, L. C. Spin Readout Techniques of the Nitrogen-Vacancy Center in Diamond. *Micromachines* **9**, 437 (2018).

[95] Robledo, L. *et al.* High-fidelity projective read-out of a solid-state spin quantum register. *Nature* **477**, 574–578 (2011).

[96] Chen, X.-D., Zou, C.-L., Sun, F.-W. & Guo, G.-C. Optical manipulation of the charge state of nitrogen-vacancy center in diamond. *Applied Physics Letters* **103**, 013112 (2013).

[97] Waldherr, G., Neumann, P., Huelga, S. F., Jelezko, F. & Wrachtrup, J. Violation of a Temporal Bell Inequality for Single Spins in a Diamond Defect Center. *Physical Review Letters* **107**, 090401 (2011).

[98] Waldherr, G. *et al.* Dark States of Single Nitrogen-Vacancy Centers in Diamond Unraveled by Single Shot NMR. *Physical Review Letters* **106**, 157601 (2011).

[99] Aslam, N., Waldherr, G., Neumann, P., Jelezko, F. & Wrachtrup, J. Photo-induced ionization dynamics of the nitrogen vacancy defect in diamond investigated by single-shot charge state detection. *New Journal of Physics* **15**, 013064 (2013).

[100] Jiang, L. *et al.* Repetitive Readout of a Single Electronic Spin via Quantum Logic with Nuclear Spin Ancillae. *Science* **326**, 267–272 (2009).

[101] Staudacher, T. *et al.* Nuclear Magnetic Resonance Spectroscopy on a (5-Nanometer)3 Sample Volume. *Science* **339**, 561–563 (2013).

[102] Staudacher, T. *et al.* Probing molecular dynamics at the nanoscale via an individual paramagnetic centre. *Nature Communications* **6**, 1–7 (2015).

[103] Kong, X., Stark, A., Du, J., McGuinness, L. P. & Jelezko, F. Towards Chemical Structure Resolution with Nanoscale Nuclear Magnetic Resonance Spectroscopy. *Physical Review Applied* **4**, 024004 (2015).

[104] Zaiser, S. *et al.* Enhancing quantum sensing sensitivity by a quantum memory. *Nature Communications* **7**, 1–11 (2016).

[105] Pfender, M. *et al.* Nonvolatile nuclear spin memory enables sensor-unlimited nanoscale spectroscopy of small spin clusters. *Nature Communications* **8**, 1–12 (2017).

[106] Aslam, N. *et al.* Nanoscale nuclear magnetic resonance with chemical resolution. *Science* **357**, 67–71 (2017).

[107] Stajic, J. The Future of Quantum Information Processing. *Science* **339**, 1163–1163 (2013).

[108] Kurizki, G. *et al.* Quantum technologies with hybrid systems. *Proceedings of the National Academy of Sciences* **112**, 3866–3873 (2015).

[109] Oeckinghaus, T. *et al.* Spin–Phonon Interfaces in Coupled Nanomechanical Cantilevers. *Nano Letters* **20**, 463–469 (2020).

[110] Hauer, B. D., Doolin, C., Beach, K. S. D. & Davis, J. P. A general procedure for thermomechanical calibration of nano/micro-mechanical resonators. *Annals of Physics* **339**, 181–207 (2013).

[111] Schmid, S., Villanueva, L. G. & Roukes, M. L. *Fundamentals of Nanomechanical Resonators* (Springer International Publishing, 2016).

[112] Karraï, K. & Grober, R. D. Piezo-electric tuning fork tip—sample distance control for near field optical microscopes. *Ultramicroscopy* **61**, 197–205 (1995).

[113] Shankar, R. *Principles of Quantum Mechanics* (Springer, New York, 1994), 2. edn.

[114] Barnes, J. R. *et al.* A femtojoule calorimeter using micromechanical sensors. *Review of Scientific Instruments* **65**, 3793–3798 (1994).

[115] Labuda, A., Kobayashi, K., Miyahara, Y. & Grütter, P. Retrofitting an atomic force microscope with photothermal excitation for a clean cantilever response in low Q environments. *Review of Scientific Instruments* **83**, 053703 (2012).

[116] Evans, D. R. *et al.* Laser Actuation of Cantilevers for Picometre Amplitude Dynamic Force Microscopy. *Scientific Reports* **4**, 5567 (2014).

[117] Jayakumar, H., Khanaliloo, B., Lake, D. P. & Barclay, P. E. Cooling and amplifying motion of a diamond resonator with a microscope. *arXiv:1810.04196 [cond-mat, physics:physics]* (2018). 1810.04196.

[118] Boales, J. A., Mateen, F. & Mohanty, P. Micromechanical Resonator Driven by Radiation Pressure Force. *Scientific Reports* **7**, 16056 (2017).

[119] Ma, D. & Munday, J. N. Measurement of wavelength-dependent radiation pressure from photon reflection and absorption due to thin film interference. *Scientific Reports* **8**, 1–6 (2018).

[120] Element Six Technologies. *The Element Six CVD Diamond Handbook* (2019).

[121] Doherty, M. W. *et al.* Theory of the ground-state spin of the NV$\{\}\hat{\}\ensuremath\{-\}\}$ center in diamond. *Physical Review B* **85**, 205203 (2012).

[122] Bennett, S. D. *et al.* Measuring mechanical motion with a single spin. *New Journal of Physics* **14**, 125004 (2012).

[123] Balasubramanian, G. *et al.* Ultralong spin coherence time in isotopically engineered diamond. *Nature Materials* **8**, 383–387 (2009).

[124] Bar-Gill, N., Pham, L. M., Jarmola, A., Budker, D. & Walsworth, R. L. Solid-state electronic spin coherence time approaching one second. *Nature Communications* **4**, 1–6 (2013).

[125] Ohashi, K. *et al.* Negatively Charged Nitrogen-Vacancy Centers in a 5 nm Thin 12C Diamond Film. *Nano Letters* **13**, 4733–4738 (2013).

[126] Jakobi, I. *et al.* Measuring broadband magnetic fields on the nanoscale using a hybrid quantum register. *Nature Nanotechnology* **12**, 67–72 (2017).

[127] Kuzyk, M. C. & Wang, H. Scaling Phononic Quantum Networks of Solid-State Spins with Closed Mechanical Subsystems. *Physical Review X* **8**, 041027 (2018).

[128] Malvar, O. *et al.* Mass and stiffness spectrometry of nanoparticles and whole intact bacteria by multimode nanomechanical resonators. *Nature Communications* **7**, 1–8 (2016).

[129] Hanay, M. S. *et al.* Single-protein nanomechanical mass spectrometry in real time. *Nature Nanotechnology* **7**, 602–608 (2012).

[130] Chaste, J. *et al.* A nanomechanical mass sensor with yoctogram resolution. *Nature Nanotechnology* **7**, 301–304 (2012).

[131] Barson, M. S. J. *et al.* Nanomechanical Sensing Using Spins in Diamond. *Nano Letters* **17**, 1496–1503 (2017).

[132] Spletzer, M., Raman, A., Wu, A. Q., Xu, X. & Reifenberger, R. Ultrasensitive mass sensing using mode localization in coupled microcantilevers. *Applied Physics Letters* **88**, 254102 (2006).

[133] Toyli, D. M. *et al.* Measurement and Control of Single Nitrogen-Vacancy Center Spins above 600 K. *Physical Review X* **2**, 031001 (2012).

[134] Rao, D. D. B., Momenzadeh, S. A. & Wrachtrup, J. Heralded Control of Mechanical Motion by Single Spins. *Physical Review Letters* **117**, 077203 (2016).

[135] Rabl, P. Cooling of mechanical motion with a two-level system: The high-temperature regime. *Physical Review B* **82**, 165320 (2010).

[136] Kepesidis, K. V., Bennett, S. D., Portolan, S., Lukin, M. D. & Rabl, P. Phonon cooling and lasing with nitrogen-vacancy centers in diamond. *Physical Review B* **88**, 064105 (2013).

Acknowledgments

Throughout my time, working on my PhD thesis, a lot of great people helped, supported and influenced me. I am thankful to every one of them.

I would like to thank Prof. Jörg Wrachtrup for giving me the opportunity to work on interesting projects and his support throughout my thesis. I would like to thank Prof. Sebastian Loth for acting as the second referee and Prof. Maria Daghofer for chairing my defense.

Throughout my work I had the pleasure to work with three great supervisors. Each one of them helped and influenced me in his own way and I am incredibly thankful to all of them.

Dr. Friedemann Reinhard, not only guided me on my first steps as a PhD student, but also supervised my diploma thesis. He contributed greatly to my decision to start my PhD journey in the first place. He helped me to re-build the Asylum AFM setup and getting my experiments started.

Dr. Amit Finkler greatly helped me to improve my scientific and experimental skills. He was a great support and source of advice in and outside of the lab. I am thankful for his influence on my post-PhD career.

Dr. Rainer Stöhr supported me during the last part of my work as a PhD student. I was always impressed by his willingness and dedication to help out others. Although he had a lot of responsibilities, a very high workload and a family waiting for him, he never hesitated to spend his time helping me, or others, out.

Furthermore, I want to thank Dr. Thomas Häberle and Dr. Dominik Schmid-Lorch, with whom I shared a lab for several years. I greatly benefited from their scientific and technical advice. As we operated similar setups, we had a great synergy working together. I will miss the times we did spend in the lab together.

A special thank you goes to Dr. Durga Dasari for his support in theoretical problems and the fruitful collaboration towards publications. Additionally,

I am greatly thankful to Dr. Ali Seyed Momenzadeh for sample fabrications and especially for pushing me forward in the mechanical resonator project he initiated.

I want to thank Dr. Lukas Schlipf for fruitful discussions and his work on the nanoscale ESR project. His effort and dedication provided a satisfying conclusion to the project and thereby added great value.

I want to thank Dr. Julia Tisler for her help during my diploma thesis and for introducing me to the Asylum AFM setup.

Furthermore, I want to thank all other members of the AFM group: Dr. Andreas Brunner, Dr. Bastian Kern, Dr. Qi-Chao Sun, Tetyana Shalomayeva, Philipp Scheiger, Domenico Paone, Dinesh Pinto, Minsik Kwon and Anurag Kanase.

I am thankful to Johannes Greiner for our good time sharing an office and fruitful discussions about physics, football and life. I want to thank Dr. Matthias Pfender, Dr. Sebastian Zaiser, Dr. Nabeel Aslam, Nikolas Abt, Dr. Roland Nagy and Dr. Natan Chejanovsky for discussions in and around the lab.

I want to thank Dr. Andrej Denisenko, Dr. Felipe Favaro de Oliveira, Dr. Rolf Reuter, Dr. Andrea Zappe and Stephan Hirschmann for technical support. Furthermore, I am thankful to Claudia Unger, Ivanka Spajic and all members of the 3rd physics institute.

Last but not least, I want to thank my family. My parents, Christa and Rolf Oeckinghaus, were a great support during all phases of my life and hold a great share in my successful PhD thesis. Especially in the role of loving grandparents, they were always there to help out and take care of my son Leo, whenever I couldn't. I admire them for their dedication to enrich the lives of all their grandchildren.

I am most thankful to my loving wife Mona, whose endless patience and support enabled this thesis in the first place. I am also thankful to my son Leo, who has been an unbelievably huge source of motivation and joy.